

The Response of Hot QCD Matter to Hard Partons

by

Richard Bryon Neufeld

Department of Physics
Duke University

Date: _____

Approved:

Berndt Müller, Advisor

Steffen Bass

Henry Greenside

Thomas Mehen

Henry Weller

Dissertation submitted in partial fulfillment of the requirements for the degree of
Doctor of Philosophy in the Department of Physics
in the Graduate School of Duke University
2009

UMI Number: 3366808

INFORMATION TO USERS

The quality of this reproduction is dependent upon the quality of the copy submitted. Broken or indistinct print, colored or poor quality illustrations and photographs, print bleed-through, substandard margins, and improper alignment can adversely affect reproduction.

In the unlikely event that the author did not send a complete manuscript and there are missing pages, these will be noted. Also, if unauthorized copyright material had to be removed, a note will indicate the deletion.



UMI Microform 3366808
Copyright 2009 by ProQuest LLC
All rights reserved. This microform edition is protected against
unauthorized copying under Title 17, United States Code.

ProQuest LLC
789 East Eisenhower Parkway
P.O. Box 1346
Ann Arbor, MI 48106-1346

ABSTRACT
(Physics)

The Response of Hot QCD Matter to Hard Partons

by

Richard Bryon Neufeld

Department of Physics
Duke University

Date: _____

Approved:

Berndt Müller, Advisor

Steffen Bass

Henry Greenside

Thomas Mehen

Henry Weller

An abstract of a dissertation submitted in partial fulfillment of the requirements for
the degree of Doctor of Philosophy in the Department of Physics
in the Graduate School of Duke University
2009

Copyright © 2009 by Richard Bryon Neufeld
All rights reserved except the rights granted by the
Creative Commons Attribution-Noncommercial Licence

Abstract

The *quark gluon plasma* (QGP) forms when matter governed by *quantum chromodynamics* (QCD) undergoes a transition at high temperature or high density from hadronic bound states to deconfined quarks and gluons. The QGP at high temperature is believed to be experimentally accessible in relativistic heavy-ion collisions, such as those done at the Relativistic Heavy-Ion Collider (RHIC) at Brookhaven National Lab and in the near future at the Large Hadron Collider (LHC) at CERN. The results obtained so far reveal the production of energetic (hard) partons in the early stages of a heavy-ion collision which propagate through the plasma. Results also show that the QGP produced at RHIC is a nearly ideal fluid and that hard partons may generate conical, Mach-like, disturbances in the QGP.

This thesis uses theoretical methods to address how the QGP responds to a hard parton that propagates through the plasma and contains the first rigorous derivation of how a hard parton deposits energy and momentum in a QGP which lead to the formation of a Mach cone. A comparison of experimental results with the theory introduced in this thesis could shed light on important properties of the QGP such as its equation of state and transport coefficients like viscosity. I investigate this problem by evaluating the source of energy and momentum generated by the hard parton in the QGP. Formalisms are developed and applied for evaluating the source of energy and momentum in perturbation theory with three different methods: classical kinetic theory, finite temperature field theory, and by including the energy lost

by the hard parton to radiation. Having obtained the source of energy and momentum generated by the hard parton, I evaluate the medium response using linearized hydrodynamics. My results show Mach cone formation in the medium. I compare the medium response for different viscosities and speeds of sound, from which I find the Mach cone weakens and broadens as viscosity is increased. By studying the time evolution of the medium response once the source of energy and momentum is turned off, which occurs in a heavy-ion collision during the hadronic phase, I find that the conical disturbance is enhanced relative to diffusive contributions over a time period of several fm/c.

Contents

Abstract	iv
List of Figures	viii
Abbreviations, Symbols and Conventions	x
Acknowledgements	xi
1 Introduction	1
1.1 QCD and the Transition to Quark-Gluon Plasma	1
1.2 Experimentally Probing the Quark-Gluon Plasma	12
2 Investigating the Medium Response: Overview	26
2.1 Two Mechanisms for Conical Emission	26
2.2 Investigating Induced Flow in the QGP	29
3 Hydrodynamic Source Term from Kinetic Theory	32
3.1 Hydrodynamic Source Term	36
3.1.1 A Comment on the Dielectric Screening	40
3.2 Explicit Evaluation of the Source Term	41
3.3 The Unscreened Source Term	45
3.4 Result With Screening	51
3.5 Discussion	52
4 Hydrodynamic Source Term with Radiation	55
4.1 Calculating the Energy Absorption	56

4.2	Discussion	61
5	Finite Temperature Field Theory Evaluation	62
5.1	Scalar Theory with Source	62
5.1.1	General Form of the Energy Momentum Tensor	62
5.1.2	Calculating Correlation Functions in Real Time	64
5.1.3	Calculating the Source of Energy and Momentum	66
5.2	Vlasov Equation for a Scalar Field Theory	72
5.3	Discussion	74
6	Medium Response in Linearized Hydrodynamics	76
6.1	Kinetic Source Term	77
6.1.1	Linearized Hydrodynamics With a Source Term	77
6.1.2	Delta Function and Momentum Space Representation	81
6.1.3	Solving the Equations	84
6.2	Source Term with Radiation	90
6.3	Numerical Results	93
6.3.1	Kinetic Theory Source Term	93
6.3.2	Radiative and Collisional Source Term	98
6.4	Discussion and Conclusions	102
7	Comparison of AdS/CFT and pQCD Results	103
8	Summary	108
9	Appendix	113
	Bibliography	137
	Biography	142

List of Figures

1.1	$\epsilon(T)/T^4 \sim \nu(T)$ as a function of temperature [5]	5
1.2	The renormalized result for $\langle L \rangle$ as a function of temperature [7]	6
1.3	$\Delta_{l,s}$ as a function of temperature [7]	8
1.4	Phase diagram of QCD [10].	9
1.5	α_s in medium [11]	10
1.6	Debye screening mass [11]	10
1.7	Speed of sound [11]	11
1.8	Elliptic flow [18]	14
1.9	Viscous hydrodynamics elliptic flow [20]	15
1.10	High p_T hadron suppression [22]	16
1.11	A geometrical representation of azimuthal correlations.	17
1.12	Azimuthal associated hadron suppression [23]	18
1.13	Azimuthal di-hadron correlations [24].	20
1.14	Azimuthal di-hadron correlations, most central [24].	21
1.15	Azimuthal di-hadron correlations, least central [24].	22
1.16	Three hadron correlations [27]	24
2.1	Doppler effect [31]	28
3.1	Hydro distance scales	35
3.2	Scaled energy density deposition	47
3.3	Velocity dependence of $-dE/dx$, as given by (3.59)	49

3.4	$J^0(\rho, z, t)/(\gamma u^2)$ as a function of $\gamma(z - ut)$	50
3.5	Screened and unscreened energy density deposition	52
3.6	Screened and unscreened transverse momentum density deposition	53
3.7	Detailed transverse momentum density comparison	53
4.1	Differential energy absorption	59
5.1	Diagrams of the ϕ^4 theory with a source.	68
6.1	3D plot comparing finite source structure	94
6.2	Linear plot comparing finite source structure	94
6.3	Conical contour plots comparing viscosity	95
6.4	Scaled 3D plots comparing viscosity	96
6.5	Conical contour plots comparing sound	97
6.6	Scaled 3D plots comparing sound	97
6.7	Energy density wave evolving in time	100
6.8	Momentum density wave evolving in time	101
7.1	Comparing AdS/CFT and pQCD medium response	106
E-1	Bending the contour for numerical integration.	125

Abbreviations, Symbols and Conventions

Symbols and Conventions

Natural units are used $\hbar = k_B = c = 1$. Indices given by Latin letters generally range from 1 - 3, whereas indices given by Greek letter range from 0 - 3. Repeated indices are summed over.

Abbreviations

- QCD Quantum Chromodynamics (see chapter 1).
- QGP Quark Gluon Plasma (see chapter 1).
- RHIC Relativistic Heavy Ion Collider, an experimental program at Brookhaven National Laboratory designed to, among other things, form and study the quark gluon plasma.

Acknowledgements

This is the last section to be written in any thesis, and probably the hardest. How do you put into a page or two what people have meant to you during your doctoral program? Certainly my acknowledgments will be inadequate, nevertheless, I will do my best.

I must start by thanking my advisor, Berndt Müller. It was his presentation to my first year graduate class that got me interested in this field of physics, and it was his continuing mentorship that has gotten me to this point. He has an amazing breadth of physics knowledge and an equally amazing ability to teach. He knew just how hard to push me along the way and never let me get too comfortable with how much I thought I knew. I could not have asked for more from an advisor.

I must also thank my PhD advisory committee which has taught me the importance of expanding my horizons and trying to understand the big picture. In particular, I thank Steffen Bass who has regularly provided mentorship and new insights into my work.

I am also grateful to my fellow graduate students who have provided friendship, support, and have challenged me to push myself during my time at Duke. In particular, I thank Wei Chen and Huidong Xu for their friendship and countless hours of help and discussion throughout our first and second year course work, as well as Matt Kiser and Matt Blackston who served as mentors. I am especially indebted to my good friend and office mate, Nasser Demir. Nasser is a wonderful friend who

served as a groomsman in my wedding and roommate on several conference trips. Nasser has been an invaluable resource for discussion and insight during the last five years.

There are many outside of the department whose support has been instrumental to my education at Duke. I thank my church community at the Church of the Good Shepherd and especially the Grad and Career Flock. The encouragement I have received from Troy, David, Justin, Richard and so many others has been invaluable. I also want to thank the North Durham Shepherding Group. I will always be grateful to Scott and Sarah, Garheng and Melissa, Chris, Ian, Roman, Mark and so many others for the support I have received during our weekly meetings.

Without the love, support and guidance of my two wonderful parents I dare not imagine where I would be today. Thank you Mom for making me believe I can achieve anything and consistently pointing out how “special” I am. Thank you Dad for many years on the golf course together and, more importantly, for being the single most important mentor to me in my relationship with Jesus Christ. I also am grateful to my older sister, Aimee. Thank you for always being there for me and helping to make me who I am today.

I thank my beautiful wife and best friend Betsy. You are my inspiration, you are my dream come true. What you have meant to me during the last two years is hard to put into words. Thanks for your support and love. You were the first to hear when I was discouraged or frustrated and you always pushed me to persevere. I look forward to spending the rest of our lives together.

Finally, I thank my Lord and Savior Jesus Christ, for apart from Him, I can do nothing (John 15:5). My relationship with Jesus shapes the way I see the world and who I am as a person and a scholar.

Introduction

The work in this thesis is primarily concerned with investigating certain aspects of a state of matter known as the *quark gluon plasma*, or QGP. The QGP is formed when strongly interacting matter, that is matter governed by *quantum chromodynamics* (QCD), undergoes a transition from hadronic bound states to deconfined quarks and gluons. This chapter will contain a broad introduction to the QGP. I begin with an introduction to QCD, which is the underlying theory of the QGP, and discuss the order parameters associated with the transition. After this, some fundamental properties of the QGP which have been determined from various theoretical techniques are listed. Finally, I introduce important experimental results which provide context and motivation for what follows in the rest of the thesis.

1.1 QCD and the Transition to Quark-Gluon Plasma

QCD provides a theoretical description of strongly interacting, or color charged, matter, that is, quarks and gluons (a more thorough introduction to QCD than that contained here can be found in [1]). From a historical and phenomenological point of view, the great success of QCD is that, as a non-Abelian gauge theory, it exhibits

asymptotic freedom, which is the observation that the coupling between quarks and gluons grows weaker as the distance scale becomes shorter. The reverse is also true: the coupling becomes stronger at larger distance scales such that only color neutral quark bound states (called *hadrons*) can be directly observed. The dynamics of the theory is governed by the QCD Lagrangian, which is given by

$$\mathcal{L} = \sum_f \bar{\psi}_f (i\gamma^\mu D_\mu - m_f) \psi_f - \frac{1}{4} G_{\mu\nu}^a G_a^{\mu\nu} \quad (1.1)$$

where G is called the gluonic field strength tensor and is

$$G_{\mu\nu}^a = \partial_\mu A_\nu^a - \partial_\nu A_\mu^a + gf^{abc} A_\mu^b A_\nu^c \quad (1.2)$$

where A_ν^a is the gluon field and f^{abc} are the $SU(3)$ structure numbers. The gauge covariant derivative has the form

$$D_\mu = \partial_\mu \mathbb{1} - igA_\mu^a t^a \quad (1.3)$$

where t^a are the fundamental representation matrices of $SU(3)$ and $\mathbb{1}$ is the identity matrix. The index a can range from 1 to 8, as there are 8 gluon fields in QCD. The quark fields are contained in the spinors, ψ_f , where the subscript f indicates quark flavor.

Having the Lagrangian, one can write down formal expressions for quantities of interest, such as correlation functions, scattering amplitudes, etc, by using the path integral formalism. In practice, the complex non-linear structure of (1.1) makes finding exact solutions for these quantities essentially impossible. However, powerful techniques, in particular perturbation theory and lattice simulations, have been developed which allow calculations to be performed under certain approximations. One especially important result is that the strong coupling 'constant', $\alpha_s = g^2/4\pi$, depends on the momentum transfer, k , of a given process such that, to leading order

$$\alpha_s(k) = \frac{\alpha_s(\Lambda)}{1 + \alpha_s(\Lambda) \frac{33-2N_f}{12\pi} \ln\left(\frac{k^2}{\Lambda^2}\right)} \quad (1.4)$$

where $N_f = 6$ and Λ is the scale at which α_s is determined experimentally. Equation (1.4) predicts that the strong coupling becomes smaller at larger momentum scales, or smaller distances, and is the mathematical statement of asymptotic freedom.

The transition from hadronic bound states to deconfined quarks and gluons is associated with an increase in temperature and or baryon chemical potential, in other words, an increase in the density of color charged particles. One can gain a straightforward physical intuition for why the transition should take place by considering what happens to a system of hadrons as the density is increased. Eventually, the quarks within the hadrons begin to overlap so that it's no longer possible to identify individual hadrons within the system. Furthermore, the high density of color charges creates a screening effect such that the long distance, confining growth of the coupling constant is no longer important (a more detailed version of this line of thinking can be found in [2]). The end result is that the relevant degrees of freedom are no longer hadrons, but deconfined quarks and gluons.

Such a transition would manifest itself in a change in the number of degrees of freedom, $\nu(T)$, of QCD matter as temperature increases, where T denotes temperature (in the rest of this section I will focus on the temperature dependence of the transition, neglecting finite baryon chemical potential). For a thermodynamic medium, $\nu(T)$ can be defined through the relation

$$\epsilon(T) = \frac{\pi^2}{30} \nu(T) T^4 \tag{1.5}$$

where $\epsilon(T)$ is the energy density of the medium. For the sake of context, one should consider that an ideal gas of ultra-relativistic pions (the lightest hadrons) has $\nu = 3$, while an ideal gas of gluons and three flavors of massless quarks has $\nu = 47.5$ [3]. Thus one expects to see a significant increase in ν as the transition from hadronic bound states to deconfined quarks and gluons occurs. As is obvious from the form of (1.5), ν can be determined from the ratio $\epsilon(T)/T^4$, whereas $\epsilon(T)$ can be determined

from the QCD partition function, $Z(\beta, V)$, via the relation

$$\epsilon = -\frac{1}{V} \left(\frac{\partial Z}{\partial \beta} \right)_V \quad (1.6)$$

where V is volume and $\beta = T^{-1}$. By calculating $Z(\beta, V)$, and in turn $\epsilon(T)$, $\nu(T)$ can be established, providing an excellent probe of whether or not, and at what temperature, the transition occurs.

The QCD partition function can be written down in terms of the Lagrangian (1.1) as

$$Z(\beta, V) = \int \mathcal{D}A \mathcal{D}\psi \mathcal{D}\bar{\psi} \exp \left[- \int dV \int_0^\beta d\tau \mathcal{L} \right] \quad (1.7)$$

where \mathcal{D} signifies functional integration and τ is the imaginary time. While the above expression looks straightforward, its evaluation is very difficult and can only be done in certain idealized approximations. One such approximation is to expand the exponential term in (1.7) in powers of the strong coupling, $\alpha_s = g^2/4\pi$, which makes sense provided $\alpha_s \ll 1$. This *perturbative* expansion allows the partition function to take on a Gaussian form which can be handled analytically, albeit with much subtlety and effort. The running coupling, (1.4), ensures that α_s will grow as T is lowered, limiting the use of perturbation theory to regions of high temperature. To calculate $Z(\beta, V)$ over a wide range of temperatures, which is required to establish that a transition has occurred, it is necessary to use an evaluation technique that is not limited to small values of α_s .

The only available tool which can do this is lattice QCD, where the partition function, (1.7), is evaluated numerically by dividing the continuous space of V, τ into a discretized lattice. I will not discuss the specifics of how QCD is evaluated on the lattice here, but the reader can see [4] for an introduction. In what immediately follows results are shown from lattice calculations which are representative of what

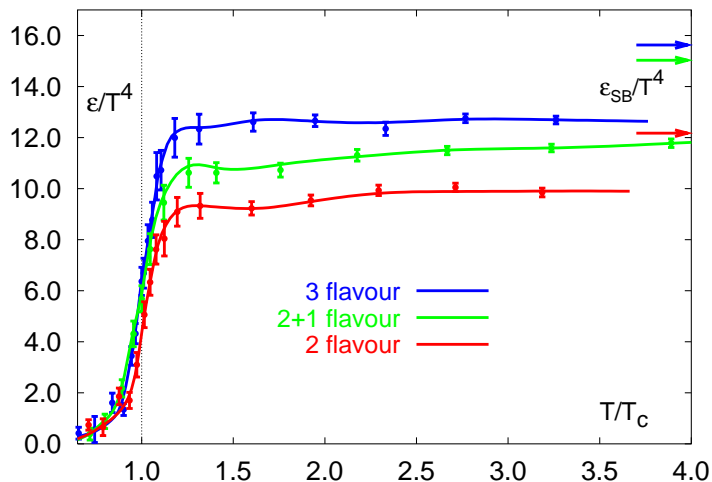


FIGURE 1.1: $\epsilon(T)/T^4 \sim \nu(T)$ as a function of temperature [5]. The curves are a measure of the number of thermodynamic degrees of freedom in the medium, which show a sharp increase in the vicinity of $T = T_c$.

is currently understood about the behavior of strongly interacting matter at high temperature, that is, the QGP. The result for $\epsilon(T)/T^4 \sim \nu(T)$ as obtained from [5] is shown in Fig. 1.1. The calculation was performed with improved staggered fermions for 2 massless flavors of quarks, 3 massless flavors of quarks, and 2+1 flavors, which indicates 2 massless flavors and one massive flavor. The result is plotted as a function of T/T_c , where for 2 flavors $T_c = 173$ MeV and for 3 flavors $T_c = 154$ MeV, which is roughly 10^{12} Kelvin. The curves, which, as was discussed above, are a direct measure of the number of thermodynamic degrees of freedom in the medium, show a sharp increase in the vicinity of $T = T_c$, and then asymptotically approach the Stefan-Boltzmann limit for an ideal gas of non-interacting quarks and gluons, which is indicated by the arrows. This is strong evidence for a transition from hadrons to deconfined quarks and gluons at $T = T_c$.

If the transition observed in Fig. 1.1 is a result of deconfinement, there must be an order parameter associated with it. It has been shown [6] that the order parameter of the deconfinement transition is the expectation value of the Polyakov loop, $\langle L \rangle$,

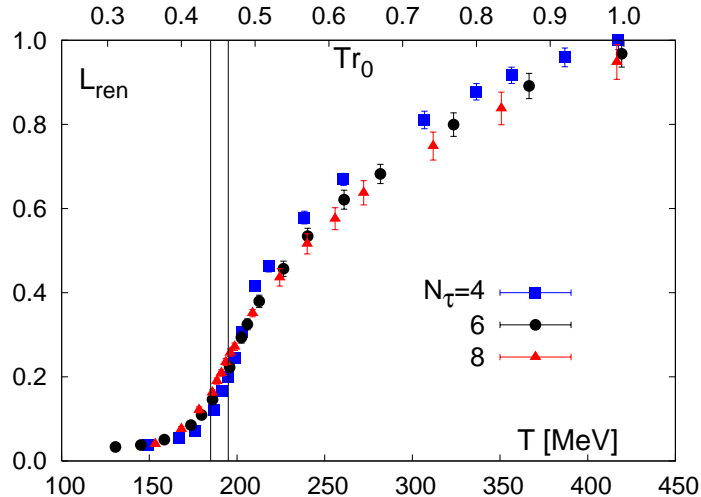


FIGURE 1.2: The renormalized result for $\langle L \rangle$ as a function of temperature [7]. The sharp rise around $T = 190$ MeV indicates the onset of deconfinement.

which is related to the free energy, F , of a static test quark

$$\langle L \rangle \sim e^{-\frac{F}{T}}. \quad (1.8)$$

The free energy measures the amount of energy required to place the test quark in a thermal medium of gluons. As long as we consider only infinitely massive quarks, this energy will be infinite in the confined phase, and finite in the deconfined phase, such that

$$\begin{aligned} \langle L \rangle &= 0 \text{ confined phase,} \\ \langle L \rangle &\neq 0 \text{ deconfined phase.} \end{aligned} \quad (1.9)$$

The situation becomes slightly more complicated when we allow for quarks with finite mass, since then the free energy is large, but not infinite, in the confined phase. However, the behavior is similar to (1.9), and $\langle L \rangle$ is still a good probe of the deconfinement transition. The result for the renormalized expectation value of the Polyakov loop as obtained from lattice calculations presented in [7] is shown in Fig. 1.2, where the calculation includes light quarks. The figure shows results for different values of N_τ , which refers to the number of lattice intervals in the imaginary

time integration. The result shows a sharp increase in $\langle L \rangle$ around $T = 190$ MeV, consistent with what might be expected from (1.9). One concludes that the transition observed in Fig. 1.1 is associated with the onset of deconfinement.

There is a second order parameter in the QGP transition which is a result of the restoration of chiral symmetry [8]. In the limit of $m_f \rightarrow 0$, the QCD Lagrangian, (1.1), preserves the chirality of quarks, where left/right handed chirality is defined through application of the pseudoscalar Dirac matrix, γ^5 :

$$\psi_{L/R} = \left(\frac{\mathbf{1} (-/+) \gamma^5}{2} \right) \psi. \quad (1.10)$$

Even for massless quarks, chiral symmetry is spontaneously broken in the QCD vacuum by the formation of a quark/anti-quark condensate, $\langle \bar{\psi}\psi \rangle$. The term *spontaneously broken* here indicates that even though the original Lagrangian has chiral symmetry (in the case of massless quarks), interactions spontaneously generate a non-zero value of $\langle \bar{\psi}\psi \rangle$ which breaks the original chiral symmetry. At high temperature or net baryon density, $\langle \bar{\psi}\psi \rangle$ tends to zero and chiral symmetry is restored. This 'melting' of the chiral condensate occurs for perhaps the same reason deconfinement occurs: as the result of an increased color charge density in the medium. Whatever the detailed nature of their relationship, it is widely believed that these two transitions occur simultaneously. A useful quantity to measure the restoration of chiral symmetry is given by

$$\Delta_{l,s}(T) = \frac{\langle \bar{\psi}\psi \rangle_{l,T} - \frac{m_l}{m_s} \langle \bar{\psi}\psi \rangle_{s,T}}{\langle \bar{\psi}\psi \rangle_{l,0} - \frac{m_l}{m_s} \langle \bar{\psi}\psi \rangle_{s,0}} \quad (1.11)$$

where the subscript $0, T$ refers to the temperature, and the subscript l, s refers to quark flavor (l being the nearly massless u and d quarks, s being the massive strange quark). As chiral symmetry is restored, $\Delta_{l,s}$ will drop and approach zero. The result for (1.11) given by [7] is shown in Fig. 1.3, where one indeed sees the chiral transition at about $T = 190$ MeV.

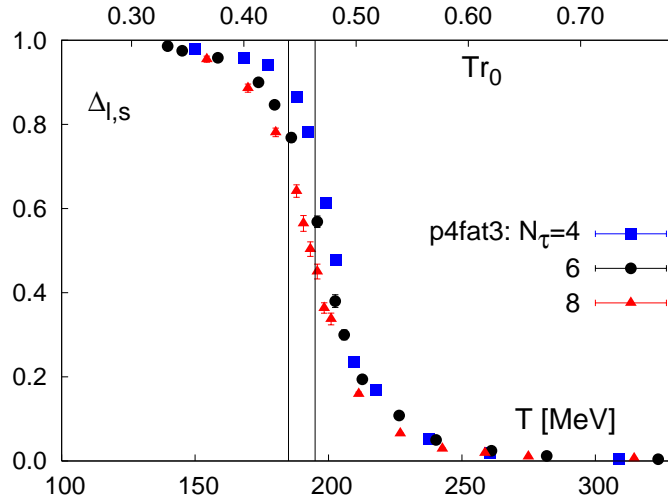


FIGURE 1.3: $\Delta_{l,s}$ as a function of temperature [7]. As discussed in the text, the result suggests the restoration of chiral symmetry at about $T = 190$ MeV.

It is important here to point out that the values of T_c listed above are not rigorously established, but rather give an idea as to where the transition occurs. Indeed, the transition occurs over a finite width of temperature, leaving some freedom in how to define where T_c occurs. A common choice is to define T_c at the steepest point in the transition. When this is done, it is found that the chiral transition and deconfinement occur at the same temperature, within numerical uncertainty, justifying the idea that these two transitions occur simultaneously. The most recent calculations [9] suggest $180 \leq T_c \leq 200$ MeV.

The picture emerges that QCD matter undergoes a transition from hadronic bound states to deconfined quarks and gluons at a temperature of about 190 MeV and zero baryon chemical potential, μ_B . A commonly used QCD phase diagram is shown in Fig. 1.4, where one can also get a sense of the μ_B dependence of the phase structure. I have been careful not to use the term *phase transition*, since the QGP transition at $\mu_B = 0$ is now thought to be continuous in all of its thermodynamic quantities. Generally, a phase transition is characterized by some non-analyticity in the thermodynamic variables.

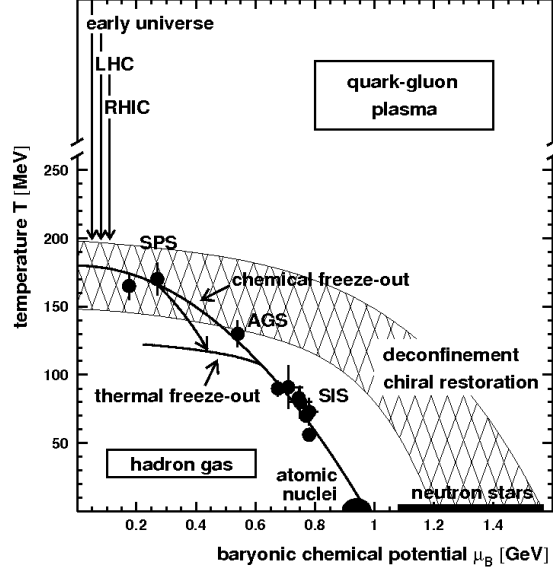


FIGURE 1.4: Phase diagram of QCD [10].

Before moving on, it is worthwhile to consider some additional properties of the QGP which have been calculated on the lattice and are presented in [11]. The first of these is the strong coupling, α_s , which is shown in Fig. 1.5 as a function of distance for given temperatures. In the plot, $\alpha_{q\bar{q}}$ is defined through the free energy of a static quark anti-quark pair

$$\alpha_{q\bar{q}}(r, T) = \frac{3r^2}{4} \frac{dF(r, T)}{dr}. \quad (1.12)$$

Consider, for example, the points corresponding to $T = 1.98 T_c$. Here, $\alpha_s \sim 0.3$ at $r = 0.3$ fm, and tends toward zero as r becomes large. This large r behavior reflects what was mentioned earlier, that the high density of color charges in the plasma phase creates a screening effect such that the long distance, confining growth

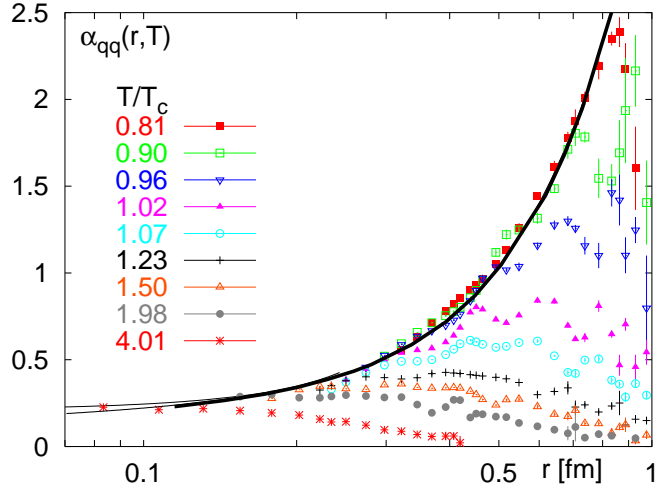


FIGURE 1.5: The strong coupling, α_s , as a function of distance for given temperatures [11].

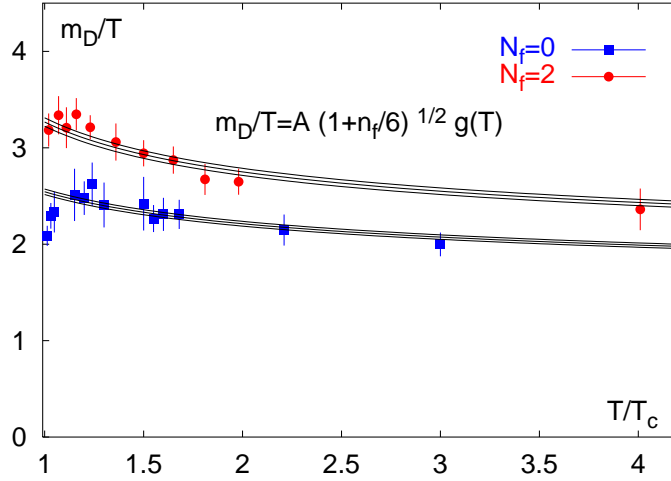


FIGURE 1.6: A lattice result for the Debye screening mass divided by temperature, m_D/T , [11]. Roughly speaking, a potential, $V(r)$, at $T = 0$ will be suppressed by a factor of $e^{-m_D r}$ at finite temperature.

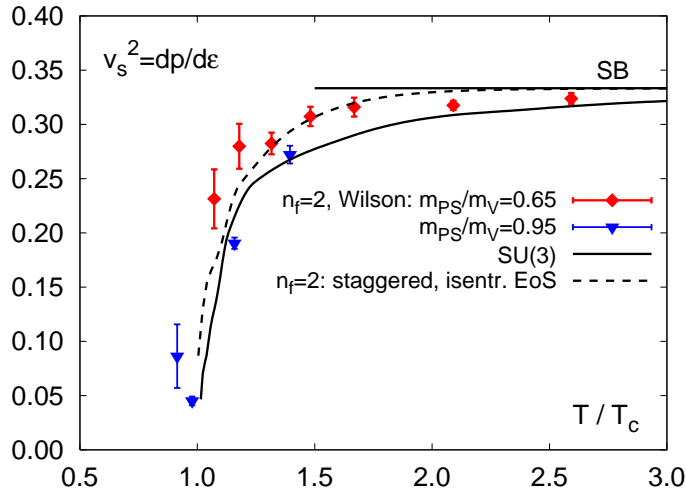


FIGURE 1.7: Speed of sound as a function of temperature [11].

of the coupling constant is no longer important. A measure of the strength of the in-medium screening is given by the Debye mass, m_D . Roughly speaking, a potential, $V(r)$, at $T = 0$ will be suppressed by a factor of $e^{-m_D r}$ at finite temperature. In perturbation theory, the Debye mass has the form

$$m_D^2 = \frac{1}{3}(N_c + \frac{1}{2}N_f)g^2 T^2, \quad (1.13)$$

which gives $m_D/T \sim 2$ for $N_f = 0$ and $\alpha_s = 0.3$. The lattice result for m_D/T is shown in Fig. 1.6.

Finally, the speed of sound, $c_s^2 \equiv \partial p / \partial \epsilon$, is shown in Fig. 1.7 (there labeled as v_s). The curves approach the Stefan-Boltzmann limit of $c_s^2 = 1/3$ at large T , but are much smaller near $T = T_c$. The speed of sound is interesting as it provides information on the equation of state. It is also directly relevant to the work presented in this thesis, which will focus on sound waves generated by supersonic particles in the plasma as is discussed below.

1.2 Experimentally Probing the Quark-Gluon Plasma

For quite some time now it has been predicted that the quark gluon plasma can be formed experimentally in relativistic heavy-ion collisions [12]. In particular, the heavy-ion program at the Relativistic Heavy-Ion Collider (RHIC) at Brookhaven National Lab, and the future program at the Large Hadron Collider (LHC) at CERN, are believed to produce matter that extends well into the QGP phase. These two experimental programs are indicated on the phase diagram in Fig. 1.4, where it is seen that they are expected to produce matter with high temperature and very low baryon chemical potential.

RHIC began operating in the summer of 2000 and has since provided a wealth of experimental data which has shaped the current understanding of QCD matter at high temperature. RHIC's heavy-ion program collides two gold nuclei at a peak center of mass energy of 200 GeV per nucleon. A simple estimate for the initial energy density in such a collision can be made using the *Bjorken energy density* [12] (named for the author who first derived it)

$$\epsilon_{Bj} = \frac{\langle E \rangle}{\tau_F A} \frac{dN}{dy} \quad (1.14)$$

where $\langle E \rangle$ is the average energy of the interacting particles, A is the nuclear overlap area, y is the rapidity, τ_F is the formation time, and N is the number of interacting particles. For a formation time of 1 fm/c and using a naive extrapolation of $p + p$ (proton) data for the input parameters, one estimates that $\epsilon_{Bj} \approx 5 \text{ GeV/fm}^3$ for the highest energy $Au + Au$ (gold) collisions at RHIC, well above the required $\epsilon_c \approx 1 \text{ GeV/fm}^3$ required to form the QGP (ϵ_c is here used as the critical energy density of the QGP transition, a value which can be obtained from Fig. 1.1). While ϵ_{Bj} can only provide an order of magnitude estimate for the initial energy density, it suggests that $Au + Au$ collisions at RHIC are able to probe the QGP.

The four experimental collaborations at RHIC: BRAHMS, PHOBOS, STAR, and PHENIX, have published *white* papers [13, 14, 15, 16] which give a summary of the significant experimental results obtained to that point in time (2005). The results indicate “that the state of matter created at RHIC cannot be described in terms of ordinary color neutral hadrons” [16], but rather that the QGP has been formed. Detailed experimental analysis reveals the initial energy density of the created medium to be greater than $15 \text{ GeV}/\text{fm}^3$, much higher than the value needed to form the deconfined phase. It is not possible to give a rigorous review of all of the important results obtained so far from RHIC here, so instead I will focus on three which are directly relevant to the rest of this thesis.

The first of these is the nearly ideal fluid behavior apparently exhibited by the medium. The primary evidence for ideal fluidity comes from measurements of the *elliptic flow*, v_2 . Elliptic flow is generated by an initial spatial anisotropy in the heavy-ion collision caused by an incomplete overlap of the colliding nuclei. The amount of anisotropy is characterized by the centrality, with the most central collisions having the least anisotropy, and most participating nucleons. The initial spatial distribution of the interacting matter takes the form of an ellipsoid. If the medium thermalizes quickly, then the initial anisotropy creates a pressure gradient which is strongest along the shortest direction of the ellipsoid. The spatial anisotropy can be characterized by the eccentricity, ε , which is given by

$$\varepsilon = \frac{\langle y \rangle^2 - \langle x \rangle^2}{\langle y \rangle^2 + \langle x \rangle^2} \quad (1.15)$$

where x and y are the directions transverse to the beam axis and $\langle \rangle$ refers to the spatial average of participating nucleons. v_2 is defined through the azimuthal distri-

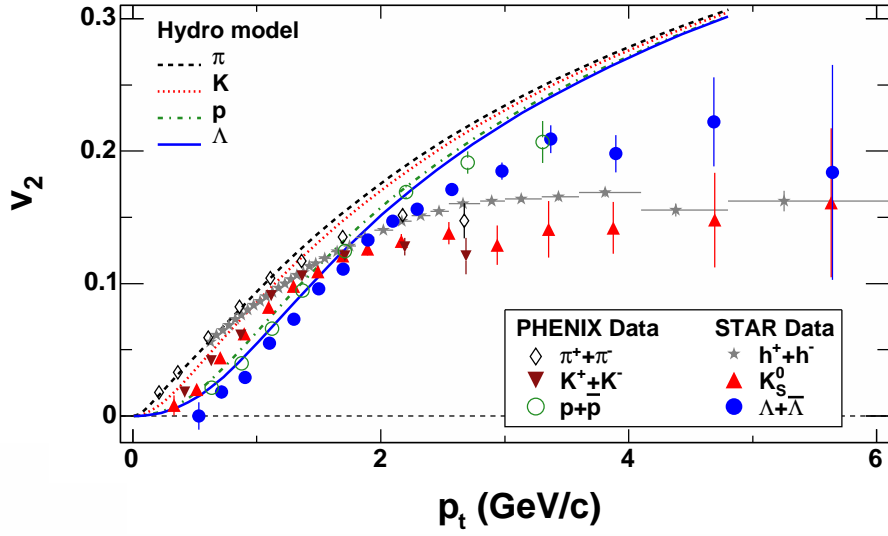


FIGURE 1.8: Elliptic flow data from experiment along with predictions from an ideal hydrodynamics calculation [18]. There is good agreement between the data points and the ideal hydro predictions for $p_t \lesssim 2$ GeV.

bution of emitted particles [17]

$$\frac{dN}{d(\phi - \Phi_R)} \propto \left(1 + \sum_{n=1}^{\infty} 2v_n \cos[n(\phi - \Phi_R)] \right) \quad (1.16)$$

where Φ_R is the azimuth of the reaction plane. The success of ideal relativistic fluid dynamics to reproduce the elliptic flow data seen at RHIC has led to the idea that the QGP is a nearly ideal fluid. Figure 1.8, taken from [18], shows elliptic flow data from both STAR and PHENIX, along with predictions from an ideal hydrodynamics calculation. One sees good agreement between the data points and the ideal hydrodynamics predictions up until $p_t \approx 2$ GeV.

Deviations from ideal fluidity are quantified by the viscosity of the medium. Much effort has been given to extracting the dimensionless ratios of the shear viscosity to entropy density, η/s , and the bulk viscosity to entropy density, ζ/s , of the QGP. It is believed that η/s is much larger than ζ/s except in the vicinity of T_c [19] for the QGP, hence that is where most of the attention has been placed. Viscous

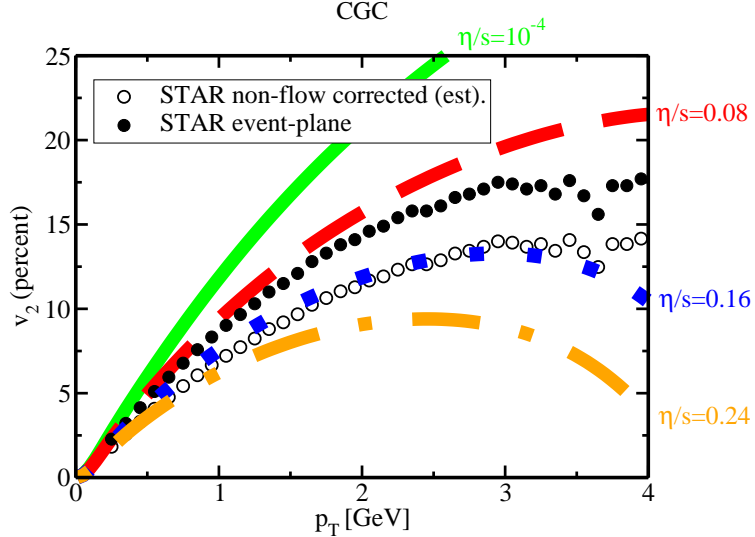


FIGURE 1.9: A viscous hydrodynamics calculation for different values of the shear viscosity to entropy density ratio along with a comparison to experimental data [20]. From the curves, it appears that the choice of $\eta/s \approx 0.16$ matches the non-flow corrected data for $p_t \lesssim 3$ GeV.

hydrodynamics calculations which include non-vanishing shear viscosity have been performed and compared to experimental data. The results of one such calculation are shown in Fig. 1.9. In the plot, the filled circles are the raw experimental data and the open circles are the same data corrected for non-flow effects. One sees that with the choice of $\eta/s \approx 0.16$ the non-flow corrected data is well reproduced by viscous hydrodynamics. This number is remarkably small. For comparison, the η/s for water under normal conditions is roughly 180 times larger than this value. The value for η/s which seems to describe the QGP data is not much larger than $1/4\pi \approx 0.08$, which has been proposed [21] as a universal lower bound for all relativistic quantum field theories and is calculated for a large N_c SUSY Yang-Mills plasma in the strongly coupled limit using the AdS/CFT correspondence. The QGP produced at RHIC is arguably the most ideal fluid ever observed experimentally.

The second important experimental result I will here discuss is the suppression of high transverse momentum hadrons in relativistic heavy-ion collisions when com-

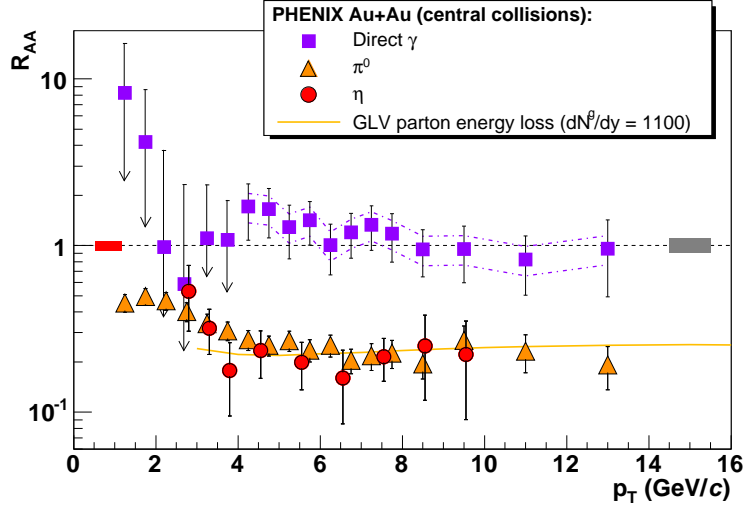


FIGURE 1.10: The nuclear modification factor, R_{AA} , which quantifies the suppression of high p_T particles in heavy-ion collisions relative to an incoherent superposition of $p+p$ collisions [22]. The strongly interacting particles, π^0 and η , show a noticeable suppression, whereas direct photons are largely unaffected.

pared to $p+p$ data. Early in a heavy-ion collision two partons may scatter at a large angle relative to the beam direction and propagate with high transverse momenta through the newly formed medium. The effect of the medium on these high energy partons is quantitatively expressed in terms of the *nuclear modification factor*, R_{AA} , which gives the ratio of the measured yield of high p_T hadrons produced in heavy-ion collisions divided by the same yield from an incoherent superposition of $p+p$ collisions, i.e.

$$R_{AA}(p_T) = \frac{d^2N_{AA}/dp_T dy}{\langle T_{AA} \rangle \cdot d^2\sigma_{pp}/dp_T dy} \quad (1.17)$$

where $\langle T_{AA} \rangle$ is the Glauber nuclear overlap function. The PHENIX measurement of R_{AA} for the most central $Au + Au$ collisions at RHIC is shown in Fig. 1.10. Here one sees significant suppression of pions and etas, with $R_{AA} \approx 0.2$. Compare this to the direct photon production, which stays close to $R_{AA} \approx 1$. The picture emerges that high energy particles which interact with the QCD medium, that is the QGP, lose substantial amounts of energy, and are suppressed, or quenched. This

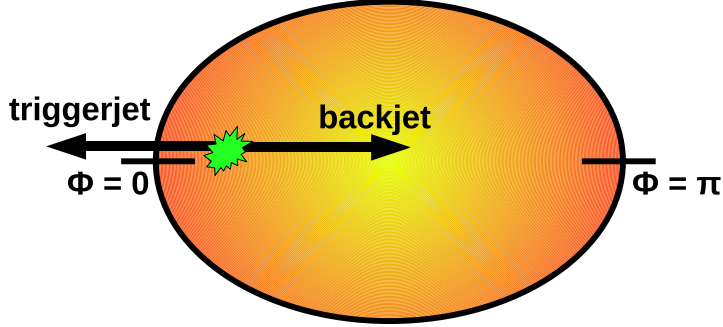


FIGURE 1.11: Early in the heavy-ion collision two partons may scatter at a large angle relative to the beam direction and propagate back to back through the medium, which is represented in the figure.

phenomenon, known as *jet quenching*, is one of the most striking results from the heavy-ion program at RHIC.

Jet quenching can be further illuminated by examining azimuthal hadron correlation measurements. As discussed in the previous paragraph, early in the heavy-ion collision two partons may scatter at a large angle relative to the beam direction and propagate back to back through the medium. If this initial scattering occurs near the surface of the nuclear medium, one of the partons, known as the trigger jet, may escape quickly and be easily observed as a high momentum hadron by detectors, while the other parton, known as the back jet, travels through the medium losing energy and momentum. This scenario is illustrated in Fig. 1.11. As can be seen from the figure, in terms of an azimuthal angle ϕ , the trigger jet defines the direction of $\phi = 0$, and the back jet propagates in the direction of $\phi = \pi$. In the figure, the back jet propagates parallel to the collision plane, however the direction of propagation could be in any orientation. A trigger jet is observed experimentally by looking for a hadron in some high p_T bin. Once a trigger jet is observed, azimuthal di-hadron correlation measurements look for secondary, or associated, high momentum hadrons as a function of azimuthal angle relative to the trigger. For instance, the overall

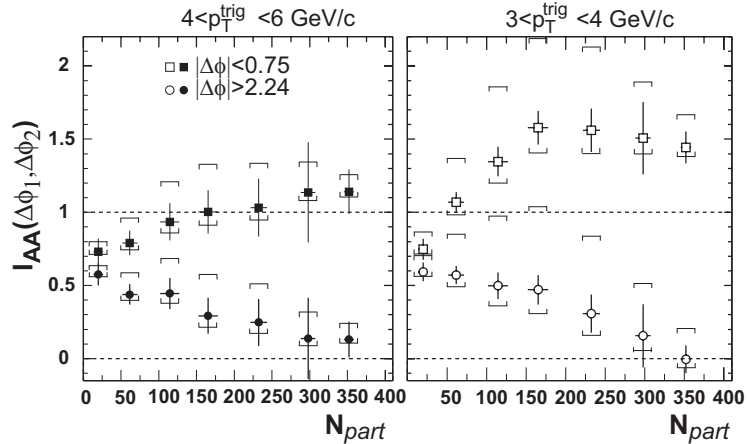


FIGURE 1.12: I_{AA} gives the ratio of the measured Au + Au correlation excess relative to the p + p correlation in the given azimuthal interval [23]. One sees significant suppression in the away side I_{AA} . The horizontal bars indicate the dominant systematic error.

azimuthal pair distribution per trigger particle

$$D(\phi) \sim \frac{1}{N_{trigger}} \int d\eta N(\phi, \eta) \quad (1.18)$$

quantifies the azimuthal distribution of secondary hadrons, where $N_{trigger}$ is the number of trigger jets and the integral is over the space-time rapidity. In terms of $D(\phi)$, the ratio of the measured Au + Au correlation excess relative to the p + p correlation in some azimuthal interval is given as

$$I_{AA}(\phi_1, \phi_2) = \frac{\int_{\phi_1}^{\phi_2} d\phi D^{Au+Au}(\phi)}{\int_{\phi_1}^{\phi_2} d\phi D^{p+p}(\phi)}. \quad (1.19)$$

As with R_{AA} , I_{AA} has a straightforward physical interpretation: it should be unity if the hard-scattering component of Au + Au collisions is a superposition of p + p collisions unaffected by the nuclear medium. In other words, I_{AA} describes the quenching of secondary hadrons per trigger. The STAR collaboration has published data on I_{AA} [23] which is shown in Fig. 1.12. In the left panel the momentum of the trigger hadron is between 4 and 6 GeV whereas in the right panel it is between

3 and 4 GeV. In both cases the momentum of the associated hadron is in the range $2 \text{ GeV} < p_T < p_T^{Trig}$. Each panel has two sets of data points, one gives the I_{AA} value when integrating over the interval $|\phi| < 0.75$, and the other when integrating over the interval $|\phi| > 2.24$ (where ϕ ranges from $-\pi$ to π). Physically, the interval $|\phi| < 0.75$ represents the contribution from the direction of the trigger jet, whereas $|\phi| > 2.24$ gives the contribution from the back jet. The values are plotted as a function of the number of participating nucleons, N_{part} . It is clear from the plots that the I_{AA} associated with the back jet decreases with increasing N_{part} , whereas the I_{AA} associated with the trigger jet actually increases or remains constant. The interpretation is that back jets, which have to propagate through the dense medium, deposit large amounts of energy and are quenched.

Both the R_{AA} and I_{AA} data indicate that highly energetic, or fast, partons deposit large amounts of energy and momentum as they propagate through the QGP. It has also been shown above that the QGP appears to be a nearly ideal fluid with strong collective flow. In light of these two facts, it is natural to think that fast partons may induce collective flow in the medium. The overall azimuthal pair distribution per trigger particle, $D(\phi)$ mentioned above, may shed light into the medium's response to fast partons. The medium response to fast partons should manifest itself in the distribution around $\phi = \pi$, which is the direction of the back jet propagation (Fig. 1.11), or the *away side*. Fig. 1.13 shows the overall azimuthal pair distribution per trigger particle as published by PHENIX in [24] for $p + p$ collisions in the upper panel, and the 20 percent most central collisions for RHIC $Au + Au$ collisions in the lower panel. The numbers in the upper right hand corner of the plots indicate the particular momentum bins for the trigger and the away side hadrons, respectively. There is a noticeable difference in the distributions of $p + p$ compared to $Au + Au$ around $\phi = \pi$. There, the $p + p$ spectrum shows a simple broad Gaussian peak whereas the $Au + Au$ spectrum has a double-peak structure, with $\phi = \pi$ being a local

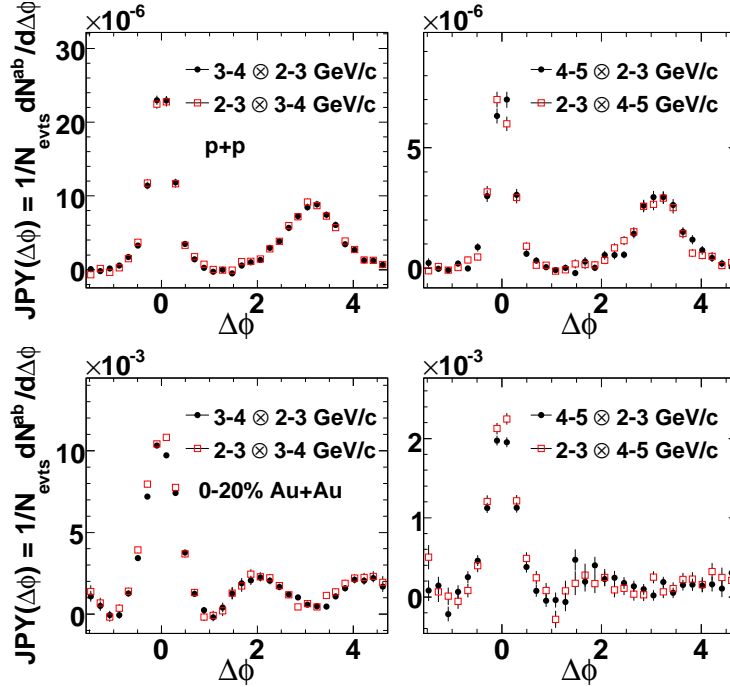


FIGURE 1.13: The overall azimuthal pair distribution per trigger particle [24] for $p + p$ collisions (upper panel), and the 20 percent most central collisions for RHIC $Au + Au$ collisions (lower panel). The distribution for RHIC $Au + Au$ collisions is double-peaked around the away side ($\Delta\phi = \pi$).

minimum. The behavior of the di-hadron correlation measurements has generated much interest in understanding the response of the QGP medium to fast partons. Many have speculated that the double-peak structure observed in the away side distribution is generated by collective, Mach-like, conical flow induced by the fast parton in the medium.

The complete picture is, however, more complicated. The structure of the away side distribution depends strongly on the momentum bins, particularly of the trigger hadron. It is also sensitive to the centrality of the initial heavy-ion collision. These facets are highlighted in the overall azimuthal pair distribution per trigger particle shown Figs. 1.14 and 1.15, also published in [24]. For instance, consider the plots marked $2 - 3 \otimes 1 - 2$ in Fig. 1.14, which shows the data from the 20 percent most central collisions, and Fig. 1.15, which shows the data from the 60-92 percent most

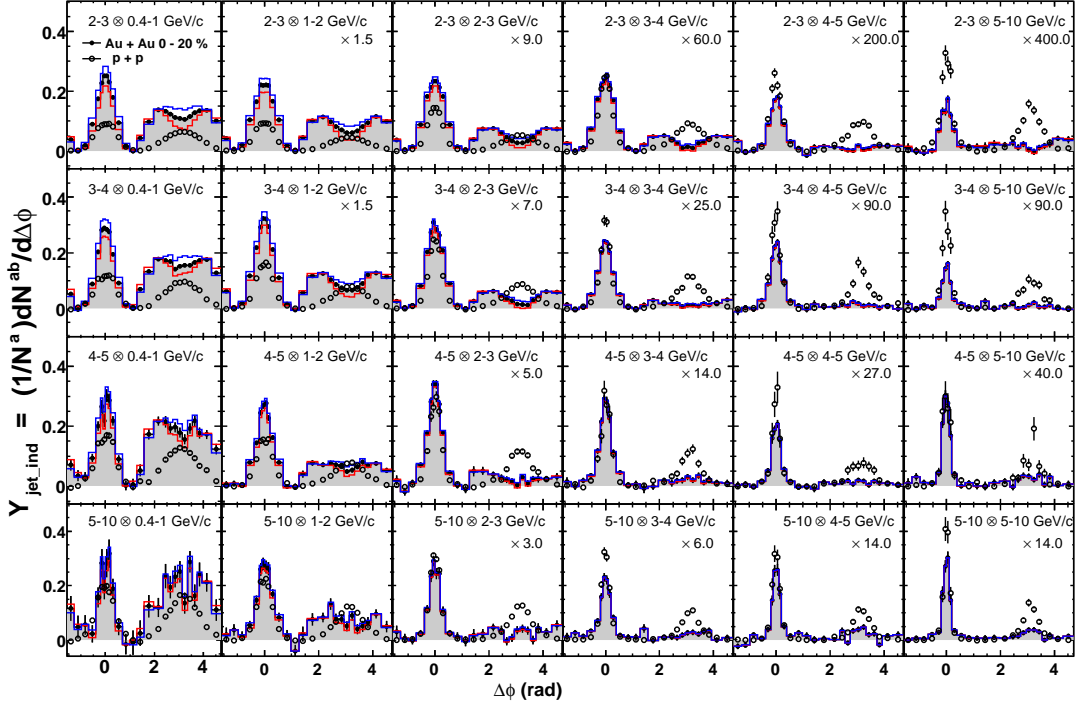


FIGURE 1.14: Azimuthal di-hadron correlations from the 20 percent most central $Au + Au$ collisions at RHIC for a wide range of momentum bins [24]. Compare to Figure 1.15 which shows data from less central collisions.

central collisions (which are some of the least central collisions). A quick inspection shows the away side distribution is substantially altered when going from the most central to the least central collisions, with the double-peak structure disappearing in the least central collisions. Recall from the discussion above on elliptic flow that the more central collisions have more participating nucleons, and hence a larger nuclear medium. One is led to conclude that the double-peak structure observed in the away side distribution of the most central collisions is associated with a medium effect.

Now consider the second column in Fig. 1.14, starting with the plot marked $2 - 3 \otimes 1 - 2$ GeV/c, and scrolling down through the subsequent plots ending at the plot marked $5 - 10 \otimes 1 - 2$ GeV/c. As mentioned above, these numbers indicate the particular momentum bins for the trigger and away side hadrons, respectively. It's clear that as the trigger hadron momentum is increased, the away side distribution

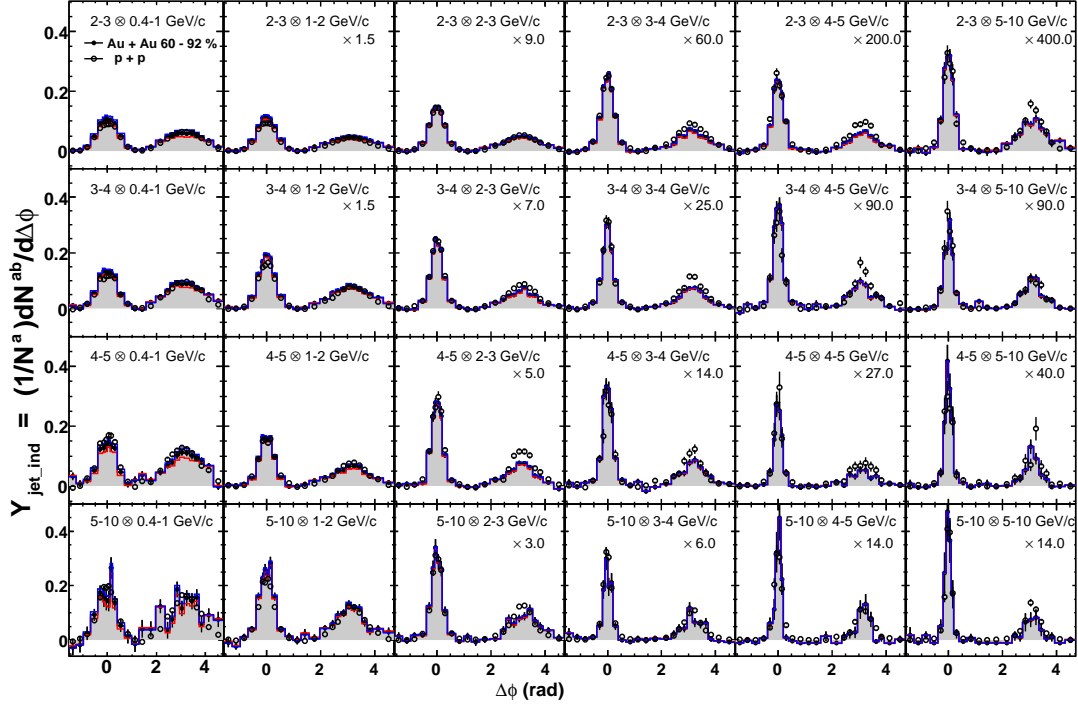


FIGURE 1.15: Azimuthal di-hadron correlations from the 60-92 percent most central $Au + Au$ collisions at RHIC for a wide range of momentum bins [24]. Compare to Figure 1.14 which shows data from the most central collisions.

changes shape and the double-peak structure is significantly altered, even though the away side hadron momentum is the same. Recall the scenario illustrated in Fig. 1.11. Due to conservation of momentum, as the trigger hadron momentum is increased, the back jet momentum must also increase. If the initial momentum of the back jet is large enough, it will propagate all the way through the medium, and escape on the away side, in which case the away side distribution should be dominated by the jet. On the other hand, if the back jet does not have enough momentum, it will be absorbed by the medium, in which case the away side distribution should be dominated by the medium's response to the jet. We are again led to conclude that the double-peak structure observed in the away side distribution is associated with a medium effect, presumably observable when the back jet is absorbed by the medium.

In terms of the underlying physics there are two straightforward, yet significantly

different interpretations of the double-peak structure in the away side distribution. One is that a fast parton propagating through the medium is deflected by the medium such that the final associated hadron spectrum gets shifted away from $\phi = \pi$ (this is discussed in [25, 26]). This picture is commonly called *the deflected jet scenario*, and suggests that the double-peak structure on the away side of the di-hadron correlations is the result of averaging over many events. In any single event, the probability of observing a hadron would be a single peak distribution displaced from $\phi = \pi$. When averaged over many events, the double-peak arises because the direction of the deflection is randomly distributed.

The second interpretation is that the fast parton creates a medium response such that the final associated hadron spectrum becomes split with respect to $\phi = \pi$. This picture is typically associated with a conical hadron emission spectrum, in which case the structure on the away side of the di-hadron correlations is legitimately double-peaked. In other words, in any single event, the probability of observing a hadron would be a double-peak distribution symmetric about $\phi = \pi$. Two examples of this scenario which I will discuss in the next chapter are Cerenkov radiation and Mach cone induced flow. Three-hadron correlation measurements seem to rule out the deflected jet scenario, and favor instead a conical emission pattern. In these measurements, as with the di-hadron correlations, a high p_T hadron serves as a trigger, but now one looks for two associated hadrons instead of just one. Plots a), b), and c) in the upper panel of Fig. 1.16 provide a simple schematic of what three-hadron correlations might look like in different physical scenarios. Notice that there are now two ϕ axes to consider, one for each of the observed secondary hadrons. Plot a) demonstrates what a simple back-to-back jet scenario would look like, where one only sees peaks at $(\phi_1, \phi_2) = (0, 0)$, $(\phi_1, \phi_2) = (\pi, \pi)$, $(\phi_1, \phi_2) = (\pi, 0)$, and $(\phi_1, \phi_2) = (0, \pi)$, each corresponding to observing hadrons in either the trigger or away side directions, or one in the trigger direction and one in the away side direction

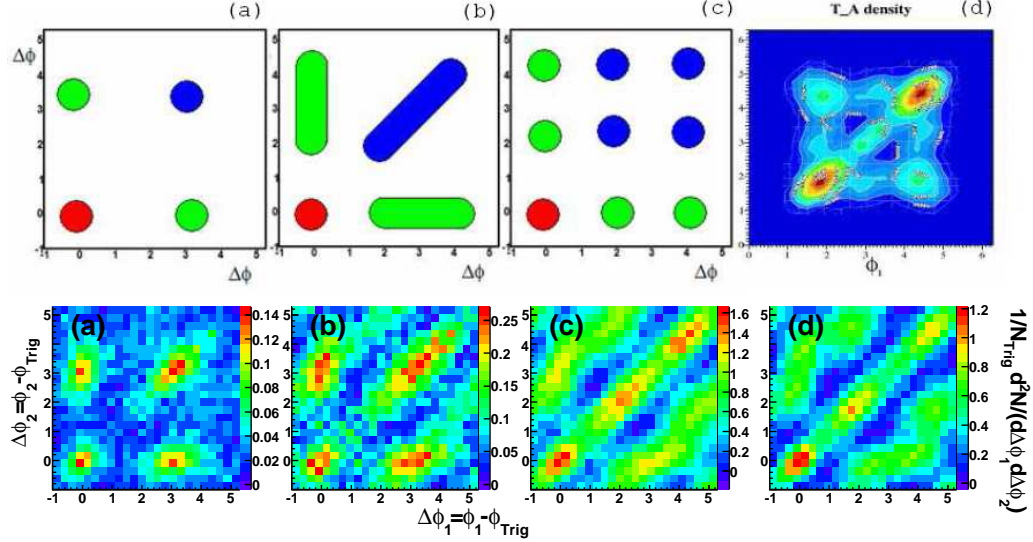


FIGURE 1.16: In the upper panel, simple schematics of what three-hadron correlations might look like for a), a simple back-to-back jet scenario, b), the deflected jet scenario and c), the conical emission scenario. Plot d) in the upper panel is a simulation of the emission pattern expected from conical flow given in [37]). The lower panel shows experimental data presented in [27]. Plot a) is three-hadron correlation data from $d + Au$ experiments, while plots b), c) and d) are the data from $Au + Au$ for increasing number of participating nucleons, with plot d) having the most participants.

(it may be helpful to review Fig. 1.11). In plot b) one sees the deflected jet scenario illustrated. Here one finds a structure not dissimilar to the back-to-back jet scenario, except that now the peaks associated with the away side ($\phi = \pi$) are smeared out. Finally, in plot c) the conical emission scenario is shown. Notice in particular the blue dots, which are associated with the away side distribution. There are two off-diagonal peaks which are unique to the conical flow scenario and are not seen in either plot a) or b) (for the curious reader, plot d) in the upper panel is a simulation of the emission pattern expected from conical flow given in [37]). These two off-diagonal peaks provide a way to establish that the double-peak structure observed in the di-hadron correlation measurements are legitimately double-peaked.

Now consider the lower panel of Fig. 1.16, which shows experimental data pre-

sented in [27]. Plot a) shown in the lower panel is three-hadron correlation data from $d + Au$ experiments, while plots b), c) and d) are the data from $Au + Au$ for an increasing number of participating nucleons, with plot d) having the most participants. In all plots the momentum of the trigger hadron is between 3 and 4 GeV whereas the momentum of the associated hadron is in the range $1 < p_T < 2$ GeV. For $d + Au$ collisions, where no thermal medium is formed, the data looks very similar to the back-to-back scenario discussed above. However, for the $Au + Au$ data with the most participants, the away side distribution has a similar form as the conical emission scenario discussed above, in particular, the two off-diagonal peaks indicative of conical flow are present. From the above considerations one is led to believe that the double-peak structure seen in the di-hadron correlations is generated by a conical emission pattern. Further in-depth analysis presented by the STAR collaboration [28] on three-hadron correlations also suggest the away side hadron distribution is best interpreted as the result of a conical emission pattern.

The picture is now emerging that fast partons propagating in the QGP interact strongly with the medium, and perhaps induce a medium effect which is observable as a conical structure in the away side distribution of hadron correlation measurements. In the next chapter, I will discuss two possible physical mechanisms to produce a conical away side spectrum and then motivate the technical aspects of this thesis which follow.

Investigating the Medium Response: Overview

In the previous chapter a broad introduction to the QGP was presented as well as some interesting results seen from experiments performed at RHIC. In this chapter I will expand upon one of these results, specifically, the conical structure in the away side distribution observed in hadron correlation measurements. In what follows, I will present two of the proposed mechanisms for generating such a structure, and offer some insights into the efficacy of each mechanism. Then I will discuss the approaches implemented in the rest of this thesis for investigating the response of the QGP to fast partons.

2.1 Two Mechanisms for Conical Emission

As discussed in the previous chapter, two commonly proposed mechanisms for generating a conical hadron emission spectrum are Cerenkov radiation and Mach cone induced flow. It is useful here to review the classical picture of Cerenkov induced radiation. When a fast charged particle travels through a dielectric medium it induces a temporary polarization in the surrounding molecules. As the temporary polarization decays, the changing fields of the constituent molecules emit radiation.

The condition for this to become Cerenkov radiation is that the velocity of the initial fast charged particle be greater than the phase velocity of light in the medium, in which case the radiation combines coherently and forms a propagating cone. The possibility of a fast parton to induce Cerenkov gluon radiation in the QGP has been investigated in [29, 30]. The scenario turns out to be somewhat more complicated than what is briefly outlined above, however, many features are similar. The primary restriction on Cerenkov induced radiation is that the medium consist of bound states which facilitate resonant scattering of the radiated gluons. This restriction poses difficulty for the QGP, where one is not likely to find bound states, except perhaps in the region of $T \approx T_c$. However, the biggest problem for Cerenkov induced radiation is the predicted strong angular dependence of the emission angle on hadron momentum, which arises from the momentum dependence of the dielectric screening. One expects the opening angle of the cone to decrease as one increases the associated hadron momentum, a feature which is not observed in the experimental data.

As with Cerenkov induced radiation, Mach cone induced, or conical, flow can be given a simple intuitive picture. Recall the Doppler effect, which describes the fact that when an object moving through some fluid emits sound, an observer at rest in the fluid detects the sound at a modified frequency (see the left side of Figure 2.1). If the speed of the source surpasses the speed of sound in the medium, the wavefronts which normally would be propagating ahead of the source can no longer keep up with it. Instead, they join together to form an intense pressure front (see the right side of Figure 2.1) which forms the boundary of a Mach cone. The fast partons created in the early stages of a relativistic heavy-ion collision propagate with velocity approaching the speed of light, and as has been seen in Chapter 1, the speed of sound in the QGP ranges from about 1/2 to 1/3 the speed of light, depending on temperature, so it is quite natural to think that fast partons may induce conical flow, generated by pressure gradients in the cone, in the medium.

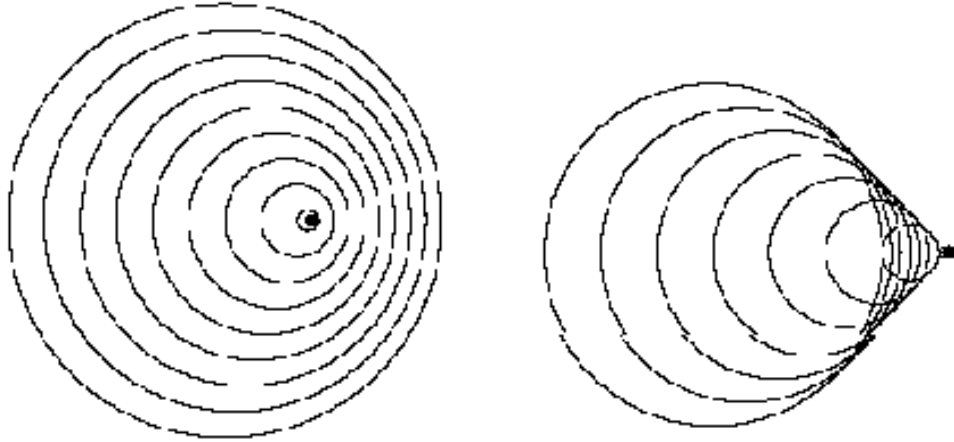


FIGURE 2.1: If the speed of a source of sound surpasses the speed of sound in the medium, the wavefronts which normally would be propagating ahead of the source can no longer keep up with it. Instead, they join together to form an intense pressure front which forms the boundary of a Mach cone [31].

Indeed, there are now several studies [32, 33, 34, 35, 36, 37, 38, 39, 40, 41, 42, 43, 44, 45] which address the issue of fast parton induced conical flow in the QGP and what consequences it may have for experimental observables, in particular, the hadron azimuthal correlations. There are many challenges to investigating conical flow induced by fast partons, two of which are the background flow profile of the underlying medium and the issue of hadronization. More will be said about these complications in later chapters. Because of these different challenges, there has yet to be a rigorous theoretical calculation which can equate the away side hadron correlation measurements with conical flow induced by fast partons. However, of the plausible mechanisms proposed so far, this seems to be the most likely candidate able to describe the data. There are two primary reasons to believe this. First, the three-hadron correlation measurements indicate the away side structure is indeed the result of a conical emission pattern. Second, the angle of the peaks in the away side distribution is independent of momentum. Both of these observations are consistent

with a Mach-cone like emission pattern, which is both conical and has an opening angle independent of momentum. The opening angle of a Mach cone in the QGP is sensitive primarily to the ratio of the speed of the fast parton to the speed of sound in the medium, and perhaps the geometry of the expanding medium, but not to a particular momentum.

2.2 Investigating Induced Flow in the QGP

In the following chapter, I begin the technical aspects of this thesis. As stated in the abstract, the primary goal will be to investigate how the QGP responds to fast partons, or hard probes. In particular, in light of the discussion above, the emphasis will be on investigating the medium response in terms of a fluid description. Before beginning any calculations, however, it will be useful to give an overview of what techniques will be employed and why.

A rigorous theoretical investigation into the response of the QGP to fast partons is met with many challenges. Perhaps the primary difficulty is bridging the high p_T physics of jet quenching with the low p_T physics of collective flow. While high p_T processes (i.e., $p_T \gtrsim 6$ GeV) can be treated with perturbative QCD, low p_T processes (i.e., $p_T \lesssim 2$ GeV) are best treated with an effective fluid description such as hydrodynamics. It's not clear that either approach is appropriate in the region of intermediate p_T . From these considerations, it seems that a consistent investigation from first principles may be an unrealistic goal.

Rather, one must develop a model which hopefully captures much of the relevant physics. One such approach is to treat the fast parton as a source of energy and momentum coupled to the hydrodynamic equations of the medium. It was shown in the previous chapter that nearly ideal hydrodynamics has been successful in describing the bulk matter produced at RHIC, thus one anticipates that hydrodynamics is well suited to describe the large distance (small momentum) medium response. In this

approach, the high p_T physics is bridged directly with the low p_T physics, and one hopes the intermediate p_T regime gets a reasonable description. In such a scenario, the source term generated by the fast parton must be specified. Much of the work presented in the rest of this thesis is devoted to calculating the hydrodynamic source term generated by a fast parton in the QGP, and then solving the medium evolution equations coupled to it.

The next three chapters, 3, 4 and 5, are devoted to calculating the source of energy and momentum generated by a fast parton in the QGP. In Chapter 3 the approach is to use kinetic theory by treating the fast parton as the source of an external color field interacting with the medium through a Vlasov equation. This approach allows one to use the classical field equations for color charges in the presence of an external field. The primary restriction on this approach is that the medium must be describable by on-shell distribution functions. Also, the Vlasov equation does not allow for collisions between particles in the medium. This means that the external field must be strong enough to change the momentum of medium particles on distance scales shorter than the mean free path. Additionally, the fast parton is assumed to follow a constant trajectory, in other words, the affect of the medium on the fast parton is neglected. As far as this author is aware, the source term derived in Chapter 3 of this thesis is the first hydrodynamic source term calculated for a QCD plasma from first principles.

In Chapter 4, the approach is quite different than that adopted in Chapter 3. There, I will be concerned with incorporating radiative energy lost by the fast parton into the hydrodynamic source of energy and momentum, something which is not included in the calculation of Chapter 3. To do this, the fast parton is treated as a point source of energy and momentum deposition, and the source term becomes a delta function centered at the position of the fast parton, whose coefficient is given by the rate of energy absorbed by the medium. As discussed above, hydrodynamics

is valid at large distance scales, so ignoring the spatial structure and focusing on the magnitude of the source should be a reasonable first approximation which will allow radiative energy loss to be incorporated.

In Chapter 5, a formalism is introduced which allows one to calculate the source of energy and momentum by coupling a source current to the Lagrangian using finite temperature field theory. This approach goes beyond the kinetic theory formalism of Chapter 3 by allowing one to incorporate off-shell contributions to the source. As a first step, a scalar field with quartic interaction coupled to a source current will be examined. The result obtained using finite temperature field theory is then compared to the kinetic theory formalism of Chapter 3. Afterward, the connection to QCD will be discussed.

In Chapter 6 the connection to the bulk fluid dynamics is made by coupling the QCD based source terms of Chapters 3 and 5 to a linearized hydrodynamic evolution. The medium response is analyzed for different viscosities, speeds of sound, and relevance of finite spatial structure of the source.

Before moving on, I note that much recent work in the field of QGP physics has been focused on examining the strongly coupled $\mathcal{N} = 4$ supersymmetric Yang-Mills plasma. Such efforts are motivated by the idea that the system is a useful model of a real QCD plasma. Studies [46, 47] of a supersonic color charge passing through this system have been performed, and it is possible to obtain solutions for the medium response at all momentum scales. However, such a calculation has never been performed for a QCD plasma for the reasons mentioned above. More will be said about the calculation from the strongly coupled $\mathcal{N} = 4$ supersymmetric Yang-Mills plasma in Chapter 7.

Hydrodynamic Source Term from Kinetic Theory

As¹ has been discussed in the previous two chapters, fast partons (partons with velocity approaching the speed of light) created by hard transverse scattering in the early moments of a heavy-ion collision are a useful probe in understanding QGP physics. Of particular importance is the process of jet quenching, in which fast partons lose energy and momentum by interacting with the surrounding medium (see, for instance, [48, 49, 50, 51, 52, 53, 54, 55]). Experimental evidence indicates that fast partons lose a significant amount of energy and momentum as they propagate through the medium. Additionally, hadron correlation functions suggest the away side distribution may be dominated by the medium's response to the fast parton. In particular, 2 and 3 hadron correlations show a structure consistent with a conical, Mach-cone like, emission pattern.

These observations have generated interest in understanding the response of the QGP to fast partons. There is strong evidence that the matter produced at RHIC obeys the hydrodynamic assumption of local thermal equilibrium. For this reason,

¹ Much of the work in this chapter originally appeared in a journal article I authored: R. B. Neufeld, *Fast Partons as a Source of Energy and Momentum in a Perturbative Quark-Gluon Plasma*, Phys. Rev. D **78**, 085015 (2008) [43]

the common theoretical approach to examining the QGP's response to a fast parton has been to treat the parton as a source of energy and momentum coupled to the hydrodynamic equations of the medium. This makes sense provided the medium maintains local thermal equilibrium following the passage of a fast parton. Assuming the medium does respond hydrodynamically to a fast parton the question arises as to what is the distribution of energy and momentum deposited? It has been observed [32, 38, 39] that the medium's response to fast partons is sensitive to the specific form of energy and momentum deposition, creating the need for a hydrodynamic source term derived from first principles. For example, the hydrodynamic source vector, which gives the momentum density deposited by the fast parton per unit time, of a parton moving at constant velocity, \mathbf{u} , can be written in Fourier space as [47]

$$\mathbf{J}(\omega, \mathbf{q}) = [\mathbf{u} \phi_u(\omega, q^2) + i\mathbf{q} \phi_q(\omega, q^2)] 2\pi\delta(\omega - \mathbf{u} \cdot \mathbf{q}). \quad (3.1)$$

The medium's response then is encoded in the functions ϕ_u and ϕ_q . For instance, if one sets $\phi_u = 0$ then the source fails to excite diffusive momentum density in the medium. The full momentum dependence of the source is necessary to predict the spectrum and shape of the sound wave excited in the medium. The sensitivity of the medium's response to the specific form of energy and momentum deposition creates the need for a hydrodynamic source term derived from first principles.

The careful reader may be curious why equation (3.1) does not contain a term proportional to $\mathbf{q} \times \mathbf{u}$. This is because $\mathbf{q} \times \mathbf{u}$ is a pseudo-vector under spatial inversion, whereas \mathbf{J} must transform as a vector (since it's a measure of momentum). One can also consider the time component of the hydrodynamic source term, J^0 , which gives the energy density deposited by the fast parton per unit time. This can be written as

$$J^0(\omega, \mathbf{q}) = \phi_E(\omega, q^2) 2\pi\delta(\omega - \mathbf{u} \cdot \mathbf{q}). \quad (3.2)$$

It is instructive to here consider the mechanism of energy and momentum deposi-

tion and the different scales involved. In a QCD plasma fast partons interact with the medium at a distance scale of the order of the inverse Debye mass, $(m_D)^{-1}$. This interaction creates a disturbance which in turn interacts with the surrounding medium, creating a new disturbance at some larger distance scale. The new disturbance again interacts with the surrounding medium, and eventually the initial disturbance propagates out to some arbitrarily large distance scale. At distances much greater than the mean free path of particles in the medium, Λ_f , the medium's response to the initial disturbance can be accurately described by hydrodynamics. Thus an effective QCD hydrodynamic source term should include the medium's response up to distances of order Λ_f , at which point the system evolves hydrodynamically. Whether the plasma is weakly or strongly coupled, the initial energy and momentum deposition occurs at a distance scale of the order of the inverse Debye mass, although the specific value of the Debye mass depends on the strength of the coupling. However, in a strongly coupled plasma, the concept of a mean free path loses meaning, and instead the de Broglie wavelength sets the minimum scale at which the hydrodynamical description is valid. In general, the application of hydrodynamics is valid on shorter distance scales for more strongly coupled mediums.

In this chapter, I will derive the hydrodynamic source term expected from a fast parton moving through a QGP in the context of kinetic theory by including the medium response at a distance scale of the order $(gT)^{-1}$. The approach will be to treat the fast parton as the source of an external color field interacting with a perturbative QGP through the collisionless Boltzmann equation. After obtaining the microscopic equation of motion, I find the macroscopic evolution by taking moments via the Chapman-Enskog approach and making the assumption of local thermal equilibrium. It is found that the fast parton serves as a source distribution of energy and momentum for the hydrodynamic equations of the medium. I then perform an explicit evaluation of the distribution both with and without the inclusion of the

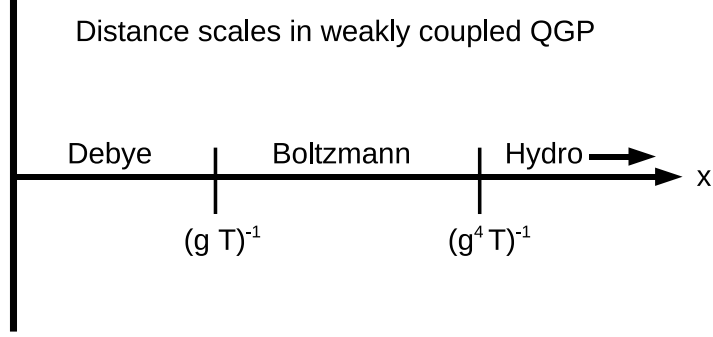


FIGURE 3.1: Some of the distance scales relevant to the hydrodynamic response of a weakly coupled QGP to fast partons.

medium’s response to screen the fast parton’s color field and interpret the results.

In a weakly coupled QCD plasma at high temperature, T , the inverse Debye mass is of order $(gT)^{-1}$, where g is the strong coupling, while the transport mean free path is of order $(g^4T)^{-1}$ [56]. The medium’s response to disturbances at distance scales between $(gT)^{-1}$ and $(g^4T)^{-1}$ is accurately described by the Boltzmann equation (see Figure 3.1). The hydrodynamic source term derived below includes the medium’s response at a distance scale of the order of the inverse Debye mass, at which point the medium’s hydrodynamic response is invoked. This is a simplification of the true QCD evolution, where the medium’s evolution between $(gT)^{-1}$ and $(g^4T)^{-1}$ should be described by the Boltzmann equation, after which the hydrodynamic response can be invoked. However, in the QGP produced at RHIC, it is likely that the mean free path is comparable in size to the inverse Debye mass (compare, for instance, [57] and [58]). Thus, from a phenomenological point of view, physics at a distance scale of the order $(gT)^{-1}$ may be relevant to the specific structure of the medium’s hydrodynamic response to fast partons. However, this also suggests the QGP produced at RHIC may be strongly coupled, limiting the application of perturbation theory.

3.1 Hydrodynamic Source Term

In this section, I will employ a formalism of kinetic theory for non-abelian plasmas originally established in [59, 60]. What is novel about the work in this section and those to follow is the application to a fast parton propagating through the medium, which is specified by the choice of the external fields given by equations (3.18,3.19,3.20).

Consider a system of partons in the presence of an external color field A_μ^a and described by the distribution $f(\mathbf{x}, \mathbf{p}, t, Q)$ which includes the color sector through its Q dependence. The Boltzmann equation for this distribution is given by [59]

$$\left(\frac{\partial}{\partial t} + \frac{\mathbf{p}}{E} \cdot \nabla_x + \frac{d\mathbf{p}}{dt} \cdot \nabla_p + \frac{\partial Q^a}{\partial t} \frac{\partial}{\partial Q^a} \right) f(\mathbf{x}, \mathbf{p}, t, Q) = 0 \quad (3.3)$$

where the collision term is omitted. The chromodynamic equations of motion for a parton with charge $gQ^a(t)$ in a color field A_μ^a are given by [61]

$$\frac{d\mathbf{p}}{dt} = gQ^a(t) (\mathbf{E}^a + (\mathbf{v} \times \mathbf{B})^a) \quad (3.4)$$

and

$$\frac{dQ^a(t)}{dt} = -gf_{abc}A_\mu^b v^\mu Q^c(t) \quad (3.5)$$

where $v_\mu = dx_\mu/dt$, f_{abc} are the $SU(3)$ structure numbers, and

$$\mathbf{E}^a + (\mathbf{v} \times \mathbf{B})^a \equiv \mathbf{F}^a \quad (3.6)$$

is the color Lorentz force. Inserting (3.4) and (3.5) into (3.3) yields

$$\left(v^\mu \frac{\partial}{\partial x^\mu} + gQ^a(t) \mathbf{F}^a \cdot \nabla_p - gf_{abc}A_\mu^b v^\mu Q^c(t) \frac{\partial}{\partial Q^a} \right) f(\mathbf{x}, \mathbf{p}, t, Q) = 0. \quad (3.7)$$

The singlet and octet components of the parton distribution, $f(\mathbf{x}, \mathbf{p}, t)$ and $f^a(\mathbf{x}, \mathbf{p}, t)$, are obtained by taking the moments of $f(\mathbf{x}, \mathbf{p}, t, Q)$ in the color sector:

$$f(\mathbf{x}, \mathbf{p}, t) = \int dQ f(\mathbf{x}, \mathbf{p}, t, Q) \equiv f_0 \quad (3.8)$$

and

$$f^a(\mathbf{x}, \mathbf{p}, t) = \int dQ Q^a f(\mathbf{x}, \mathbf{p}, t, Q) \equiv f_1^a. \quad (3.9)$$

The notation f_1^a used in (3.9) is meant to emphasize that any contribution from the color octet distribution must come from off equilibrium effects since it vanishes in equilibrium. Assuming gA_μ^a can be treated as a perturbation in an otherwise equilibrated system the contribution from f_1^a should be small and higher moments, such as f_2^{ab} ($a \neq b$), which are of higher order in gA_μ^a , will be ignored. Applying the first two moments to (3.7) gives

$$v^\mu \frac{\partial f_0}{\partial x^\mu} + g\mathbf{F}^a \cdot \nabla_p f_1^a = 0 \quad (3.10)$$

and

$$v^\mu D_\mu f_1^a = -\frac{gC_2}{N_c^2 - 1} \mathbf{F}^a \cdot \nabla_p f_0 \quad (3.11)$$

where $D_\mu f_1^a = \partial_\mu f_1^a + gf_{abc}A_\mu^b f_1^c$ is the covariant derivative. In obtaining (3.11) I have used

$$\int dQ Q^a Q^b f(\mathbf{x}, \mathbf{p}, t, Q) = \frac{C_2 \delta^{ab}}{N_c^2 - 1} f_0 + f_2^{ab} \quad (3.12)$$

where C_2 is the eigenvalue of the Casimir operator of the medium partons and, as mentioned above, f_2^{ab} is neglected.

An equation for f_0 can be obtained by solving (3.11) for f_1^a and inserting the result into (3.10). Neglecting any space-time dependence in f_0 the solution is given by

$$f_1^a = -\frac{igC_2}{N_c^2 - 1} \int \frac{d^4 k}{(2\pi)^4} \int d^4 x' U_{ab}(x, x') \frac{e^{ik \cdot (x' - x)}}{v \cdot k + i\epsilon} \mathbf{F}^b(x') \cdot \nabla_p f_0 \quad (3.13)$$

where

$$U_{ab}(x, x') = P \exp \left(- \int_{x'}^x g f_{acb} A_\mu^c dx^\mu \right) \quad (3.14)$$

is the path ordered gauge connection. The result (3.13) can be simplified with a contour integration in k^0 . It has one pole which is in the lower complex plane (i.e., $t' < t$). I find

$$\begin{aligned} f_1^a &= -\frac{gC_2}{N_c^2 - 1} \int \frac{d^3\mathbf{k}}{(2\pi)^3} \int d^4x' U_{ab}(x, x') e^{i\mathbf{v}\cdot\mathbf{k}(t'-t) - i\mathbf{k}\cdot(\mathbf{x}'-\mathbf{x})} \mathbf{F}^b(x') \cdot \nabla_p f_0 \\ &= -\frac{gC_2}{N_c^2 - 1} \int_{-\infty}^t dt' U_{ab}(x, x') \mathbf{F}^b(x') \cdot \nabla_p f_0. \end{aligned} \quad (3.15)$$

where now $\mathbf{x}' = \mathbf{x}(t') = \mathbf{v}(t' - t) + \mathbf{x}$. Combining (3.15) with (3.10) gives the result for f_0 [60]

$$v^\mu \frac{\partial f_0}{\partial x^\mu} - \nabla_{p_i} D_{ij} \nabla_{p_j} f_0 = 0 \quad (3.16)$$

where

$$D_{ij} = \frac{g^2 C_2}{N_c^2 - 1} \int_{-\infty}^t dt' F_i^a(x) U_{ab}(x, x') F_j^b(x'). \quad (3.17)$$

The result (3.16) describes the phase space distribution of partons in the presence of a soft external color field A_μ^a (the term *soft* implies the momenta in A_μ^a are small compared to the average momentum in f_0). My approach is to consider the external color field to be generated by a fast parton propagating through the medium, which I specify to be a perturbative QGP. In light of the perturbative nature of the medium it makes sense to expand the path ordered gauge connection in (3.17) to zeroth order in g . In the hard thermal loop (HTL) approximation the source field for a fast parton with constant velocity \mathbf{u} at position $\mathbf{x} = \mathbf{u}t$ has the Fourier representation

$$\mathbf{E}_T^a(x) = \frac{igQ_p^a}{(2\pi)^3} \int d^4k e^{-ik\cdot x} \frac{(\mathbf{u}k^2 - \mathbf{k}(\mathbf{k}\cdot\mathbf{u}))\omega\delta(\omega - \mathbf{u}\cdot\mathbf{k})}{k^2(k^2 - \epsilon_T(\mathbf{k}, \omega)\omega^2)} \quad (3.18)$$

$$\mathbf{E}_L^a(x) = -\frac{igQ_p^a}{(2\pi)^3} \int d^4k e^{-ik\cdot x} \frac{(\mathbf{k}\cdot\mathbf{u})\delta(\omega - \mathbf{u}\cdot\mathbf{k})}{\epsilon_L(\mathbf{k}, \omega)\omega k^2} \mathbf{k} \quad (3.19)$$

$$\mathbf{B}^a(x) = \frac{igQ_p^a}{(2\pi)^3} \int d^4k e^{-ik\cdot x} \frac{(\mathbf{k}\times\mathbf{u})\delta(\omega - \mathbf{u}\cdot\mathbf{k})}{k^2 - \epsilon_T(\mathbf{k}, \omega)\omega^2} \quad (3.20)$$

where $k^\mu = (\omega, \mathbf{k})$, and the dielectric functions, $\epsilon_L(\mathbf{k}, \omega)$ and $\epsilon_T(\mathbf{k}, \omega)$, encode the medium's response to screen the fields. These functions read explicitly [35]

$$\begin{aligned}\epsilon_L &= 1 + \frac{2m_g^2}{k^2} \left[1 - \frac{\omega}{2k} \left(\ln \left[\frac{k + \omega}{k - \omega} \right] - i\pi\Theta(k^2 - \omega^2) \right) \right], \\ \epsilon_T &= 1 - \frac{m_g^2}{\omega^2} \left[\frac{\omega^2}{k^2} + \frac{\omega}{2k} \frac{(k^2 - \omega^2)}{k^2} \left(\ln \left[\frac{k + \omega}{k - \omega} \right] - i\pi\Theta(k^2 - \omega^2) \right) \right]\end{aligned}\tag{3.21}$$

where $m_g = m_D/\sqrt{3}$ and $\Theta(k^2 - \omega^2)$ is a step function which is unity if $k^2 > \omega^2$ and zero otherwise. The derivation and momentum space representation of Eqs. (3.18 - 3.20) is given in Appendix A. Note that in (3.18) and (3.19) the electric field has been divided into transverse and longitudinal parts such that $\mathbf{E} = \mathbf{E}_T + \mathbf{E}_L$.

The macroscopic equations of motion are found by taking moments of the evolution equation (3.16):

$$\int \frac{d\mathbf{p} p^\nu}{(2\pi)^3} \left(v^\mu \frac{\partial f_0}{\partial x^\mu} - \nabla_{p_i} D_{ij} \nabla_{p_j} f_0 \right) = 0\tag{3.22}$$

where $p^\nu = (E, \mathbf{p})$. The integrals in (3.22) can be evaluated by boosting to the frame co-moving with the volume element and then exploiting the hydrodynamic assumption of local thermal equilibrium by using the thermodynamic relations (which are only valid in the local frame of the medium element)

$$\int \frac{d\mathbf{p} p^\mu p^\nu}{(2\pi)^3} \frac{p^\mu p^\nu}{p^0} f_0 = (\epsilon + p)\delta^{0\mu}\delta^{0\nu} - pg^{\mu\nu}\tag{3.23}$$

where p is the local pressure, ϵ is the local energy density and $g^{\mu\nu}$ is the metric tensor. Using the notation

$$\int \frac{d\mathbf{p} p^\nu}{(2\pi)^3} (\nabla_{p_i} D_{ij} \nabla_{p_j} f) \equiv J^\nu\tag{3.24}$$

I find that the resulting equations of motion for the medium evolution are

$$\partial_\mu T^{\mu\nu} = J^\nu\tag{3.25}$$

where the energy-momentum tensor is given by

$$T^{\mu\nu} = (\epsilon + p)w^\mu w^\nu - pg^{\mu\nu} \quad (3.26)$$

and w^μ is the medium 4-velocity. The details of how Eq. (3.25) is derived are shown in Appendix B.

The result (3.25) describes the macroscopic evolution of a perturbative QGP in the presence of J^ν , which acts as a source of energy and momentum. In other words, J^ν gives the distribution of energy and momentum deposited into a perturbative QGP due to the passage of a fast parton. This is precisely the quantity I set out to evaluate. In the derivation of (3.25) effects of viscosity in the medium have been neglected, as can be seen from the ideal form of the energy-momentum tensor given in equation (3.26). This is because off-equilibrium effects in the medium response have been neglected. These effects could be incorporated by keeping the collision term in the Boltzmann equation (3.3). In Chapter 6, where the linearized hydrodynamic equations coupled to a source term are solved, the viscosity is included as a parameter of the equations of motion. In the remainder of this chapter, I will evaluate the source term (3.24) both with and without dielectric screening and examine the resulting distribution.

3.1.1 A Comment on the Dielectric Screening

Medium screening of the color fields generated by the fast parton was implemented using the dielectric functions (3.21). In light of the perturbative assumptions used in deriving (3.16), one may ask whether it makes sense to include screening effects to all orders in g , as is done in the fields listed above. The dielectric functions used in (3.21) are derived in the HTL formalism, and are known to be gauge invariant [62], so in terms of gauge invariance it does make sense. Additionally, the dielectric screening cures an infrared divergence in the source which manifests itself when calculating

the total energy deposited in the medium (see (3.59) below) or in taking the Fourier transform of the source. This negates the need to introduce an infrared cutoff by hand, which is necessary in the absence of screening.

3.2 Explicit Evaluation of the Source Term

I begin by simplifying (3.24) with an integration by parts

$$\int \frac{d\mathbf{p} p^\nu}{(2\pi)^3} (\nabla_{p_i} D_{ij} \nabla_{p_j} f_0) = - \int \frac{d\mathbf{p}}{(2\pi)^3} (\delta_{0\nu} \frac{p_i}{p_0} + \delta_{i\nu}) D_{ij} \nabla_{p_j} f_0 \quad (3.27)$$

where $\delta_{0\nu}$ is the Kronecker-Delta symbol and, as mentioned previously, i, j range from 1 to 3. I specify the medium to be a locally thermal plasma of massless gluons with the distribution

$$f_0(p) = \frac{2(N_c^2 - 1)}{e^{\beta p^0} - 1} \quad (3.28)$$

where N_c is the number of colors and $1/\beta = T$ is the local temperature of the medium. With this specification the distribution, f_0 , now contains the only dependence upon the magnitude of the momentum, $p^0 = p$, in (3.27). It follows that

$$- \int \frac{d\mathbf{p}}{(2\pi)^3} (\delta_{0\nu} \frac{p_i}{p_0} + \delta_{i\nu}) D_{ij} \nabla_{p_j} f_0 = \frac{(N_c^2 - 1)T^2}{3} \int \frac{d\hat{\mathbf{v}} \hat{v}_j}{4\pi} (\delta_{0\nu} \hat{v}_i + \delta_{i\nu}) D_{ij} \quad (3.29)$$

where $\hat{\mathbf{v}} = \mathbf{p}/p^0$ is the directional velocity of medium particles.

Inserting the explicit form of D_{ij} gives

$$J^\nu(x) = \frac{m_D^2}{(2\pi)^8} \int_{-\infty}^t dt' \int d^4k d^4k' d\hat{\mathbf{v}} \frac{\hat{v}_j}{4\pi} e^{-ik \cdot x - ik' \cdot x'} (\delta_{0\nu} \hat{v}_i + \delta_{i\nu}) F_i^a(k) F_j^a(k') \quad (3.30)$$

where $m_D = \sqrt{N_c/3} gT$ is equal to the Debye mass for gluons in the HTL approximation, and I have introduced the Fourier representation of the color Lorentz force

$$F_i^a(x) = \frac{1}{(2\pi)^4} \int d^4k e^{-ik \cdot x} F_i^a(k). \quad (3.31)$$

The generalization to include N_f flavors of quarks/antiquarks in the medium can be done in a straightforward way by adding the appropriate thermal distribution to (3.28)

$$f_0 = \frac{2(N_c^2 - 1)}{e^{\beta p^0} - 1} + \frac{4N_c N_f}{e^{\beta p^0} + 1} \quad (3.32)$$

and repeating the steps which lead to (3.30). The only modification is that the expression for the Debye mass appearing in (3.30) now includes flavor: $m_D = \sqrt{(2N_c + N_f)/6} gT$. In the numerical results that follow I have set $N_f = 0$.

I next make the assumption that the typical momentum transfer between the source particle and the medium is small compared to the typical momentum of a medium particle. This assumption allows a straight line approximation relating the position of a medium particle at time t' to its position at time t :

$$\mathbf{x}' = \mathbf{x} + \hat{\mathbf{v}}(t' - t). \quad (3.33)$$

The t' integration can be evaluated after plugging (3.33) into (3.30) and introducing an exponential damping factor, $i\epsilon$, yielding

$$J^\nu(x) = \frac{im_D^2}{(2\pi)^8} \int d^4k d^4k' d\hat{\mathbf{v}} e^{i(\mathbf{k}+\mathbf{k}')\cdot\mathbf{x}-it(\omega+\omega')} \times \frac{\hat{\mathbf{v}} \cdot \mathbf{E}^a(k') (\delta_{0\nu} \hat{\mathbf{v}} \cdot \mathbf{E}^a(k) + \delta_{i\nu} (E_i^a(k) + (\hat{\mathbf{v}} \times \mathbf{B})_i^a(k)))}{4\pi(\omega' - \mathbf{k}' \cdot \hat{\mathbf{v}} + i\epsilon)}. \quad (3.34)$$

Next consider the integral over $\hat{\mathbf{v}}$. It can be evaluated by choosing a frame in which $\mathbf{k}' = k'\hat{\mathbf{z}}$, performing the integral, and then rotating back into a frame in which \mathbf{k}' is arbitrary. The explicit details of the calculation are given in Appendix C. The result is most easily expressed by dividing the source term into two pieces, J_1^ν and J_2^ν , where $J_1^\nu + J_2^\nu = J^\nu$. After integrating out the delta functions in (3.18 - 3.20) I find

$$J_1^\nu(x) = \frac{im_D^2}{(2\pi)^8} \int d^3k d^3k' e^{i(\mathbf{k}+\mathbf{k}')\cdot(\mathbf{x}-\mathbf{u}t)} \Omega_2(\mathbf{k}') (\delta_{0\nu} \mathbf{E}^a(\mathbf{k}') \cdot \mathbf{E}^a(\mathbf{k}) + \delta_{i\nu} (\mathbf{E}^a(\mathbf{k}') \times \mathbf{B}^a(\mathbf{k}))_i) \quad (3.35)$$

and

$$\begin{aligned}
J_2^\nu(x) &= \frac{im_D^2}{(2\pi)^8} \int d^3k d^3k' e^{i(\mathbf{k}+\mathbf{k}')\cdot(\mathbf{x}-\mathbf{u}t)} (\mathbf{E}^a(\mathbf{k}') \cdot \hat{\mathbf{k}}') \\
&\times \left(\left(\Omega_1(\mathbf{k}') \mathbf{u} \cdot \hat{\mathbf{k}}' - \Omega_2(\mathbf{k}') \right) \left(\delta_{0\nu} (\mathbf{E}^a(\mathbf{k}) \cdot \mathbf{k}') + \delta_{i\nu} (\hat{\mathbf{k}}' \times \mathbf{B}^a(\mathbf{k}))_i \right) + \delta_{i\nu} \Omega_1(\mathbf{k}') E_i^a(\mathbf{k}) \right)
\end{aligned} \tag{3.36}$$

where

$$\Omega_1(\mathbf{k}') = \frac{\mathbf{u} \cdot \mathbf{k}'}{2k'^2} \ln \left[\frac{k' + \mathbf{u} \cdot \mathbf{k}'}{k' - \mathbf{u} \cdot \mathbf{k}'} \right] - \frac{i\pi \mathbf{u} \cdot \mathbf{k}'}{2k'^2} - \frac{1}{k'} \tag{3.37}$$

$$\begin{aligned}
\Omega_2(\mathbf{k}') &= \frac{1}{4k'^3} \left(\ln \left[\frac{k' + \mathbf{u} \cdot \mathbf{k}'}{k' - \mathbf{u} \cdot \mathbf{k}'} \right] (k'^2 - (\mathbf{u} \cdot \mathbf{k}')^2) \right. \\
&\quad \left. - \pi i (k'^2 - (\mathbf{u} \cdot \mathbf{k}')^2) + 2k' \mathbf{u} \cdot \mathbf{k}' \right).
\end{aligned} \tag{3.38}$$

In the above expressions $\hat{\mathbf{k}}'$ is the unit vector in the \mathbf{k}' direction, k' is the magnitude of \mathbf{k}' , \mathbf{u} is the source parton's velocity. The exponential damping factor in (3.34), $i\epsilon$, sets the sign of the imaginary terms in (3.37), (3.38).

At this point it is convenient to specify a direction for the source particle's velocity which I do by choosing $\mathbf{u} = u \hat{\mathbf{z}}$. I also choose to work in plane polar coordinates, k_T and ϕ , such that $k_x = k_T \cos \phi$ and $k_y = k_T \sin \phi$. With these choices the only dependence upon the momentum space variable ϕ is in the exponential and terms proportional to $\cos \phi$ or $\sin \phi$. The exponential depends upon ϕ through the term $ik_T(x \cos \phi + y \sin \phi)$ which can be rewritten as $ik_T \rho \cos[\phi - \alpha]$, where $x = \rho \cos \alpha$ and $y = \rho \sin \alpha$. With these simplifications the entire ϕ dependence of (3.35) and (3.36) can be integrated out by using the relations

$$\int_0^{2\pi} \frac{d\phi}{2\pi} \exp [ik_T \rho \cos[\phi - \alpha]] \begin{bmatrix} 1 \\ \cos \phi \\ \sin \phi \end{bmatrix} \equiv \begin{bmatrix} J_0(\rho k_T) \\ \frac{ix}{\rho} J_1(\rho k_T) \\ \frac{iy}{\rho} J_1(\rho k_T) \end{bmatrix} \tag{3.39}$$

where $J_n(x)$ is a Bessel function of order n . The calculation is further simplified due to the fact that the \mathbf{k} and \mathbf{k}' dependence can be completely factorized, reducing the

remaining four-dimensional integration to a product of two-dimensional integrations. Using the explicit field dependence listed above, I find there are 12 unique two-dimensional integrations which must be performed. They are given by

$$\begin{aligned}
\begin{bmatrix} \xi_1 \\ \xi_2 \\ \xi_3 \\ \xi_4 \end{bmatrix} &\equiv \int dk_z dk_T \frac{e^{i(z-ut)k_z} \Omega_1(k)}{k D_L(k)} \begin{bmatrix} J_0(\rho k_T) k_T k^2 \\ J_0(\rho k_T) k_T k_z^2 \\ J_0(\rho k_T) k_T^3 \\ J_1(\rho k_T) k_z k_T^2 \end{bmatrix} \\
\begin{bmatrix} \xi_5 \\ \xi_6 \end{bmatrix} &\equiv \int dk_z dk_T \frac{e^{i(z-ut)k_z} \Omega_2(k)}{k^2 D_T(k)} \begin{bmatrix} J_0(\rho k_T) k_z k_T^3 \\ J_1(\rho k_T) k_T^2 k_z^2 \end{bmatrix} \\
\begin{bmatrix} \xi_7 \\ \xi_8 \end{bmatrix} &\equiv \int dk_z dk_T \frac{e^{i(z-ut)k_z}}{D_L(k)} \begin{bmatrix} J_1(\rho k_T) k_T^2 \\ J_0(\rho k_T) k_z k_T \end{bmatrix} \\
\begin{bmatrix} \xi_9 \\ \xi_{10} \\ \xi_{11} \\ \xi_{12} \end{bmatrix} &\equiv \int dk_z dk_T \frac{e^{i(z-ut)k_z}}{k^2 D_T(k)} \begin{bmatrix} J_1(\rho k_T) k_T^2 k^2 \\ J_1(\rho k_T) k_T^4 \\ J_1(\rho k_T) k_T^2 k_z^2 \\ J_0(\rho k_T) k_z k_T^3 \end{bmatrix}
\end{aligned} \tag{3.40}$$

where $D_L(k) \equiv k^2 \epsilon_L(k)$, $D_T(k) \equiv k^2 - u^2 k_z^2 \epsilon_T(k)$.

In terms of the above definitions the source term is

$$J^{x(y)} = \frac{g^2 m_D^2 (Q_p^a)^2}{16\pi^4} \frac{x(y)}{\rho} (u^3 \xi_5 \xi_9 + (\xi_1 \xi_7 - u^2 \xi_2 \xi_{10} + u^2 \xi_3 \xi_{11})), \tag{3.41}$$

$$J^z = \frac{ig^2 m_D^2 (Q_p^a)^2}{16\pi^4} (u^2 \xi_9 (u \xi_6 + \xi_4) - \xi_1 (\xi_8 - u^2 \xi_{12})) \tag{3.42}$$

and

$$J^0 = - \frac{ig^2 m_D^2 (Q_p^a)^2}{16\pi^4} ((\xi_8 - u^2 \xi_{12})(u \xi_2 - u^2 \xi_5) - u(u \xi_6 + \xi_4)(\xi_7 + u^2 \xi_{11})). \tag{3.43}$$

The problem is now reduced to the evaluation of the 12 ξ_i terms. Before considering the full results of such an evaluation it is useful to calculate the above expressions without including the medium's screening of the fields. I perform this calculation in the next section and obtain an analytical result.

3.3 The Unscreened Source Term

The unscreened source term is found by setting the dielectric function given in (3.21) to unity, or, equivalently, setting $D_L(k) = k^2$ and $D_T(k) = k^2 - u^2 k_z^2$ in (3.40). It is easy to verify that with this simplification (3.41) and (3.43) can be rewritten as

$$J^{x(y)} = \frac{g^2 m_D^2 (Q_p^a)^2 x(y)}{16\pi^4} \frac{1}{\rho} \xi_9 (u^3 \xi_5 + (\xi_1 - u^2 \xi_2)), \quad (3.44)$$

$$J^0 = \frac{ig^2 m_D^2 (Q_p^a)^2}{16\pi^4} \times (u \xi_9 (u \xi_6 + \xi_4) - (u \xi_2 - u^2 \xi_5) (\xi_8 - u^2 \xi_{12})) \quad (3.45)$$

A quick perusal of the source term given by (3.42,3.44,3.45) reveals that the only combinations of ξ_7, \dots, ξ_{12} that need to be evaluated are $(\xi_8 - u^2 \xi_{12})$ and ξ_9 . These relevant combinations are given by

$$\int dk_z dk_T \frac{e^{i(z-ut)k_z}}{k_z^2 + \gamma^2 k_T^2} \begin{bmatrix} \gamma^2 J_1(\rho k_T) k_T^2 \\ J_0(\rho k_T) k_z k_T \end{bmatrix} = \begin{bmatrix} \xi_9 \\ \xi_8 - u^2 \xi_{12} \end{bmatrix} \quad (3.46)$$

where $\gamma^2 = (1 - u^2)^{-1}$.

The above expressions can be evaluated in a straightforward manner by first performing a contour integration in the k_z variable. The general form needed is

$$\int dk_z \frac{e^{\pm i k_z (z-ut)}}{(k_z^2 + k_T^2 \gamma^2)} \begin{bmatrix} \gamma^2 k_T^2 \\ k_z \end{bmatrix} = \pi e^{\mp (z-ut) k_T \gamma} \begin{bmatrix} \gamma \\ \pm i \end{bmatrix} \quad (3.47)$$

where \pm refers to the sign of $(z - ut)$. Similarly, one can use the relation

$$\int dk_T k_T e^{-k_T \gamma |z-ut|} \begin{bmatrix} J_1(\rho k_T) \\ J_0(\rho k_T) \end{bmatrix} = \frac{1}{(\rho^2 + \gamma^2 (z - ut)^2)^{3/2}} \begin{bmatrix} \rho \\ \gamma |z - ut| \end{bmatrix} \quad (3.48)$$

to obtain the result

$$\begin{bmatrix} \xi_9 \\ \xi_8 - u^2 \xi_{12} \end{bmatrix} = \frac{\pi \gamma}{(\rho^2 + \gamma^2 (z - ut)^2)^{3/2}} \begin{bmatrix} \rho \\ i(z - ut) \end{bmatrix} \quad (3.49)$$

Before attempting an explicit evaluation of ξ_1, \dots, ξ_6 it is worthwhile to consider the general form of the source term given by (3.42,3.44,3.45). It is interesting to note

that (3.42) and (3.45) have a similar form. If one were to replace $\xi_1 \rightarrow (u^2\xi_2 - u^3\xi_5)$ in (3.42) then one would find the relation

$$J_z \rightarrow uJ_0. \quad (3.50)$$

I am motivated to find a relationship between ξ_1 , ξ_2 , and ξ_5 that would allow me to write the source term in a form similar to that given by (3.50). I can (trivially) write

$$\xi_1 = (u^2\xi_2 - u^3\xi_5) + (\xi_1 - u^2\xi_2) + u^3\xi_5 \quad (3.51)$$

which allows

$$\begin{aligned} J^z &= \frac{ig^2m_D^2(Q_p^a)^2}{16\pi^4} (u^2\xi_9(u\xi_6 + \xi_4) - ((u^2\xi_2 - u^3\xi_5) \\ &\quad + (\xi_1 - u^2\xi_2) + u^3\xi_5) (\xi_8 - u^2\xi_{12})) \\ &= uJ^0 + 2(z - ut) \frac{d(\rho, z, t)}{\pi} \gamma (u^3\xi_5 + (\xi_1 - u^2\xi_2)) \end{aligned} \quad (3.52)$$

and

$$J^{x(y)} = 2x(y) \frac{d(\rho, z, t)}{\pi} \gamma (u^3\xi_5 + (\xi_1 - u^2\xi_2)) \quad (3.53)$$

where the function d is given by

$$d(\rho, z, t) = \frac{\alpha_s(Q_p^a)^2 m_D^2}{8\pi(\rho^2 + \gamma^2(z - ut)^2)^{3/2}}. \quad (3.54)$$

Notice that $J^{x(y)}$ now has the same form as $J^z - uJ^0$ apart from the factors of x and $(z - ut)$. The source term can be written in the following compact form:

$$J^\nu(x) = (J^0(x), \mathbf{u}J^0(x) - \mathbf{J}_\nu) \quad (3.55)$$

where

$$\mathbf{J}_\nu = (\mathbf{x} - \mathbf{u}t) \frac{2\gamma}{\pi} d(\rho, z, t) (u^3\xi_5 + (\xi_1 - u^2\xi_2)). \quad (3.56)$$

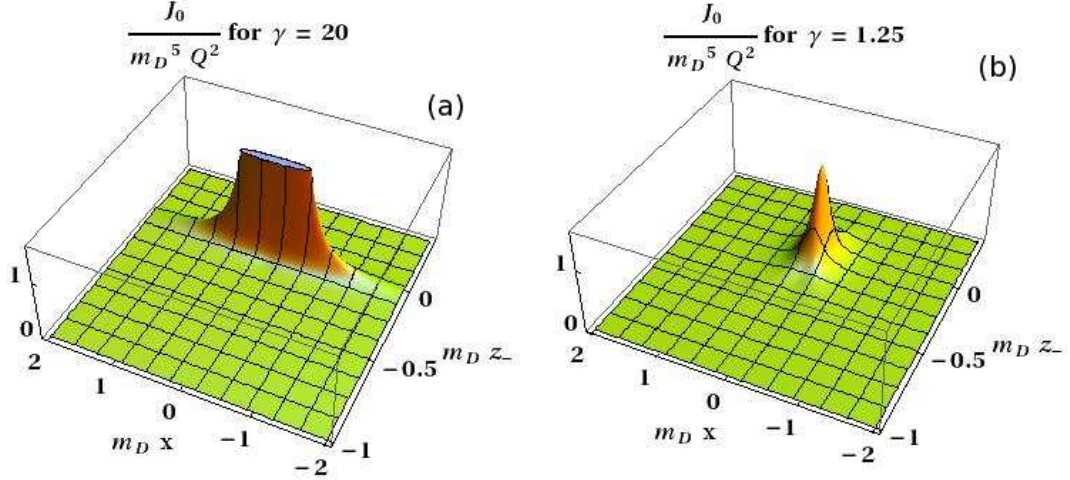


FIGURE 3.2: Three-dimensional plots of the scaled energy density deposited per unit time by a fast parton moving in the positive z direction for $\alpha_s = 1/\pi$ and $N_c = 3$ [see (3.57)]. The plots are scaled by $m_D^5 (Q_p^a)^2 \approx 20.4 \text{ GeV/fm}^4$ for a gluon moving in a QGP at $T = 200 \text{ MeV}$. As one might expect, the distribution becomes Lorentz contracted for large values of γ . (In the above plots, I have set $y = 0.4 \text{ GeV}^{-1}$ to avoid plotting the origin where the source is divergent.)

I now continue by examining the terms ξ_1, \dots, ξ_6 which are considerably more difficult to evaluate than ξ_7, \dots, ξ_{12} because of their dependence on the two Ω_i terms. The result and method of their evaluation is discussed in detail in Appendix D. Inserting the ξ_i into (3.45) and (3.56) I eventually find for the source term

$$J^0(\rho, z, t) = d(\rho, z, t) \gamma u^2 \left(1 - \frac{z_-}{(z_-^2 + \rho^2)} \left(z_- + \frac{\gamma u \rho^2}{\sqrt{\rho^2 + z_-^2 \gamma^2}} \right) \right) \quad (3.57)$$

$$\mathbf{J}_v(\rho, z, t) = (\mathbf{x} - \mathbf{u}t) \frac{\alpha_s (Q_p^a)^2 m_D^2}{8\pi (z_-^2 + \rho^2)^2} \times \left(\frac{u^4 \rho^4 + (z_-^2 \gamma^2 + \rho^2) \left(2z_- + \frac{(u^2+2)\rho^2}{\gamma^2} \right)}{(z_-^2 \gamma^2 + \rho^2)^2} - \frac{2uz_-}{\gamma \sqrt{z_-^2 \gamma^2 + \rho^2}} \right) \quad (3.58)$$

where $z_- = (z - ut)$.

Equations (3.57) and (3.58), combined with (3.55), give the distribution of energy and momentum deposited into a perturbative QGP per unit time by a parton with

constant velocity $\mathbf{u} = u \hat{\mathbf{z}}$ at position $\mathbf{x} = ut \hat{\mathbf{z}}$ in the absence of screening. That this result can be expressed in closed form is remarkable. The result for $J^0(\rho, z, t)$ is plotted in Fig. 3.2 for two different values of γ for $\alpha_s = 1/\pi$ and $N_c = 3$. The plots are scaled by $m_D^5(Q_p^a)^2 \approx 20.4 \text{ GeV}/\text{fm}^4$ for a gluon moving in a QGP at 200 MeV. As one might expect, the distribution becomes Lorentz contracted for large values of γ . In the plots, I have set $y = 0.4 \text{ GeV}^{-1}$ (about 0.08 fm) to avoid plotting the origin where the source is divergent.

The total energy deposited per unit time (or length) can be obtained by integrating (3.57) over all space:

$$-\frac{dE}{dx} = \int d\mathbf{x} J^0(\rho, z, t) = \frac{\alpha_s(Q_p^a)^2 m_D^2}{2} \ln \left[\frac{\rho_{\max}}{\rho_{\min}} \right] \left(1 - \frac{y}{\gamma^2 u} \right) \quad (3.59)$$

where $y = \cosh^{-1}(\gamma)$ is the rapidity and ρ_{\max} and ρ_{\min} are infrared and ultraviolet cut-offs for the ρ -integration. This result matches the standard leading-logarithmic result [63] for collisional energy loss in the relativistic ($u \rightarrow 1$) limit if one chooses $\rho_{\max} = 1/m_D$ and $\rho_{\min} = 1/(2\sqrt{E_p T})$, where E_p is the energy of the fast parton. The divergence which arises in (3.59) when taking $\rho_{\min} \rightarrow 0$ can physically be understood as the result of an infinite momentum transfer to the medium. The choice of $\rho_{\min}^{-1} = 2\sqrt{E_p T}$ represents the maximum momentum transfer allowed by kinematic constraints. The divergence arising from $\rho_{\max} \rightarrow \infty$ is due to the unscreened Coulomb potential generated by the fast parton, which decays like $1/\rho$. In-medium screening at the Debye scale naturally cures this divergence, which motivates the choice of $\rho_{\max} = 1/m_D$. It is interesting to plot the u dependence of (3.59) which is done in Fig. 3.3. The total momentum deposited per unit time can likewise be obtained by integrating $\mathbf{J}(\rho, z, t)$ over all space (recall that $\mathbf{J} = \mathbf{u}J^0 - \mathbf{J}_v$). One can verify explicitly that the source term satisfies the energy-momentum relation

$$\int d\mathbf{x} \mathbf{u} \cdot \mathbf{J}(\rho, z, t) = \int d\mathbf{x} J^0(\rho, z, t). \quad (3.60)$$

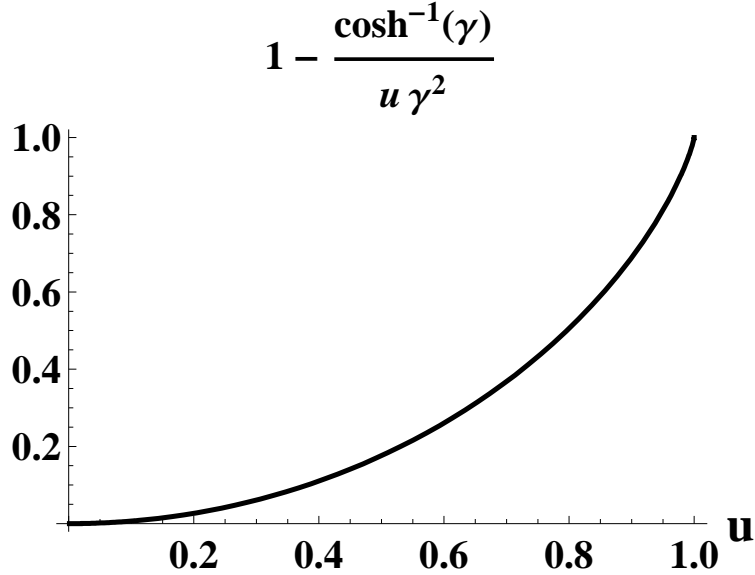


FIGURE 3.3: The dependence of $-dE/dx$, as given by (3.59), on the magnitude of the velocity of the fast parton, u , is contained in the term $(1 - \frac{\gamma}{\gamma^2 u})$ which is plotted above.

A careful observer may notice that the denominators of (3.57) and (3.58) contain terms involving both $(z_-^2 \gamma^2 + \rho^2)$, which encodes the Lorentz contraction of the fast parton's field configuration, and $(z_-^2 + \rho^2)$, which is sensitive to the rest frame of the medium. One may ask why the result, in the absence of dielectric screening, should depend on the rest frame of the medium. The answer can be traced back to the t' integration in (3.30) which records the history of the fast parton's interactions with the medium. In that expression the fast parton interacts with a medium particle at t' , which is expressed by $F_j(k')$, and again at t , which is expressed by $F_i(k)$. In between t' and t the medium particle propagates with a momentum that depends on the properties of the medium [see (3.33)]. Thus the second interaction, at t , depends on both the field configuration of the fast parton and the properties of the medium, even in the absence of screening. One can observe this effect in Fig. 3.4, where $J^0(\rho, z, t)/(\gamma u^2)$ is plotted as a function of γz_- for the parameters $m_D = 0.4$ GeV, $\alpha_s = 1/\pi$ and $\rho = 1$ GeV⁻¹. If $J^0(\rho, z, t)$ depended only on the field configuration of

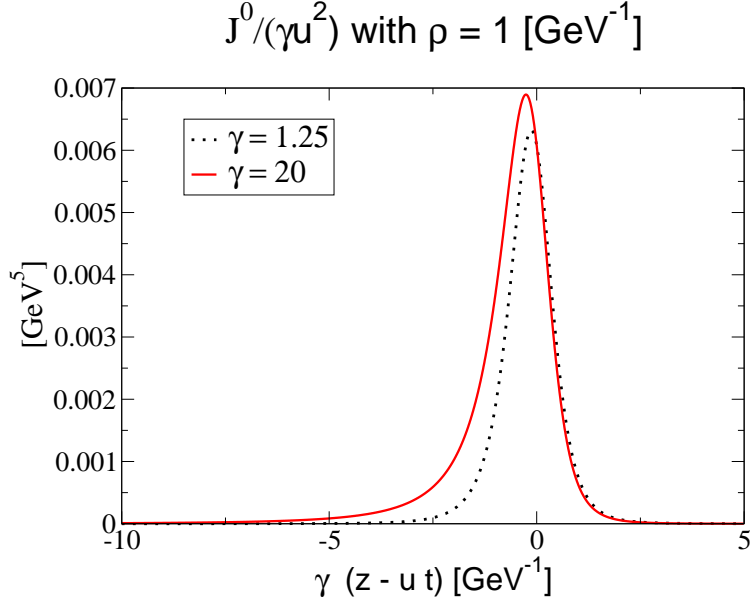


FIGURE 3.4: A plot of $J^0(\rho, z, t)/(\gamma u^2)$ as a function of $\gamma(z - ut)$ for the parameters $m_D = 0.4$ GeV, $\alpha_s = 1/\pi$ and $\rho = 1$ GeV⁻¹. If $J^0(\rho, z, t)$ depended only on the field configuration of the fast parton the curves should be identical. As one can see, there is a slight shift in the curve when going from $\gamma = 1.25$ to $\gamma = 20$. This shift reflects the dynamics of the medium in between the two interactions at t' and t (see discussion in the text). The fact that the shift in the curve is small even though γ has changed by a factor of 16 suggests the effect is small.

the fast parton the curves should be identical. As one can see, there is a slight shift in the curve when going from $\gamma = 1.25$ to $\gamma = 20$. This shift reflects the dynamics of the medium in between the two interactions at t' and t . The fact that the shift in the curve is small even though γ has changed by a factor of 16 suggests the effect is small.

For a highly relativistic source parton Eqs. (3.57) and (3.58) can be written in a simplified form by considering that terms with $(z_-^2 \gamma^2 + \rho^2)$ in the denominator will be severely damped except for $z \approx ut$. In this case, I keep $(z - ut)$ to first order (and

drop terms proportional to $1/\gamma$, etc.) and the result becomes

$$J^0(\rho, z, t) = d(\rho, z, t)\gamma u^2 \left(1 - \frac{\gamma u z_-}{\sqrt{z_-^2 \gamma^2 + \rho^2}}\right) \quad (3.61)$$

$$\mathbf{J}_v(\rho, z, t) = (\mathbf{x} - \mathbf{u}t) d(\rho, z, t) \frac{u^4}{\sqrt{z_-^2 \gamma^2 + \rho^2}} \quad (3.62)$$

In the next section, I consider the numerical evaluation of the source term with medium screening included and compare to the analytical result without screening.

3.4 Result With Screening

The evaluation of the source term (3.41,3.42,3.43) with medium screening included must be done numerically. As mentioned before this amounts to evaluating the 12 ξ_i terms listed in (3.40). A discussion of the specific techniques used to perform the numerical integrations is given in Appendix E. Also, a general discussion of the software used and control of accuracy of the numerical integration performed in this chapter and elsewhere in this thesis is given in Appendix H.

In this section all evaluations are for a parton moving along the positive z axis with velocity $u = 0.99$ and I have set $m_D = 0.4$ GeV, $N_c = 3$ and $\alpha_s = 1/\pi$ (the choice of $u = 0.99$ corresponds to $\gamma \approx 7$, or $E \approx 3$ GeV for the source gluon, which is likely too small a choice for the fast partons produced at RHIC but lends itself nicely to plotting the result). The result for the energy density deposited per unit time both with and without medium screening is given in Fig. 3.5. One sees a very similar structure in both cases except that the screened result is moderately damped in the transverse direction. A similar plot is shown in Fig. 3.6 for the transverse momentum density deposited per unit time. Here one finds more noticeable differences in the two cases. For instance, the screened result has a positive bump just behind the source parton which is absent in the unscreened result. This would correspond to matter

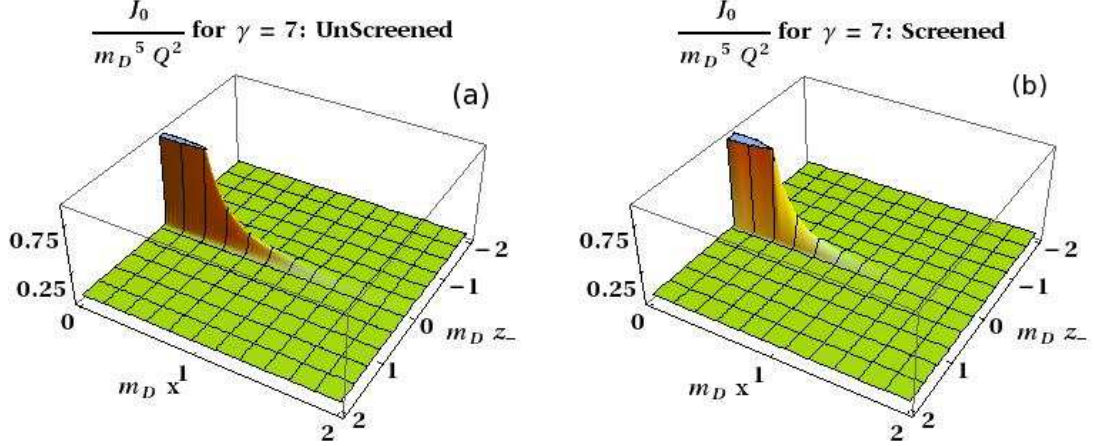


FIGURE 3.5: Plots of the scaled energy density deposited per unit time by a parton moving in the positive z direction with velocity $u = 0.99$ and $\alpha_s = 1/\pi$, both with and without medium screening (compare with Fig. 3.2). There is a very similar structure in both cases; however, as one would expect, the screened result shows some damping in the transverse direction.

being pushed outward, away from the source parton, in the vicinity of the bump. The differences are further highlighted in Fig. 3.7. Plots of the parallel momentum density distribution, J^z , are not included because they are very similar to J^0 for a relativistic source.

3.5 Discussion

In this chapter, I have derived the space-time distribution of energy and momentum deposited by a fast parton traversing a perturbative quark-gluon plasma by including physics at the Debye screening scale. The approach has been to treat the fast parton as the source of an external color field perturbing the medium. The final result depends on two parameters: the source strength $\alpha_s Q_p^2$ and the Debye mass $m_D = \sqrt{N_c/3} gT$.

Several assumptions were made in deriving the result. The first, and primary, of these is that the medium is perturbative in the coupling α_s . This assumption is reflected in the derivation of (3.16), the expansion of the path ordered gauge

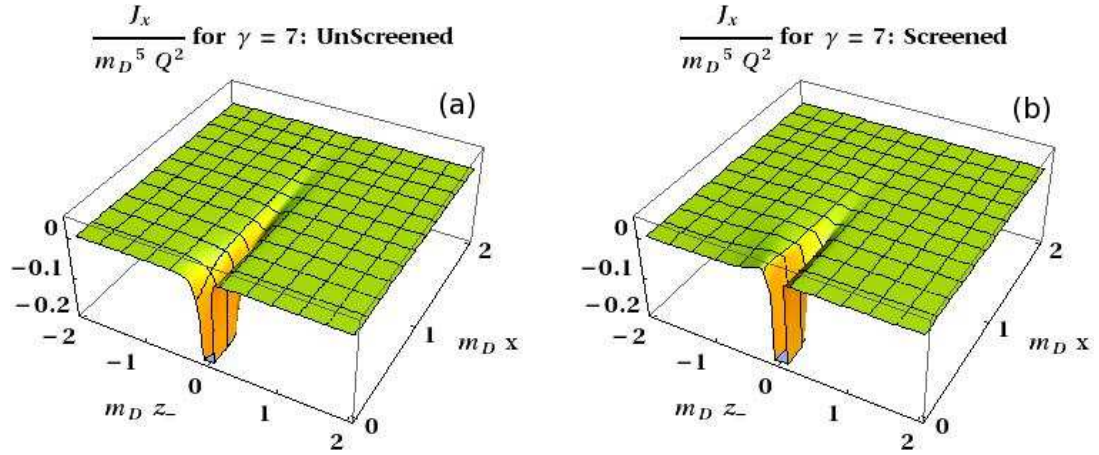


FIGURE 3.6: Plots of the scaled transverse momentum density deposited per unit time both with and without medium screening included for the same parameters as in Fig. 3.5. The structure shows noticeable differences in the two cases. In particular, the screened result has a positive bump just behind the source parton which is absent in the unscreened result.

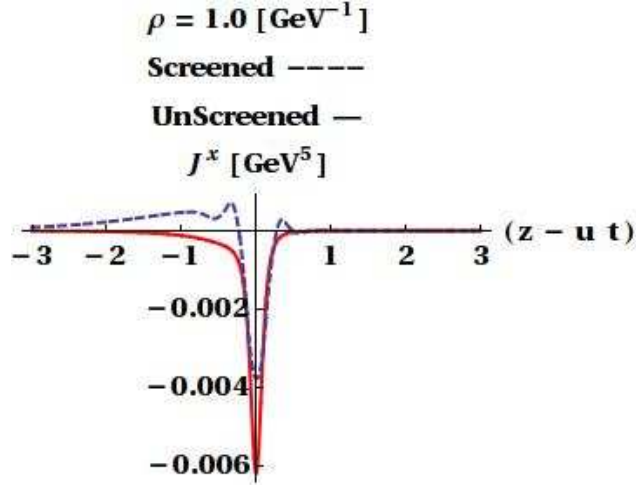


FIGURE 3.7: Plot of transverse momentum density deposited per unit time by a gluon both with and without medium screening included (compare with Fig. 3.6). The plot is for $u = 0.99$, $m_D = 0.4$ GeV, and $\alpha_s = 1/\pi$.

connection, $U_{ab}(x, x')$, and the choice of fields (3.18 - 3.20). Another assumption is that the medium is in local thermal equilibrium. This is the basic assumption of hydrodynamics and is necessary to obtain (3.25). I also assume that the typical momentum transfer between the source particle and the medium is small compared to the typical momentum of a medium particle. This assumption allows the straight line approximation given by (3.33). To get an idea of where this last assumption breaks down one can use the equipartition theorem for massless particles to find a relation between the typical momentum of a medium particle and the temperature: $\bar{p} = 3T$. For $T = 350$ MeV the typical momentum of a medium particle is about 1 GeV which places an upper limit on typical momentum transfers. It follows that the straight line approximation breaks down somewhere on the order of $k \geq 1$ GeV⁻¹ (or distances less than 0.2 fm).

In the absence of the medium's response to screen the fields, it was possible to obtain an analytical result which is given by (3.57) and (3.58). This result shows many similarities to the result obtained when the medium's response to screen the color field is included. The most noticeable differences appear in the transverse momentum density distribution. The total energy deposited per unit time is obtained by integrating $J^0(\rho, z, t)$ over all space and is given by (3.59) for the unscreened result.

Hydrodynamic Source Term with Radiation

In¹ the previous chapter the hydrodynamic source of energy and momentum generated by a fast parton in a QGP was calculated using kinetic theory. The result captured the spatial structure of the energy and momentum deposition, assuming the fast parton to be moving with constant velocity. However, the possibility of the fast parton to emit radiation was not considered, rather only the collisional energy loss was included.

In this chapter, I calculate the hydrodynamic source of energy and momentum generated by a fast parton including both collisional and radiative energy losses. The approach will be quite different than that adopted in the previous chapter, where the full spatial structure of the source term was calculated. Here, the fast parton is treated as a point source of energy and momentum deposition, and the source term becomes a delta function centered at the position of the fast parton, whose coefficient is given by the rate of energy absorbed by the medium. Thus, rather than be concerned with the spatial structure of the source, in this chapter I am interested

¹ Much of the work in this chapter originally appeared in a journal article I co-authored with Berndt Müller: R. B. Neufeld and B. Müller, *The sound produced by a fast parton in the quark-gluon plasma is a crescendo*, Phys. Rev. Letters (in production 2009)

simply in how the magnitude of the energy absorbed by the medium evolves in time. As discussed in the previous chapter, hydrodynamics is valid at large distance scales, so ignoring the spatial structure and focusing on the magnitude of the source should be a reasonable first approximation.

As a fast parton propagates through the medium, it loses energy through collisions and medium induced radiation. The collisional energy loss goes directly into medium excitation, however, the radiated gluons still need to deposit their energy. The energy deposited into the medium per unit length is then the sum of the collisional energy loss of the primary parton and of the radiated gluons. In what follows, I calculate the total energy deposited into the medium per unit length by a fast parton traversing a quark-gluon plasma. The medium excitation due to collisions is taken to be given by the well-known expression for the collisional drag force [63]. To calculate the medium excitation due to radiation, I begin by deriving a differential equation which describes how the spectrum of radiated gluons is modified as the radiated gluons lose energy through collisions. This modified spectrum is then used to calculate the differential energy loss due to the interactions of radiated gluons with the medium, from which I find that the energy which goes into medium excitation is substantially less than the total radiative energy loss. The final result for the energy deposited into the medium per unit length, which is a sum of the primary and the secondary contributions, is then treated as the coefficient of a local hydrodynamic source term.

4.1 Calculating the Energy Absorption

I start by considering the collisional energy lost per unit length by a fast parton in the quark-gluon plasma. As mentioned above, for the collisional energy loss I will use the familiar perturbative QCD expression [63]

$$\left(\frac{dE}{d\xi}\right)_C = \frac{\alpha_s C_2 m_D^2}{2} \ln \frac{2\sqrt{E_p T}}{m_D} \quad (4.1)$$

where $\alpha_s = g^2/4\pi$ is the strong coupling, m_D is the Debye mass of the medium, which I take to be given by $m_D = gT$, E_p is the energy of the fast parton, T is the temperature of the medium, and C_2 is the eigenvalue of the quadratic Casimir operator of the color charge of the source parton, which is 4/3 if the fast parton is a quark, and 3 for a gluon (I consider $N_c = 3$). In (4.1), the subscript C denotes collisional energy loss and ξ is the path-length traveled by the source parton.

I am next interested in calculating the energy deposited, or gained by the medium, due to gluons radiated by the fast parton. I begin by defining the quantity $f(\omega, \xi) \equiv dI_M/d\omega$, which gives the spectrum of radiated gluons with energy ω in the medium. $f(\omega, \xi)$ is in general different than $dI/d\omega$, which is the spectrum of gluons emitted by the fast parton, because gluons, once emitted, lose energy in the medium due to collisions until they become part of the thermal bath. As a gluon with energy ω travels from ξ to $\xi + \Delta\xi$, it loses collisional energy $\epsilon(\omega) \Delta\xi$, where $\epsilon(\omega)$ is obtained from (4.1) to be

$$\epsilon(\omega) = \frac{3}{2}\alpha_s m_D^2 \ln \frac{2\sqrt{\omega T}}{m_D}. \quad (4.2)$$

Thus, in the absence of incremental radiation, in order to find a gluon with energy ω at position $\xi + \Delta\xi$, there must be a gluon with energy $\omega + \epsilon(\omega) \Delta\xi$ at position ξ . Additionally, I require the total number of gluons, that is, $f d\omega$, to be invariant. This means that as $\omega \rightarrow \omega + \epsilon(\omega) \Delta\xi$ one has $d\omega \rightarrow d\omega(1 + \frac{\partial\epsilon(\omega)}{\partial\omega}\Delta\xi)$. In equation form, this is

$$f(\omega, \xi + \Delta\xi) = f(\omega + \epsilon(\omega) \Delta\xi, \xi)(1 + \frac{\partial\epsilon(\omega)}{\partial\omega}\Delta\xi). \quad (4.3)$$

Furthermore, as the fast parton moves from ξ to $\xi + \Delta\xi$, it will emit additional gluons, $\Delta\xi \times dI/d\omega d\xi$, which add to $f(\omega, \xi + \Delta\xi)$. The evolution equation for $f(\omega, \xi)$ thus takes the form

$$\frac{\partial}{\partial\xi}f(\omega, \xi) - \frac{\partial}{\partial\omega}[\epsilon(\omega) f(\omega, \xi)] = \frac{dI}{d\omega d\xi}(\omega, \xi) \quad (4.4)$$

where I have taken the limit of $\Delta\xi \rightarrow 0$.

Equation (4.4) provides a partial differential equation through which one can determine the spectrum of radiated gluons in the medium, $f(\omega, \xi)$. In order to solve for f , it is necessary to specify $dI/d\omega d\xi$. I choose the spectrum calculated by Salgado and Wiedemann in the multiple soft scattering approximation [64]

$$\frac{dI}{d\omega d\xi} = -\frac{\sqrt{\hat{q}}\alpha_s C_2}{\pi} \text{Re} \frac{(1+i) \tan \left[(1+i) \sqrt{\frac{\hat{q}}{\omega}} \frac{\xi}{2} \right]}{\omega^{3/2}} \quad (4.5)$$

where I use [65]

$$\hat{q} = 2\alpha_s C_2 m_D^2 T \ln \frac{2\sqrt{E_p T}}{m_D}, \quad (4.6)$$

where the logarithm is consistent with (4.1).

In my approach, $f(\omega, \xi)$ consists of two components: energetic gluons which lose energy through collisions and low energy gluons which become a part of the medium. The total energy being dumped into the medium is then given by the sum of the collisional energy loss of high energy gluons and the energy absorbed by the medium in the form of low energy gluons. I make the distinction that gluons with $\omega > \bar{\omega} \equiv 2T$ are sources of collisional energy loss, while those with less energy are considered as immediately part of the medium. For $\omega > \bar{\omega}$ I solve for $f(\omega, \xi)$ numerically from equation (4.4) for a primary quark using the parameters: $\alpha_s = 1/\pi$, $T = 350$ MeV, and $E_p = 50$ GeV. The total energy deposited into the medium by the secondary gluons per unit length is then given by

$$\left(\frac{dE}{d\xi} \right)_R = \int_{\bar{\omega}}^{\omega_{\max}} d\omega \epsilon(\omega) f(\omega, \xi) + \int_0^{\bar{\omega}} d\omega \omega \frac{dI}{d\omega d\xi} + \bar{\omega} f(\bar{\omega}, \xi) \epsilon(\bar{\omega}), \quad (4.7)$$

where I set $\omega_{\max} = E_p/2$. The last term in equation (4.7) accounts for energetic gluons which have lost enough energy to become a part of the medium and thus

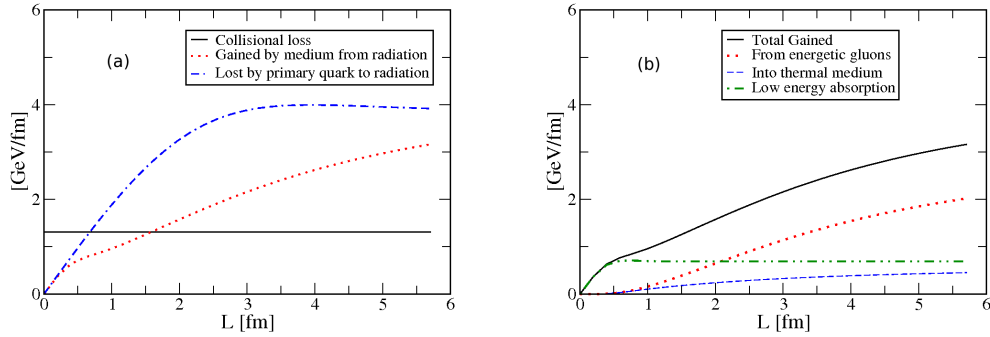


FIGURE 4.1: Plot (a) shows the differential energy lost by the fast parton due to radiation and that gained by the medium as a function of path-length, L , as well as the collisional energy loss (the specific parameters are discussed in the text). The differential energy deposition into the medium is the sum of the solid (black) and dotted (red) lines. Plot (b) shows the breakdown of various the contributions to the radiative energy gained by the medium. The dotted (red) line shows the collisional energy loss of the radiated gluons. The dash-dotted (green) line shows the the energy radiated in gluons with energy below $\bar{\omega}$, which are assumed to immediately become part of the medium. The (blue) curve marked 'Into thermal medium' denotes the last term in (4.7).

deposit their entire remaining energy. When solving (4.4), I multiply the spectrum (4.5) by a factor of $1 - (\omega/\omega_{\max})^8$ to ensure it goes to zero at $\omega = \omega_{\max}$.

The result of (4.7) is shown as the dotted red line in Fig. 4.1(a) for the same parameters listed above, along with the differential collisional energy loss of the primary parton (solid black line) and its differential energy loss to radiation (dashed blue curve). One sees that the energy deposited by the radiation into the medium per unit length has an approximately linear growth in pathlength, which results from the steady increase in the number of gluons that deposit energy in collisions. This linear growth is thus of a different origin than what is observed in the first few fm of the differential energy loss to radiation, which is caused by the energy dependent coherence length for radiated gluons. If one continues the curves shown in Fig. 4.1(a) out to a large enough pathlength, the dotted red line reaches a steady state solution and merges with the dashed blue curve. The individual contributions

on the right-hand side of (4.7) are shown separately in Fig. 4.1(b), together with their sum.

The total energy deposited into the medium per unit length, or time, is given by the sum of (4.1) and (4.7), which I write as

$$\frac{dE}{dt} = \left(\frac{dE}{dt}\right)_C + \left(\frac{dE}{dt}\right)_R \quad (4.8)$$

As discussed previously, I treat the fast parton as a point source of energy and momentum deposition in the medium, with velocity \mathbf{u} and energy E_p . The hydrodynamic source term, denoted as J^ν , gives the energy and momentum density deposited in the medium per unit time. For a relativistic point source, J^ν takes the following form

$$J^\nu(x) = \frac{dE}{dt} \delta(\mathbf{x} - \mathbf{u}t) (1, \mathbf{u}) \quad (4.9)$$

where dE/dt is given by (4.8). For future reference, I note that the result of (4.7) can be fit to a linear curve, from which it is found that

$$\left(\frac{dE}{dt}\right)_R \approx 0.474 \frac{\text{GeV}}{\text{fm}} + 0.51 t \frac{\text{GeV}}{\text{fm}^2}. \quad (4.10)$$

The fit slightly overestimates the energy deposition rate for $t < 0.5 \text{ fm}/c$. I will be interested in considering two fast partons created in an initial hard interaction at time $t = 0$, which then propagate back to back for some time, t_M , before being absorbed by the medium. In this case (4.9) is modified to

$$J^\nu(x) = \frac{dE}{dt} (\Theta(t) - \Theta(t - t_M)) \times [\delta(\mathbf{x} - \mathbf{u}t) (1, \mathbf{u}) + \delta(\mathbf{x} + \mathbf{u}t) (1, -\mathbf{u})] \quad (4.11)$$

where $\Theta(t)$ is 1 if $t > 0$ and zero otherwise.

4.2 Discussion

In this chapter I have derived an expression for the total energy deposited into the medium per unit length (or time) by a fast parton propagating in the quark-gluon plasma, including both collisional and radiative energy deposition. I have shown that while the differential energy loss due to radiation is quite large, the contribution to medium excitation is more modest, but growing with path length. This result is similar, but less dramatic than the increase of the energy deposition by a light quark obtained in the strongly coupled supersymmetric Yang-Mills theory [66]. In my formalism, the magnitude of the wave depends on the specific value (4.6) of \hat{q} , as well as to the collisional energy loss (4.1). It is possible that in the quark-gluon plasma produced at RHIC either one or both of these has a larger value than that assumed here (see Bass *et al.* [67] for a range of values of \hat{q} compatible with experimental data). A general feature of the above result is that the perturbation created in the QCD medium by a fast parton will be dominated by the last stage of the phase in which color charges are deconfined and highly mobile, *i. e.* just before bulk hadronization. This observation is consistent with the measured peak emission angle of secondary hadrons in the backward direction [72], which correspond to a small sound velocity $c_s/c \approx 0.3$ as deduced from lattice QCD for $T \approx T_c$.

In the previous two chapters, two different approaches have been presented for calculating the hydrodynamic source term generated by a fast parton in the QGP. Up until now, however, nothing has been said regarding solving the hydrodynamic equations coupled to a source. In Chapter 6, this will be addressed by presenting a detailed method of solution for the hydrodynamic evolution with a source term. Numerical results will be presented for a wide range of parameters and scenarios. In Chapter 5, I consider a different approach for calculating the response of a QGP to fast partons by utilizing finite temperature field theory.

Finite Temperature Field Theory Evaluation

In this chapter I consider a different perspective on analyzing the response of a QGP to fast partons by utilizing finite temperature field theory. For simplicity, a scalar field with quartic interaction will be examined first. Afterward, the connection to QCD will be discussed. It will not be my purpose to here go into great detail about the background of finite temperature field theory, but rather I will focus on how to apply it to a particular problem of interest. The interested reader can consult [68] for an introduction to the background theory.

5.1 Scalar Theory with Source

5.1.1 General Form of the Energy Momentum Tensor

Consider a scalar field, ϕ , with quartic self interaction and coupled to an external source. The Lagrangian for this theory is given by

$$\mathcal{L}(x) = \frac{1}{2}\partial_\mu\phi(x)\partial^\mu\phi(x) - \frac{1}{2}m^2\phi(x)^2 - j(x)\phi(x) - \frac{\lambda}{4!}\phi(x)^4 \quad (5.1)$$

where m is the mass of the field, $\frac{\lambda}{4!}$ is the strength of the self-interaction, and $j(x) = g\delta(\mathbf{x} - \mathbf{ut})$ is the strength of the external source. In what follows I will neglect the

mass term, m . The energy-momentum tensor of this theory is given by [69]

$$T^{\mu\nu} = \partial^\mu \phi \partial^\nu \phi - g^{\mu\nu} \mathcal{L}. \quad (5.2)$$

To make connection to the previous chapters, I'll be interested in calculating the source of energy and momentum generated in the medium, or $\partial_\mu T^{\mu\nu}$, by the source, $j(x)$. Consider first the terms in $T^{\mu\nu}$ with derivatives. These can be related to the two point correlation function between the field at position x and y as follows:

$$\partial^\mu \phi \partial^\nu \phi = \lim_{y \rightarrow x} \partial_x^\mu \partial_y^\nu \langle \phi(x) \phi(y) \rangle \quad (5.3)$$

and

$$\partial_\mu \phi \partial^\mu \phi = \lim_{y \rightarrow x} \partial_\mu^x \partial_y^\mu \langle \phi(x) \phi(y) \rangle. \quad (5.4)$$

In this case,

$$\partial_\mu T_D^{\mu\nu} = \frac{1}{2} \lim_{y \rightarrow x} (\partial_\mu^x + \partial_\mu^y) [\partial_x^\mu \partial_y^\nu + \partial_x^\nu \partial_y^\mu - g^{\mu\nu} \partial_\mu^x \partial_y^\mu] \langle \phi(x) \phi(y) \rangle \quad (5.5)$$

where the subscript D indicates terms with derivatives and the first derivative term has been symmetrized with respect to x and y . This symmetrization with respect to x and y is simply a matter of convenience. $\langle \phi(x) \phi(y) \rangle$ is equivalent to $\langle \phi(y) \phi(x) \rangle$ so that in any calculation the symmetry will be present.

Consider the momentum space representation of (5.5). In that case, if one assigns a momentum p_1 to x , and p_2 to y , the derivative structure is

$$\frac{i}{2} (p_{1\mu} + p_{2\mu}) [p_1^\mu p_2^\nu + p_1^\nu p_2^\mu - g^{\mu\nu} p_1 \cdot p_2] = \frac{i}{2} (p_1^2 p_2^\nu + p_2^2 p_1^\nu). \quad (5.6)$$

The result (5.6) will be useful in later calculations. One must also include the ϕ^4 term in $\partial_\mu T^{\mu\nu}$, which gives

$$\partial_\mu T_Q^{\mu\nu} = \partial^\nu \frac{\lambda}{4!} \langle \phi(x)^4 \rangle. \quad (5.7)$$

where the subscript Q indicates the quartic term. I don't include the source term, $j(x)\phi(x)$, in the energy momentum tensor because it's considered to be external to the system. The goal is to now calculate $\langle\phi(x)\phi(y)\rangle$ and $\langle\phi(x)^4\rangle$ to determine $\partial_\mu T^{\mu\nu}$.

5.1.2 Calculating Correlation Functions in Real Time

I am here interested in using real-time finite temperature field theory to calculate the correlation functions, $\langle\phi(x)\phi(y)\rangle$ and $\langle\phi(x)^4\rangle$. As mentioned above, I will not go into great background detail but rather focus on a particular problem of interest. Recall from statistical mechanics that the thermal average of some operator, \hat{A} , is given by

$$\langle A \rangle = \frac{\text{Tr } \hat{A} e^{-\beta \hat{H}}}{\text{Tr } e^{-\beta \hat{H}}} \quad (5.8)$$

where I do not include any chemical potential and β is the inverse temperature. The quantity $\text{Tr } e^{-\beta \hat{H}} \equiv Z$ is the partition function of the system and is the most important function of thermodynamics.

The great power of finite temperature field theory is to be able to cast the partition function in terms of a functional integration, which in turn allows perturbative or lattice techniques to be used. In particular, for a scalar field ϕ the partition function takes the form

$$Z = \int d\phi \langle \phi | e^{-\beta \hat{H}} | \phi \rangle = \int \mathcal{D}\phi e^{\int_0^\beta d\tau \int d^3z \mathcal{L}(\tau, \mathbf{z})} \quad (5.9)$$

where $\tau \equiv it$ and there is a restriction that $\phi(0, \mathbf{z}) = \phi(\beta, \mathbf{z})$. No attempt has been made to prove the above relation, which is done in any textbook on finite temperature field theory.

Because the time variable in (5.9) is imaginary, its use is often termed the *imaginary time formalism*. The great restriction of the imaginary time formalism is that it can only be applied to static, or time-independent, quantities. However, there is

an alternate formulation of finite temperature field theory which allows the calculation of time-dependent quantities called the *real time formalism*. In the real time formalism, one essentially doubles the degrees of freedom. Fields can be on what are here referred to as the + and - contours. In this formalism, the partition function is

$$Z = \int \mathcal{D}\phi e^{i \int_c d^4z \mathcal{L}} \quad (5.10)$$

where the time variable is real and the the time integration goes from $-\infty$ to ∞ . The notation $\int_c d^4z$ indicates that both the + and - contours must be integrated over

$$\int_c d^4z = \int_+ d^4z - \int_- d^4z. \quad (5.11)$$

In a perturbative expansion, any correlation function can be cast into a function of free field (without any interactions) 2 particle correlations using Wick's theorem. Thus, all that is needed is the representation of the free field two particle correlation functions. There are four to consider, because any two fields can be on ++, +-, -+ or -- contours. The time ordered, free field 2 particle correlations for a scalar field theory are given by

$$\begin{aligned} \langle \phi(x)\phi(y) \rangle_0 &= \int \frac{d^4p}{(2\pi)^4} i e^{-ip \cdot (x-y)} G_{++}(p) \quad x \text{ and } y \text{ on } + \\ \langle \phi(x)\phi(y) \rangle_0 &= \int \frac{d^4p}{(2\pi)^4} i e^{-ip \cdot (x-y)} G_{+-}(p) \quad x \text{ on } + \text{ and } y \text{ on } - \\ \langle \phi(x)\phi(y) \rangle_0 &= \int \frac{d^4p}{(2\pi)^4} i e^{-ip \cdot (x-y)} G_{-+}(p) \quad x \text{ on } - \text{ and } y \text{ on } + \\ \langle \phi(x)\phi(y) \rangle_0 &= \int \frac{d^4p}{(2\pi)^4} i e^{-ip \cdot (x-y)} G_{--}(p) \quad x \text{ and } y \text{ on } - \end{aligned} \quad (5.12)$$

where

$$\begin{aligned}
G_{++}(p) &= \frac{1}{p^2 - m^2 + i\epsilon} - 2\pi i n_B(|p^0|) \delta(p^2 - m^2) \\
G_{+-}(p) &= -2\pi i (\theta(-p^0) + n_B(|p^0|)) \delta(p^2 - m^2) \\
G_{-+}(p) &= -2\pi i (\theta(p^0) + n_B(|p^0|)) \delta(p^2 - m^2) \\
G_{--}(p) &= -\frac{1}{p^2 - m^2 - i\epsilon} - 2\pi i n_B(|p^0|) \delta(p^2 - m^2)
\end{aligned} \tag{5.13}$$

and n_B is the Bose-Distribution. It is also helpful to note the following relations

$$\begin{aligned}
G_R(p) &= \frac{1}{p^2 - m^2 + i\epsilon p^0} = G_{++} - G_{+-} = G_{-+} - G_{--} \\
G_A(p) &= \frac{1}{p^2 - m^2 - i\epsilon p^0} = G_{++} - G_{-+} = G_{+-} - G_{--} \\
G_C(p) &= -2\pi i (1 + 2n_B(|p^0|)) \delta(p^2 - m^2) = G_{++} + G_{--} = G_{+-} + G_{-+}.
\end{aligned} \tag{5.14}$$

5.1.3 Calculating the Source of Energy and Momentum

With the above definitions in place, it is now possible to consider the correlation functions, $\langle \phi(x)\phi(y) \rangle$ and $\langle \phi(x)^4 \rangle$. The convention is that both $\phi(x)$ and $\phi(y)$ are on the + contour. Final results should not depend on which contour one chooses for the fields $\phi(x)$ and $\phi(y)$.

The Two Point Contribution

First consider $\langle \phi(x)\phi(y) \rangle$, which is written as

$$\langle \phi(x)\phi(y) \rangle = \frac{\int \mathcal{D}\phi \phi(x)\phi(y) \mathcal{D}\phi e^{i \int_c d^4z \mathcal{L}}}{\int \mathcal{D}\phi e^{i \int_c d^4z \mathcal{L}}} \tag{5.15}$$

where \mathcal{L} is given in (5.1). Treating both λ and g as parameters for a perturbative expansion, the lowest order contributions are

$$\begin{aligned}
&\langle \phi(x)\phi(y) \rangle_I = \\
&\frac{\int \mathcal{D}\phi \phi(x)\phi(y) e^{iS_0} (1 - \frac{g^2}{2} \int_c d^4r d^4w j(r)j(w)\phi(r)\phi(w)) (1 - i\frac{\lambda}{4!} \int_c d^4z \phi(z)^4)}{\int \mathcal{D}\phi e^{iS_0} (1 - \frac{g^2}{2} \int_c d^4r d^4w j(r)j(w)\phi(r)\phi(w)) (1 - i\frac{\lambda}{4!} \int_c d^4z \phi(z)^4)}.
\end{aligned} \tag{5.16}$$

where the subscript I means interacting, and all other quantities are free field. The right hand side (RHS) of the above expression can be turned into correlation functions by multiplying both the numerator and the denominator by the partition function. Then, expanding the denominator in powers of the coupling terms yields a polynomial expression for $\langle \phi(x)\phi(y) \rangle_I$. I am only interested in interaction terms which have a $g^2\lambda$ coupling. Terms with only g^2 do not couple to the medium, and are temperature independent. They reflect the source's interaction with the vacuum. Terms with only λ do not couple to the source. In this case, after straightforward manipulation

$$\begin{aligned} \langle \phi_x \phi_y \rangle_I &= \langle \phi_x \phi_y \rangle + i \frac{g^2 \lambda}{2(4!)} \int_{c,r,w,z} j_r j_w (\langle \phi_x \phi_y \phi_r \phi_w \phi_z^4 \rangle - \langle \phi_x \phi_y \rangle \langle \phi_r \phi_w \phi_z^4 \rangle \\ &\quad - \langle \phi_x \phi_y \phi_r \phi_w \rangle \langle \phi_z^4 \rangle - \langle \phi_x \phi_y \phi_z^4 \rangle \langle \phi_r \phi_w \rangle) \end{aligned} \quad (5.17)$$

where $\phi_x = \phi(x)$, etc., and $\int_{c,r} = \int_c d^4r$ etc.

As mentioned above, Wick's theorem allows correlations of many fields to be written as products of correlations of two fields. One finds

$$\begin{aligned} &\langle \phi_x \phi_y \phi_r \phi_w \phi_z^4 \rangle - \langle \phi_x \phi_y \rangle \langle \phi_r \phi_w \phi_z^4 \rangle - \langle \phi_x \phi_y \phi_r \phi_w \rangle \langle \phi_z^4 \rangle - \langle \phi_x \phi_y \phi_z^4 \rangle \langle \phi_r \phi_w \rangle = \\ &12 (\langle \phi_x \phi_r \rangle \langle \phi_y \phi_z \rangle \langle \phi_w \phi_z \rangle \langle \phi_z \phi_z \rangle + x \leftrightarrow y) + 12 (\langle \phi_x \phi_w \rangle \langle \phi_y \phi_z \rangle \langle \phi_r \phi_z \rangle \langle \phi_z \phi_z \rangle + x \leftrightarrow y) \\ &+ 24 \langle \phi_x \phi_z \rangle \langle \phi_y \phi_z \rangle \langle \phi_w \phi_z \rangle \langle \phi_r \phi_z \rangle. \end{aligned} \quad (5.18)$$

Then, ignoring the free field contribution,

$$\begin{aligned} \langle \phi_x \phi_y \rangle_I &= i \frac{g^2 \lambda}{4} \int_{c,r,w,z} j_r j_w [(\langle \phi_x \phi_r \rangle \langle \phi_y \phi_z \rangle \langle \phi_w \phi_z \rangle \langle \phi_z \phi_z \rangle + x \leftrightarrow y) \\ &\quad + (\langle \phi_x \phi_w \rangle \langle \phi_y \phi_z \rangle \langle \phi_r \phi_z \rangle \langle \phi_z \phi_z \rangle + x \leftrightarrow y) + 2 \langle \phi_x \phi_z \rangle \langle \phi_y \phi_z \rangle \langle \phi_w \phi_z \rangle \langle \phi_r \phi_z \rangle]. \end{aligned} \quad (5.19)$$

Equation (5.19) has three distinct terms, which I label as

$$T_1 \equiv i \frac{g^2 \lambda}{4} \int_{c,r,w,z} j_r j_w \langle \phi_x \phi_r \rangle \langle \phi_y \phi_z \rangle \langle \phi_w \phi_z \rangle \langle \phi_z \phi_z \rangle + x \leftrightarrow y \quad (5.20)$$

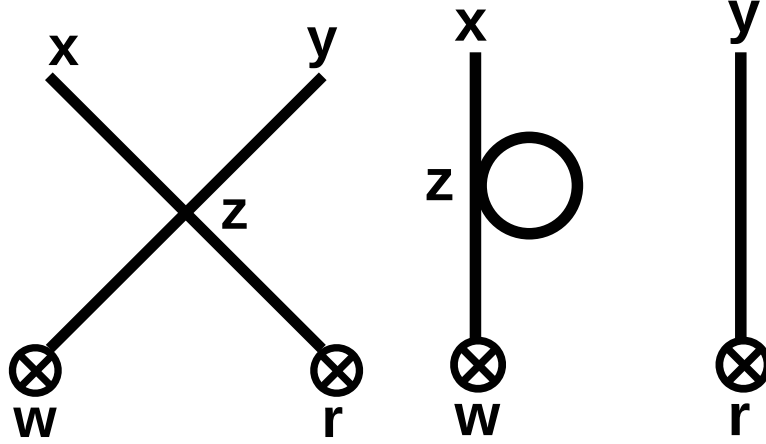


FIGURE 5.1: Representative diagrams of the ϕ^4 theory with a source. The diagram on the left represents the lowest order source/medium interaction, while the diagram on the right contributes to the screening of the source field.

$$T_2 \equiv i \frac{g^2 \lambda}{4} \int_{c,r,w,z} j_r j_w \langle \phi_x \phi_w \rangle \langle \phi_y \phi_z \rangle \langle \phi_r \phi_z \rangle \langle \phi_z \phi_z \rangle + x \leftrightarrow y \quad (5.21)$$

and

$$T_3 \equiv i \frac{g^2 \lambda}{2} \int_{c,r,w,z} j_r j_w \langle \phi_x \phi_z \rangle \langle \phi_y \phi_z \rangle \langle \phi_w \phi_z \rangle \langle \phi_r \phi_z \rangle. \quad (5.22)$$

It is instructive to consider the diagrammatic representation of T_1 , T_2 and T_3 , which is done in Figure 5.1. The diagram on the left represents T_3 , while the diagram on the right is representative of T_1 and T_2 . It's clear that T_1 and T_2 contribute to the screening of the field due to thermal interactions, but are not indicative of the essential source/medium interaction. They provide a thermal correction to the source's interaction with the vacuum. However, T_3 legitimately represents the lowest order source/medium interaction from $\langle \phi(x)\phi(y) \rangle$, thus I'll consider that term.

To evaluate T_3 , it's helpful to write the r and w integrations as a product

$$T_3 = i \frac{g^2 \lambda}{2} \left(\int_{z_+} \langle \phi_x \phi_z \rangle \langle \phi_y \phi_z \rangle - \int_{z_-} \langle \phi_x \phi_z \rangle \langle \phi_y \phi_z \rangle \right) \left[\int_{c,r} j_r \langle \phi_r \phi_z \rangle \right]^2 \quad (5.23)$$

in which case one can consider the evaluation of

$$\begin{aligned}
\int_{c,r} j_r \langle \phi_r \phi_{z\pm} \rangle &= i \int d^4r \frac{d^4p}{(2\pi)^4} \delta(\mathbf{r} - \mathbf{u}t_r) e^{ip \cdot (r-z)} (G_{+\pm}(p) - G_{-\pm}(p)) \\
&= i \int d^4r \frac{d^4p}{(2\pi)^4} \delta(\mathbf{r} - \mathbf{u}t_r) e^{ip \cdot (r-z)} G_{A/R}(p) \\
&= i \int d^4r \frac{d^4p}{(2\pi)^4} \delta(\mathbf{r} - \mathbf{u}t_r) e^{ip \cdot (r-z)} \frac{1}{p^2 \mp i\epsilon p^0}.
\end{aligned} \tag{5.24}$$

The integration over d^4r can be done trivially to yield a factor of $2\pi\delta(p^0 - \mathbf{u} \cdot \mathbf{p})$. Using the δ function to integrate out p^0 and the relation (3.39) to evaluate the azimuthal integration, one has

$$\int_{c,r} j_r \langle \phi_r \phi_{z+} \rangle = -i\gamma^2 \int \frac{dp_z dp_T p_T J_0(\rho p_T)}{(2\pi)^2} \frac{e^{ip_z(z_z - ut_z)}}{p_z^2 + \gamma^2 p_T^2 \pm i\epsilon p_z}. \tag{5.25}$$

The denominator can be factored as $(p_z - i\gamma p_T \pm i\epsilon)(p_z + i\gamma p_T \pm i\epsilon)$ from which it's clear that ϵ has no further role. The contour integral over dp_z then amounts to

$$\int \frac{dp_z}{2\pi} \frac{e^{ip_z(z_z - ut_z)}}{(p_z - i\gamma p_T + i\epsilon)(p_z + i\gamma p_T + i\epsilon)} = \frac{e^{-\gamma p_T |z_z - ut_z|}}{2\gamma p_T} \tag{5.26}$$

and finally

$$\int_{c,r} j_r \langle \phi_r \phi_{z\pm} \rangle = -i\gamma \int \frac{dp_T J_0(\rho p_T)}{(2\pi)} \frac{e^{-\gamma p_T |z_z - ut_z|}}{2} = -i \frac{\gamma}{4\pi} \frac{1}{\sqrt{\rho^2 + \gamma^2(z_z - ut_z)^2}}. \tag{5.27}$$

Going back to (5.23) gives

$$\begin{aligned}
T3 &= -i \frac{\gamma^2 g^2 \lambda}{32\pi^2} \left[\int_{z_+} \langle \phi_x \phi_z \rangle \langle \phi_y \phi_z \rangle - \int_{z_-} \langle \phi_x \phi_z \rangle \langle \phi_y \phi_z \rangle \right] \frac{1}{\rho^2 + \gamma^2(z_z - ut_z)^2} \\
&= i \frac{\gamma^2 g^2 \lambda}{32\pi^2} \int d^4z \frac{d^4p_1 d^4p_2}{(2\pi)^8} \frac{e^{-ip_1 \cdot (x-z) - ip_2 \cdot (y-z)}}{\rho^2 + \gamma^2(z_z - ut_z)^2} \\
&\quad \times [G_{++}(p_1)G_{++}(p_2) - G_{+-}(p_1)G_{+-}(p_2)].
\end{aligned} \tag{5.28}$$

Using (5.13) and (5.14) one can show that the term in brackets can be written as the sum of a vacuum contribution and temperature dependent contribution

$$\begin{aligned} & [G_{++}(p_1)G_{++}(p_2) - G_{+-}(p_1)G_{+-}(p_2)] = \\ & \text{VAC} - 2\pi i [n_B(|p_2^0|)\delta(p_2^2)G_R(p_1) + n_B(|p_1^0|)\delta(p_1^2)G_R(p_2)]. \end{aligned} \quad (5.29)$$

I am here interested in the temperature dependent contribution, in which case

$$\begin{aligned} T3 &= \frac{\gamma^2 g^2 \lambda}{16\pi} \int d^4 z \frac{d^4 p_1 d^4 p_2}{(2\pi)^8} \frac{e^{-ip_1 \cdot (x-z) - ip_2 \cdot (y-z)}}{\rho^2 + \gamma^2 (z_z - ut_z)^2} \\ & \times [n_B(|p_2^0|)\delta(p_2^2)G_R(p_1) + n_B(|p_1^0|)\delta(p_1^2)G_R(p_2)]. \end{aligned} \quad (5.30)$$

At this point, in order to make connection to $\partial_\mu T_D^{\mu\nu}$ it is helpful to recall (5.6), where it was shown that if one assigns a momentum p_1 to x , and p_2 to y , the derivative structure contributes $\frac{i}{2}(p_1^\nu p_2^\nu + p_2^\nu p_1^\nu)$. I then have

$$\begin{aligned} \partial_\mu T_D^{\mu\nu} &= i \frac{\gamma^2 g^2 \lambda}{32\pi} \int d^4 z \frac{d^4 p_1 d^4 p_2}{(2\pi)^8} \frac{e^{-i(p_1+p_2) \cdot (x-z)}}{\rho^2 + \gamma^2 (z_z - ut_z)^2} \\ & \times (p_1^\nu p_2^\nu + p_2^\nu p_1^\nu) [n_B(|p_2^0|)\delta(p_2^2)G_R(p_1) + n_B(|p_1^0|)\delta(p_1^2)G_R(p_2)]. \end{aligned} \quad (5.31)$$

where the limit of $y \rightarrow x$ has been taken. Enforcing the δ functions on p_1^2 and p_2^2 and using the relation

$$\lim_{\epsilon \rightarrow 0} \frac{p_1^2}{p_1^2 + i\epsilon p^0} \rightarrow 1 \quad (5.32)$$

finally gives

$$\begin{aligned} \partial_\mu T_D^{\mu\nu} &= i \frac{\gamma^2 g^2 \lambda}{16\pi} \int d^4 z \frac{d^4 p_1 d^4 p_2}{(2\pi)^8} \frac{e^{-i(p_1+p_2) \cdot (x-z)}}{\rho^2 + \gamma^2 (z_z - ut_z)^2} p_2^\nu n_B(|p_2^0|)\delta(p_2^2) \\ &= i \frac{\gamma^2 g^2 \lambda}{16\pi} \int d^4 z \frac{d^4 p_2}{(2\pi)^4} \frac{e^{-ip_2 \cdot (x-z)}}{\rho^2 + \gamma^2 (z_z - ut_z)^2} p_2^\nu n_B(|p_2^0|)\delta(p_2^2)\delta^4(x-z) \\ &= i \frac{\gamma^2 g^2 \lambda}{16\pi} \frac{1}{\rho^2 + \gamma^2 (x_z - ut_x)^2} \int \frac{d^4 p_2}{(2\pi)^4} p_2^\nu n_B(|p_2^0|)\delta(p_2^2) \\ &= 0. \end{aligned} \quad (5.33)$$

It's interesting that terms from the bare Lagrangian contribute nothing to $\partial_\mu T^{\mu\nu}$, even when a source is present. In some ways, it's not entirely surprising since in the absence of interactions $\partial_\mu T^{\mu\nu} = 0$. One expects the contribution from the interaction term, $\langle\phi(x)^4\rangle$ to provide a non-zero contribution.

The Four Point Contribution

I now consider the interaction term from the Lagrangian, which as shown above is given by

$$\partial_\mu T_Q^{\mu\nu} = \partial^\nu \frac{\lambda}{4!} \langle\phi(x)^4\rangle. \quad (5.34)$$

The lowest order contributions in both λ and g are

$$\partial_\mu T^{\mu\nu} = \partial^\nu \frac{\lambda}{4!} \frac{\int \mathcal{D}\phi \phi(x)^4 e^{iS_0} (1 - \frac{g^2}{2} \int_c d^4r d^4w j(r)j(w)\phi(r)\phi(w))}{\int \mathcal{D}\phi e^{iS_0} (1 - \frac{g^2}{2} \int_c d^4r d^4w j(r)j(w)\phi(r)\phi(w))} \quad (5.35)$$

where the subscript has been dropped, since this is now the only contribution to $\partial_\mu T^{\mu\nu}$. As discussed above, I am interested in interaction terms which have a $g^2\lambda$ coupling. In this case the relevant contribution is found to be

$$\begin{aligned} \partial_\mu T^{\mu\nu} &= -\partial^\nu \frac{g^2\lambda}{48} \int_{c,r,w} j_r j_w (\langle\phi_x^4 \phi_r \phi_w\rangle - \langle\phi_x^4\rangle \langle\phi_r \phi_w\rangle) \\ &= -\partial^\nu \frac{g^2\lambda}{4} \int_{c,r,w} j_r j_w \langle\phi_x \phi_r\rangle \langle\phi_x \phi_w\rangle \langle\phi_x \phi_x\rangle. \end{aligned} \quad (5.36)$$

It was shown previously that

$$\left[\int_{c,r} j_r \langle\phi_x + \phi_r\rangle \right]^2 = -\frac{\gamma^2}{16\pi^2} \frac{1}{\rho^2 + \gamma^2(x_z - ut_x)^2} \quad (5.37)$$

so that one is left with

$$\partial_\mu T^{\mu\nu} = \frac{\gamma^2 g^2 \lambda}{64\pi^2} \partial^\nu \frac{1}{\rho^2 + \gamma^2(x_z - ut_x)^2} \langle\phi_x \phi_x\rangle. \quad (5.38)$$

Finally, it is necessary to consider $\langle \phi_x^2 \rangle$. The convention is that x is chosen to be on the $+$ axis, which gives

$$\begin{aligned}
\langle \phi_x \phi_x \rangle &= \int \frac{d^4 p}{(2\pi)^4} i G_{++}(p) \\
&= \int \frac{d^4 p}{(2\pi)^4} i \left(\frac{1}{p^2 + i\epsilon} - 2\pi i n_B(|p^0|) \delta(p^2) \right) \\
&= \frac{1}{8\pi^3} \int d^4 p n_B(|p^0|) \delta(p^2) \\
&= \frac{1}{2\pi^2} \int_0^\infty dp \frac{p}{e^{\beta p} - 1} = \frac{T^2}{12}
\end{aligned} \tag{5.39}$$

where again I have ignored a purely vacuum contribution.

The end result is that

$$\partial_\mu T^{\mu\nu} = \frac{\gamma^2 g^2 T^2 \lambda}{768 \pi^2} \partial^\nu \frac{1}{\rho^2 + \gamma^2 (z - ut)^2} \tag{5.40}$$

As expected there is a non-zero contribution arising from the interaction term of the Lagrangian. It's interesting that the source term derived here is a pure derivative. For instance, the total energy deposited into the medium per unit time (compare to equation (3.59) for the QCD case) is

$$\frac{dE}{dt} \sim \int d\mathbf{x} \frac{(x_z - ut_x)}{\rho^2 + \gamma^2 (z - ut)^2} = 0. \tag{5.41}$$

Thus the net energy deposited into the medium vanishes. More will be said about the interesting dynamics of a pure gradient source term in Chapter 6.

5.2 Vlasov Equation for a Scalar Field Theory

In order to make a comparison to (5.40), consider the Vlasov equation of a scalar field with quartic interaction in the presence of an external field ϕ given by [70]

$$\left(p^\mu \partial_{x,\mu} + \frac{\lambda}{4} \partial_x^\mu (\phi(x)^2) \partial_{p,\mu} \right) f(x, p) = 0 \tag{5.42}$$

where the on-shell distribution function is taken to be

$$f(x, p) = n_B(p^0)\delta(p^2)_+ \quad (5.43)$$

and $\delta(p^2)_+$ indicates to sum only over the positive root of p^0 . Following the approach of chapter 3, I take moments in momentum space, but now include an integration over p^0

$$\int \frac{d^4 p p^\nu}{(2\pi)^3} \left(p^\mu \partial_{x,\mu} + \frac{\lambda}{4} \partial_x^\mu (\phi(x)^2) \partial_{p,\mu} \right) n_B(p^0)\delta(p^2)_+ = 0. \quad (5.44)$$

After integrating out the δ function, the first term in parenthesis becomes

$$\frac{1}{2} \int \frac{d\mathbf{p} p^\nu}{(2\pi)^3} v^\mu \frac{\partial n_B(p)}{\partial x^\mu} = \frac{1}{2} \partial_\mu T^{\mu\nu} \quad (5.45)$$

where the equality was seen before in equation (3.25). Now consider the second term of (5.44)

$$\frac{\lambda}{4} \partial_x^\mu (\phi(x)^2) \int \frac{d^4 p p^\nu}{(2\pi)^3} \partial_{p,\mu} n_B(p^0)\delta(p^2)_+ \quad (5.46)$$

After an integration by parts this is

$$-\frac{\lambda}{4} \partial_x^\nu (\phi(x)^2) \int \frac{d^4 p}{(2\pi)^3} n_B(p^0)\delta(p^2)_+ \quad (5.47)$$

The form of the integral was seen in (5.39)

$$\int \frac{d^4 p}{(2\pi)^3} n_B(p^0)\delta(p^2)_+ = \frac{1}{4\pi^2} \int_0^\infty dp \frac{p}{e^{\beta p} - 1} = \frac{T^2}{24}. \quad (5.48)$$

Finally, I find

$$\partial_\mu T^{\mu\nu} = \frac{T^2 \lambda}{48} \partial^\nu (\phi(x)^2). \quad (5.49)$$

It is now left to determine the external field ϕ generated by the source current $j(x) = g \delta(\mathbf{x} - \mathbf{u}t)$. The classical equation of motion for the field in the presence of a source is

$$\partial_\mu \partial^\mu \phi = -j. \quad (5.50)$$

In Fourier space, the source has the form

$$j(\mathbf{k}, \omega) = 2\pi g \delta(\omega - \mathbf{u} \cdot \mathbf{k}) \quad (5.51)$$

and the equation for $\phi(k)$ becomes

$$\phi(\mathbf{k}, \omega) = \frac{2\pi g \delta(\omega - \mathbf{u} \cdot \mathbf{k})}{\omega^2 - k^2}. \quad (5.52)$$

The field $\phi(\mathbf{x}, t)$ is determined with a reverse transform, to give

$$\begin{aligned} \phi(\mathbf{x}, t) &= \int \frac{d^4 k}{(2\pi)^4} \frac{2\pi g \delta(\omega - \mathbf{u} \cdot \mathbf{k})}{\omega^2 - k^2} e^{i\mathbf{k} \cdot \mathbf{x} - i\omega t} \\ &= g \int \frac{d^3 k}{(2\pi)^3} \frac{e^{i\mathbf{k} \cdot \mathbf{x} - iuk_z t}}{u^2 k_z^2 - k^2} \\ &= -\frac{g\gamma}{4\pi} \frac{1}{\sqrt{\rho^2 + \gamma^2 (z - ut)^2}}. \end{aligned} \quad (5.53)$$

The final result is

$$\partial_\mu T^{\mu\nu} = \frac{\gamma^2 g^2 T^2 \lambda}{768 \pi^2} \partial^\nu \frac{1}{\rho^2 + \gamma^2 (z - ut)^2} \quad (5.54)$$

which is identical to (5.40).

5.3 Discussion

It's nice to see (5.40) and (5.54) in agreement. This provides an independent check on the methods of Chapter 3. A subtlety arises when considering that the distribution in (5.43) is different than the distribution used in, for instance, (3.28). In particular, in Chapter 3 the distribution was already assumed to be on shell, with $p^0 = E(p)$, eliminating the need for the δ function seen in (5.43). If one went back to (3.22) and replaced

$$f_0(p) \rightarrow n_B(p^0) \delta(p^2)_+ \quad (5.55)$$

and let $d^3p \rightarrow d^4p$, consistent with (5.44), the end result (3.25) would be unchanged. In the derivation of Section 5.2, it was necessary to start with the distribution given by (5.43) because the original Vlasov equation had an explicit dependence upon p^0 , which was not the case in Chapter 3.

In the QCD case the interaction of the medium and the source occurred at two different times, t' and t in (3.17), making it qualitatively different than the ϕ^4 theory. However, QCD also has a 4 point gluon interaction which is similar in structure to the ϕ^4 interaction. It is possible that the Vlasov approach implemented in Chapter 3 misses some of the affects associated with the point-like interactions of the source and medium. On the other hand, in the limit of $t' \rightarrow t$ one expects the two interactions expressed in (3.17) to take on a point-like form, in which case the effects of the 4 point gluon interaction may be captured, at least qualitatively. The only way to test this is to perform the calculation for QCD which was done in section 5.1 of this chapter for the scalar theory. This comparison will be done in a future work.

Medium Response in Linearized Hydrodynamics

In¹ Chapters 3 and 4, different formalisms were presented to derive the hydrodynamic source term generated by a fast parton in the QGP. In this chapter, attention will now be given to solving the equations and examining the medium response at large distance scales. For ease of reference, all numerical results are contained in Sec. 6.3, while the technical manipulations are in Secs. 6.1 and 6.2. Readers primarily interested in the numerical results can skim through Secs. 6.1 and 6.2.

The first part of the chapter will focus on solving the hydrodynamic equations coupled to the source term derived in Chapter 3 from kinetic theory. In Sec. 6.1.1 I consider the general form of linearized hydrodynamics with a source term. In Sec. 6.1.2 the source term is expanded in terms of gradients of a delta function, in an effort to understand the relevance of finite source structure. Both the full source term and the delta function expanded form are then Fourier transformed into momentum space. In Sec. 6.1.3 the hydrodynamic equations are solved in terms of a one dimensional numerical integration. In Sec. 6.3.1 results are given for both the

¹ Some of the work in this chapter originally appeared in a journal article I authored: R. B. Neufeld, *Mach Cones in the quark-gluon plasma: viscosity, speed of sound, and effects of finite source structure*, Phys. Rev. C 79, 054909, (2009) [44]

full source and the delta function expanded version, as well as different values of the viscosity and speed of sound.

In the second part of the chapter, I examine the medium response when the equations are coupled to the source derived in Chapter 4. Then, in Sec. 6.3.2, results are presented for the case of two energetic back-to-back partons created in a hard interaction.

6.1 Kinetic Source Term

6.1.1 *Linearized Hydrodynamics With a Source Term*

Recall in Chapter 3 the source term was coupled to the ideal hydrodynamic energy-momentum tensor in equation (3.25). The rest of that chapter was devoted to explicitly evaluating the source term. The ideal hydrodynamic energy-momentum tensor given by (3.26) contains no off-equilibrium effects. Of course, any physical fluid will demonstrate non-ideal behavior, particularly in the presence of a disturbance such as the propagation of a fast quark. As discussed in Chapter 1, non-ideal behavior is described by viscous corrections. In hydrodynamics, the coefficients of viscosity are phenomenological input parameters. In what follows, the energy-momentum tensor given by (3.26) will be modified to include the first order deviations from equilibrium for a QGP with non-zero shear viscosity. In the derivation of (3.25), these off-equilibrium deviations would appear in the collision term of the Boltzmann equation (3.3). Here, they will be incorporated phenomenologically via the hydrodynamic equations of motion.

I consider the first order hydrodynamical equations for a medium with non-zero shear viscosity, η , in the presence of a source term, J^ν , which are of the form

$$\partial_\mu T^{\mu\nu} = J^\nu \tag{6.1}$$

where $T^{\mu\nu}$ is the energy-momentum tensor of the system. Assuming that the en-

ergy and momentum density deposited by the fast parton is small compared to the equilibrium energy density of the medium, the hydrodynamical equations (6.1) can be linearized. Defining $T^{\mu\nu} = T_0^{\mu\nu} + \delta T^{\mu\nu}$, where $\delta T^{\mu\nu}$ is the perturbation of the energy-momentum tensor resulting from the source in an otherwise static medium, one has

$$\partial_\mu \delta T^{\mu\nu} = J^\nu, \quad (6.2)$$

where $\partial_\mu T_0^{\mu\nu} = 0$ and $\delta T^{\mu\nu}$ is given by [71]

$$\begin{aligned} \delta T^{00} &\equiv \delta\epsilon, \quad \delta T^{0i} \equiv \mathbf{g}, \\ \delta T^{ij} &= \delta_{ij} c_s^2 \delta\epsilon - \frac{3}{4} \Gamma_s \left(\partial^i g^j + \partial^j g^i - \frac{2}{3} \delta_{ij} \nabla \cdot \mathbf{g} \right). \end{aligned} \quad (6.3)$$

In (6.3) c_s denotes the speed of sound, $\Gamma_s \equiv \frac{4\eta}{3(\epsilon_0 + p_0)} = \frac{4\eta}{3sT}$ is the sound attenuation length, and ϵ_0 and p_0 are the unperturbed energy density and pressure, respectively.

Introducing the general rule for Fourier transforms

$$F(\mathbf{x}, t) = \frac{1}{(2\pi)^4} \int d^3k \int d\omega e^{i\mathbf{k}\cdot\mathbf{x} - i\omega t} F(\mathbf{k}, \omega), \quad (6.4)$$

the equations given by (6.2) are written in momentum space as

$$J^0 = -i\omega \delta\epsilon + i\mathbf{k} \cdot \mathbf{g} \quad (6.5)$$

$$\mathbf{J} = -i\omega \mathbf{g} + i\mathbf{k} c_s^2 \delta\epsilon + \frac{3}{4} \Gamma_s \left(k^2 \mathbf{g} + \frac{\mathbf{k}}{3} (\mathbf{k} \cdot \mathbf{g}) \right). \quad (6.6)$$

Solving for $\mathbf{k} \cdot \mathbf{g}$ in (6.6) allows for $\delta\epsilon$ to be determined from (6.5):

$$\mathbf{k} \cdot \mathbf{g} = k g_L = \frac{\mathbf{k} \cdot \mathbf{J} - ik^2 c_s^2 \delta\epsilon}{-i\omega + \Gamma_s k^2} \quad (6.7)$$

hence

$$\delta\epsilon(\mathbf{k}, \omega) = \frac{ik J_L(\mathbf{k}, \omega) + J^0(\mathbf{k}, \omega)(i\omega - \Gamma_s k^2)}{\omega^2 - c_s^2 k^2 + i\Gamma_s \omega k^2} \quad (6.8)$$

where the source and perturbed momentum density vectors are divided into transverse and longitudinal parts: $\mathbf{g} = \hat{\mathbf{k}}g_L + \mathbf{g}_T$ and $\mathbf{J} = \hat{\mathbf{k}}J_L + \mathbf{J}_T$, with $\hat{\mathbf{k}}$ denoting the unit vector in the direction of \mathbf{k} . Similarly, one has from (6.5) and (6.8)

$$kg_L = -iJ^0 + \omega\delta\epsilon \quad (6.9)$$

yielding

$$\mathbf{g}_L(\mathbf{k}, \omega) = \hat{\mathbf{k}}g_L = \frac{i\omega\hat{\mathbf{k}}J_L(\mathbf{k}, \omega) + ic_s^2\mathbf{k}J^0(\mathbf{k}, \omega)}{\omega^2 - c_s^2k^2 + i\Gamma_s\omega k^2}. \quad (6.10)$$

The transverse part of \mathbf{g} can be obtained from (6.6). The calculation is simplified by considering that any part of \mathbf{g} proportional to \mathbf{k} is a part of \mathbf{g}_L . This leaves

$$\mathbf{g}_T(\mathbf{k}, \omega) = \mathbf{g} - \mathbf{g}_L = \frac{i\mathbf{J}_T(\mathbf{k}, \omega)}{\omega + \frac{3}{4}i\Gamma_s k^2}. \quad (6.11)$$

Equation (6.11) is a diffusion equation and the quantity \mathbf{g}_T is interpreted as diffusive momentum density generated by the fast parton. Equations (6.8, 6.10) describe damped sound waves propagating at speed c_s , it follows that $\delta\epsilon$ and \mathbf{g}_L are interpreted as the energy and momentum density carried by sound generated by the fast parton. The importance of the explicit form of the source term can be readily seen. In a homogeneous medium symmetries ensure that the source vector, \mathbf{J} , can be written generally as

$$\mathbf{J}(\mathbf{x}, t) = \mathbf{u}p(r) + \nabla q(r) \quad (6.12)$$

where \mathbf{u} is the velocity of the source particle and $p(r)$ and $q(r)$ are scalar functions of the (possibly Lorentz contracted) magnitude $r = \sqrt{(\mathbf{x} - \mathbf{u}t)^2}$. If we instead write (6.12) in momentum space we have (one can compare to equation (3.1))

$$\mathbf{J}(\mathbf{k}, \omega) = \mathbf{u} \int d^4x e^{ik \cdot x} p(r) + i\mathbf{k} \int d^4x e^{ik \cdot x} q(r) \quad (6.13)$$

and \mathbf{J}_T is found to be

$$\mathbf{J}_T(\mathbf{k}, \omega) = \mathbf{J} - \frac{\mathbf{k}(\mathbf{k} \cdot \mathbf{J})}{k^2} = \left(\frac{\mathbf{u}k^2 - \mathbf{k}(\mathbf{k} \cdot \mathbf{u})}{k^2} \right) \int d^4x e^{ik \cdot x} p(r) \quad (6.14)$$

so that $q(r)$ does not contribute to \mathbf{J}_T . If one chooses the source (6.12) such that $p(r) = 0$ then there is no excitation of the diffusive momentum density. It is clear that the hydrodynamics of the system are sensitive to the specific form of the source term. In particular, terms which are in the form of a gradient only generate sound.

As mentioned above, in this section I use the source term derived in Chapter 3. For a gluonic medium at temperature T in the presence of a parton moving with velocity $\mathbf{u} = u\hat{z}$ at position $\mathbf{r} = ut\hat{z}$ in the relativistic limit ($\gamma = (1 - u^2)^{-1/2} \gg 1$), the source is given by

$$J^\nu(x) = (J^0(x), \mathbf{u}J^0(x) - \mathbf{J}_v) \quad (6.15)$$

where

$$J^0(\rho, z, t) = d(\rho, z, t)\gamma u^2 \left(1 - \frac{\gamma u z_-}{\sqrt{z_-^2 \gamma^2 + \rho^2}} \right) \quad (6.16)$$

$$\mathbf{J}_v(\rho, z, t) = (\mathbf{x} - \mathbf{u}t) d(\rho, z, t) \frac{u^4}{\sqrt{z_-^2 \gamma^2 + \rho^2}} \quad (6.17)$$

and

$$d(\rho, z, t) = \frac{\alpha_s (Q_p^a)^2 m_D^2}{8\pi(\rho^2 + \gamma^2 z_-^2)^{3/2}}. \quad (6.18)$$

In the above expressions, $(Q_p^a)^2 = 3$ for a gluon and $4/3$ for a quark, $\rho = (x^2 + y^2)^{1/2}$ is the radius transverse to the z axis, $\alpha_s = g^2/4\pi$ is the strong coupling, $m_D = gT$ and $z_- = (z - ut)$. In what follows any numerical coefficient suppressed by powers of γ^2 will be dropped. For instance, terms such as $\gamma^2 + 1$ will be taken as γ^2 .

The vector part of the source, $\mathbf{J} = \mathbf{u}J^0 - \mathbf{J}_v$, is explicitly

$$\mathbf{J} = \frac{\alpha_s (Q_p^a)^2 m_D^2 u^2}{8\pi} \left(\frac{\gamma \mathbf{u}}{(z_-^2 \gamma^2 + \rho^2)^{3/2}} - \frac{u^2 (x, y, z_- \gamma^2)}{(z_-^2 \gamma^2 + \rho^2)^2} \right) \quad (6.19)$$

which, as one can verify, can be re-written in the form of (6.12),

$$\mathbf{J} = \frac{\alpha_s (Q_p^a)^2 m_D^2 u^2}{8\pi} \left(\frac{\gamma \mathbf{u}}{(z_-^2 \gamma^2 + \rho^2)^{3/2}} + \nabla \frac{u^2}{2(z_-^2 \gamma^2 + \rho^2)} \right). \quad (6.20)$$

6.1.2 Delta Function and Momentum Space Representation

At distances increasingly far from the fast parton, one expects that the source term will begin to look like a delta function. Since hydrodynamics is a long distance effective theory, the hydrodynamic solutions (in the range of validity) should be dominated by the lowest order terms in an expansion of gradients of a delta function centered at the location of the source parton (a detailed discussion of this is given in [47]). Higher order terms in the expansion, which are sensitive to the detailed structure of the source term, will become less important at larger distances. In this section, I will expand the source term, as given by (6.16) and (6.20), up to first order in gradients of a delta function. Later, the hydrodynamic equations, (6.8), (6.10), (6.11), will be solved for both the full source term and the truncated series. A comparison of the solutions will highlight at what distance scales the detailed structure of the source term becomes negligible. It will prove convenient to Fourier transform the source into momentum space, which I will also do in this section, before attempting to solve the hydrodynamic equations. The effect of color screening, which is absent in (6.16) and (6.20), will be modeled by including a damping factor of the form $e^{-\rho m}$, where m^{-1} is a typical screening scale. In a perturbative QGP the inverse screening scale is given by $m_D = gT$, which appears as a coefficient in front of the source term used here. However, in principle, at higher orders the screening scale may be different than what appears as the coefficient of the source term. It is thus instructive to keep m arbitrary; however, in solving the hydrodynamical equations in Sec.6.1.3 I will set $m = gT$. Also, when necessary, a short distance cutoff will be used to regulate ultraviolet divergences. A common choice, which will also be used here, for the short distance cutoff in collisional energy loss is $\rho_{min} = (2\sqrt{E_p T})^{-1}$, where E_p is the energy of the fast parton (see, for instance, [63]).

Consider (6.16), which can be expanded as

$$J^0(\rho, z, t) = C_0 \delta(\mathbf{x}_-) + \mathbf{C}_1 \cdot \nabla \delta(\mathbf{x}_-) + \dots \quad (6.21)$$

where I have used the shorthand notation

$$\delta(\mathbf{x}_-) \equiv \delta(x) \delta(y) \delta(z - ut). \quad (6.22)$$

The coefficients, C_0 and \mathbf{C}_1 , are found by taking the appropriate moment of $J^0(\rho, z, t)$.

Introducing the damping factor, $e^{-\rho m}$, one has for C_0 ,

$$\begin{aligned} C_0 &= \int d^3x J^0(\rho, z, t) e^{-\rho m} \\ &= \int d^3x \frac{\alpha_s (Q_p^a)^2 m_D^2 \gamma u^2}{8\pi (\rho^2 + \gamma^2 z_-^2)^{3/2}} e^{-\rho m} \\ &= \frac{\alpha_s (Q_p^a)^2 m_D^2 u^2}{2} G_0 \left(\frac{m}{2\sqrt{E_p T}} \right), \end{aligned} \quad (6.23)$$

where $(2\sqrt{E_p T})^{-1}$ has been introduced as a short distance cutoff, and G_0 is a representation of the incomplete Gamma function

$$G_0(z) = \int_z^\infty dt \frac{e^{-t}}{t}. \quad (6.24)$$

The coefficient given by (6.23) gives the total energy deposited into the medium per unit time.

Similarly, \mathbf{C}_1 can be obtained as

$$\begin{aligned} \mathbf{C}_1 &= - \int d^3x (x, y, z_-) J^0(\rho, z, t) e^{-\rho m} \\ &= \int d^3x \frac{\alpha_s (Q_p^a)^2 m_D^2 \gamma^2 u^3}{8\pi} \frac{z_-(x, y, z_-)}{(\rho^2 + \gamma^2 z_-^2)^2} e^{-\rho m} \\ &= \frac{\alpha_s (Q_p^a)^2 m_D^2 u^2}{2} \left(0, 0, \frac{\pi u}{4 m \gamma} \right). \end{aligned} \quad (6.25)$$

The results from (6.23) and (6.25), together with (6.21), give

$$J_D^0(\rho, z, t) = \frac{\alpha_s(Q_p^a)^2 m_D^2 u^2}{2} \times \left(G_0 \left(\frac{m}{2\sqrt{E_p T}} \right) + \frac{\pi u}{4 m \gamma} \partial_z \right) \delta(\mathbf{x}_-) + \dots \quad (6.26)$$

where the subscript D is meant to indicate the expansion in gradients of a δ function.

Proceeding in an analogous manner yields for (6.20)

$$\mathbf{J}_D(\rho, z, t) = \frac{\alpha_s(Q_p^a)^2 m_D^2 u^2}{2} \left(\mathbf{u} G_0 \left(\frac{m}{2\sqrt{E_p T}} \right) + \frac{\pi}{8 m \gamma} (u^2 \nabla + \mathbf{u}(\mathbf{u} \cdot \nabla)) \right) \delta(\mathbf{x}_-) + \dots \quad (6.27)$$

Equations (6.26) and (6.27) provide the expansion of the full source, (6.16) and (6.20), up to first order in gradients of a delta function.

As mentioned above, it is easiest to solve for the hydrodynamics in Fourier space. To do this, it is necessary to first transform the source terms into momentum space, following the general rule (6.4). The details of the Fourier transforms of (6.16) and (6.20) are given in Appendix F, and the result is

$$J^0(\mathbf{k}, \omega) = \frac{\alpha_s(Q_p^a)^2 m_D^2 u^2}{2} (2\pi) \delta(\omega - uk_z) \left(G_0 \left(\frac{m + k_T}{2\sqrt{E_p T}} \right) + \frac{i\pi(\mathbf{u} \cdot \mathbf{k})}{4\gamma\sqrt{k_T^2 + m^2}} \right)$$

$$\mathbf{J}(\mathbf{k}, \omega) = \frac{\alpha_s(Q_p^a)^2 m_D^2 u^2}{2} (2\pi) \delta(\omega - uk_z) \times \left(\mathbf{u} G_0 \left(\frac{m + k_T}{2\sqrt{E_p T}} \right) + \frac{i\pi}{4\gamma} \left(\frac{\sqrt{k_T^2 + m^2} - m}{k_T^2} \right) \left(u^2 \mathbf{k} + \frac{\mathbf{u}(\mathbf{u} \cdot \mathbf{k})m}{\sqrt{k_T^2 + m^2}} \right) \right) \quad (6.28)$$

The above should be compared to the Fourier transforms of (6.26) and (6.27), which

are found by making the replacements $\delta(z_-) \rightarrow (2\pi)\delta(\omega - uk_z)$ and $\nabla \rightarrow i\mathbf{k}$:

$$\begin{aligned}
J_D^0(\mathbf{k}, \omega) &= \frac{\alpha_s(Q_p^a)^2 m_D^2 u^2}{2} (2\pi)\delta(\omega - uk_z) \left(G_0 \left(\frac{m}{2\sqrt{E_p T}} \right) + \frac{i\pi(\mathbf{u} \cdot \mathbf{k})}{4m\gamma} \right) \\
\mathbf{J}_D(\mathbf{k}, \omega) &= \frac{\alpha_s(Q_p^a)^2 m_D^2 u^2}{2} (2\pi)\delta(\omega - uk_z) \left(\mathbf{u} G_0 \left(\frac{m}{2\sqrt{E_p T}} \right) + \frac{i\pi}{8m\gamma} (u^2 \mathbf{k} + \mathbf{u} \omega) \right)
\end{aligned} \tag{6.29}$$

One can verify that (6.28) reduces to (6.29) by taking the $k_T \rightarrow 0$ limit in the coefficients of 1 and \mathbf{k} . (6.28) and (6.29) will be used in the next section to solve for the hydrodynamic variables of the medium.

As discussed at the beginning of the section, at distances increasingly far from the fast parton the source term is dominated by the lowest order terms in an expansion of gradients of a delta function. It's clear from inspection that the detailed structure of the full source term, given by (6.28), becomes important at a momentum scale $k \sim m$. This could have been anticipated, since the full source term is calculated up to distances of the order of the screening length. A quantitative comparison of the effects of (6.28) and (6.29) requires solving the hydrodynamic equations. This will be done in the next section.

6.1.3 Solving the Equations

The result given by (6.28) is combined with equations (6.8), (6.10), and (6.11) to yield $\delta\epsilon(\mathbf{k}, \omega)$, $\mathbf{g}_L(\mathbf{k}, \omega)$ and $\mathbf{g}_T(\mathbf{k}, \omega)$. These are then transformed back to position space using the relation (6.4). In $\delta\epsilon(\mathbf{k}, \omega)$ and $\mathbf{g}_L(\mathbf{k}, \omega)$, one can find J_L by taking

$\hat{\mathbf{k}} \cdot \mathbf{J}$, which is written conveniently as

$$\begin{aligned}
J_L &= \frac{\alpha_s(Q_p^a)^2 m_D^2 u^2}{2k} (2\pi) \delta(\omega - uk_z) \left((\mathbf{u} \cdot \mathbf{k}) \left(G_0 \left(\frac{m_D + k_T}{2\sqrt{E_p T}} \right) + \right. \right. \\
&\quad \left. \left. \frac{i\pi(\mathbf{u} \cdot \mathbf{k})}{4\gamma\sqrt{k_T^2 + m_D^2}} \right) + \frac{i\pi u^2}{4\gamma} \left(\sqrt{k_T^2 + m_D^2} - m_D \right) \right) \\
&= \frac{(\mathbf{u} \cdot \mathbf{k}) J^0}{k} + \frac{\alpha_s(Q_p^a)^2 m_D^2 u^2}{2k} (2\pi) \delta(\omega - uk_z) \frac{i\pi u^2}{4\gamma} \left(\sqrt{k_T^2 + m_D^2} - m_D \right)
\end{aligned} \tag{6.30}$$

where I am now taking $m = m_D$. After integrating out $\delta(\omega - uk_z)$ and using (F-5), the expression for $\delta\epsilon(\mathbf{x}, t)$ is given by

$$\begin{aligned}
\delta\epsilon(\mathbf{x}, t) &= \frac{\alpha_s(Q_p^a)^2 m_D^2 u^2 \lambda^2}{8\pi^2 c_s^2} \int dk_T dk_z \frac{k_T J_0(\rho k_T) e^{ik_z(z-ut)}}{k_z^2 - \lambda^2 k_T^2 + i\sigma} \times \\
&\quad \left(\left(G_0 \left(\frac{m_D + k_T}{2\sqrt{E_p T}} \right) + \frac{i\pi u k_z}{4\gamma\sqrt{k_T^2 + m_D^2}} \right) (2iuk_z - \Gamma_s k^2) - \frac{\pi u^2}{4\gamma} \left(\sqrt{k_T^2 + m_D^2} - m_D \right) \right)
\end{aligned} \tag{6.31}$$

where $\lambda^2 = c_s^2/(u^2 - c_s^2)$, $\sigma = \Gamma_s u (\lambda^2/c_s^2) k_z (k_T^2 + k_z^2)$ and I am again working in plane polar coordinates. The integral over k_z can be performed using contour integration. Poles are located at $k_z = \pm(k_T^2 \lambda^2 \mp i|\sigma|)^{1/2}$, where $|\sigma|$ is itself a function of k_z . When evaluating the residues at these poles I make the approximation $\sigma(k_z) \approx \sigma(\pm k_T \lambda)$. This approximation is valid at momentum scales for which the sound attenuation is small ($k_T \ll c_s^2/\Gamma_s$), which should be reasonable in the hydrodynamic limit. Both poles are located in the lower complex plane so that the integration only contributes

for $z < ut$, i. e., behind the source parton. Performing the integration yields

$$\begin{aligned}
\delta\epsilon(\mathbf{x}, t) &= \frac{\alpha_s(Q_p^a)^2 m_D^2 u^2 \lambda^2}{4\pi c_s^2} \text{Re} \left[\int dk_T \frac{iJ_0(\rho k_T) e^{ik_T \sqrt{\lambda^2 - ik_T \alpha}(z-ut)}}{\sqrt{\lambda^2 - ik_T \alpha}} \right. \\
&\times \left(\frac{\pi u^2}{4\gamma} \left(\sqrt{k_T^2 + m_D^2} - m_D \right) - \left(G_0 \left(\frac{m_D + k_T}{2\sqrt{E_p T}} \right) + \frac{i\pi u k_T \sqrt{\lambda^2 - ik_T \alpha}}{4\gamma \sqrt{k_T^2 + m_D^2}} \right) \right. \\
&\times \left. \left. \left(2iuk_T \sqrt{\lambda^2 - ik_T \alpha} - \Gamma_s k_T^2 (1 + \lambda^2 - ik_T \alpha) \right) \right) \right] \tag{6.32}
\end{aligned}$$

where $\alpha \equiv \Gamma_s u \lambda^3 / (c_s^2 (\lambda^2 + 1))$. The final integration over k_T is performed numerically.

The analogous expression resulting from (6.29) is given by

$$\begin{aligned}
\delta\epsilon_D(\mathbf{x}, t) &= \frac{\alpha_s(Q_p^a)^2 m_D^2 u^2 \lambda^2}{4\pi c_s^2} \text{Re} \left[\int dk_T \frac{iJ_0(\rho k_T) e^{ik_T \sqrt{\lambda^2 - ik_T \alpha}(z-ut)}}{\sqrt{\lambda^2 - ik_T \alpha}} \right. \\
&\times \left(\frac{\pi u^2 k_T^2}{8\gamma m_D} - \left(G_0 \left(\frac{m_D}{2\sqrt{E_p T}} \right) + \frac{i\pi u k_T \sqrt{\lambda^2 - ik_T \alpha}}{4\gamma m_D} \right) \right. \\
&\times \left. \left. \left(2iuk_T \sqrt{\lambda^2 - ik_T \alpha} - \Gamma_s k_T^2 (1 + \lambda^2 - ik_T \alpha) \right) \right) \right] \tag{6.33}
\end{aligned}$$

The same approach is applied to $\mathbf{g}_L(\mathbf{x}, t)$. The contour integration proceeds in the same manner as in (6.31) with the exception that one term has additional poles at $k_z = \pm ik_T$. The additional pole at $k_z = ik_T$ allows for some contribution in the

region in front of the source parton. The result is

for $z < ut$:

$$\begin{aligned}
\mathbf{g}_L(\mathbf{x}, t) &= \frac{\alpha_s(Q_p^a)^2 m_D^2 u^2 \lambda^2}{4\pi c_s^2} \text{Re} \left[\int dk_T \frac{k_T e^{ik_T \sqrt{\lambda^2 - ik_T \alpha}(z-ut)}}{\sqrt{\lambda^2 - ik_T \alpha}} \right. \\
&\times \left(\frac{x}{\rho} i J_1(\rho k_T), \frac{y}{\rho} i J_1(\rho k_T), \sqrt{\lambda^2 - ik_T \alpha} J_0(\rho k_T) \right) \\
&\times \left(G_0 \left(\frac{m_D + k_T}{2\sqrt{E_p T}} \right) \left(\frac{u^2(\lambda^2 - ik_T \alpha)}{(1 + \lambda^2 - ik_T \alpha)} + c_s^2 \right) + \right. \\
&\left. \frac{i\pi u k_T \sqrt{\lambda^2 - ik_T \alpha}}{4\gamma \sqrt{k_T^2 + m_D^2}} \left((u^2 + c_s^2) + \frac{u^2 m_D (m_D - \sqrt{k_T^2 + m_D^2})}{k_T^2 (1 + \lambda^2 - ik_T \alpha)} \right) \right) \left. \right] \\
&+ \frac{\alpha_s(Q_p^a)^2 m_D^2 u^2}{8\pi} \int dk_T e^{-k_T |z-ut|} \left(-\frac{x}{\rho} J_1(\rho k_T), -\frac{y}{\rho} J_1(\rho k_T), J_0(\rho k_T) \right) \\
&\times \left(k_T G_0 \left(\frac{m_D + k_T}{2\sqrt{E_p T}} \right) + \frac{\pi m_D}{4\gamma} \left(1 - \frac{m_D}{\sqrt{k_T^2 + m_D^2}} \right) \right)
\end{aligned} \tag{6.34}$$

for $z > ut$:

$$\begin{aligned}
\mathbf{g}_L(\mathbf{x}, t) &= -\frac{\alpha_s(Q_p^a)^2 m_D^2 u^2}{8\pi} \int dk_T e^{-k_T |z-ut|} \left(\frac{x}{\rho} J_1(\rho k_T), \frac{y}{\rho} J_1(\rho k_T), J_0(\rho k_T) \right) \\
&\times \left(k_T G_0 \left(\frac{m_D + k_T}{2\sqrt{E_p T}} \right) - \frac{\pi m_D}{4\gamma} \left(1 - \frac{m_D}{\sqrt{k_T^2 + m_D^2}} \right) \right).
\end{aligned}$$

which must be done numerically. The analogous expression resulting from (6.29) is

given by

for $z < ut$:

$$\begin{aligned}
\mathbf{g}_{LD}(\mathbf{x}, t) &= \frac{\alpha_s(Q_p^a)^2 m_D^2 u^2 \lambda^2}{4\pi c_s^2} \text{Re} \left[\int dk_T \frac{k_T e^{ik_T \sqrt{\lambda^2 - ik_T \alpha}(z-ut)}}{\sqrt{\lambda^2 - ik_T \alpha}} \right. \\
&\times \left(\frac{x}{\rho} i J_1(\rho k_T), \frac{y}{\rho} i J_1(\rho k_T), \sqrt{\lambda^2 - ik_T \alpha} J_0(\rho k_T) \right) \\
&\left(G_0 \left(\frac{m_D}{2\sqrt{E_p T}} \right) \left(\frac{u^2(\lambda^2 - ik_T \alpha)}{(1 + \lambda^2 - ik_T \alpha)} + c_s^2 \right) + \right. \\
&\left. \left. \frac{i\pi u k_T \sqrt{\lambda^2 - ik_T \alpha}}{4\gamma m_D} \left((u^2 + c_s^2) + \frac{u^2}{2(1 + \lambda^2 - ik_T \alpha)} \right) \right) \right] \\
&+ \frac{\alpha_s(Q_p^a)^2 m_D^2 u^2}{8\pi} \int dk_T e^{-k_T |z-ut|} \left(-\frac{x}{\rho} J_1(\rho k_T), -\frac{y}{\rho} J_1(\rho k_T), J_0(\rho k_T) \right) \\
&\times \left(k_T G_0 \left(\frac{m_D}{2\sqrt{E_p T}} \right) + \frac{\pi k_T^2}{8\gamma m_D} \right)
\end{aligned}$$

for $z > ut$:

$$\begin{aligned}
\mathbf{g}_{LD}(\mathbf{x}, t) &= -\frac{\alpha_s(Q_p^a)^2 m_D^2 u^2}{8\pi} \int dk_T e^{-k_T |z-ut|} \left(\frac{x}{\rho} J_1(\rho k_T), \frac{y}{\rho} J_1(\rho k_T), J_0(\rho k_T) \right) \\
&\times \left(k_T G_0 \left(\frac{m_D}{2\sqrt{E_p T}} \right) - \frac{\pi k_T^2}{8\gamma m_D} \right).
\end{aligned} \tag{6.35}$$

Combining (6.14) with (6.11) and following the same approach used above allows for the determination of $\mathbf{g}_T(\mathbf{x}, t)$. The denominator of (6.11) has a simpler structure than in (6.8,6.10) which allows the contour integration to be performed exactly.

Defining $\Omega \equiv 4u/3\Gamma_s$ it is found that

$$\begin{aligned}
\mathbf{g}_T(\mathbf{x}, t) &= \frac{\alpha_s(Q_p^a)^2 m_D^2}{4\pi} \int dk_T \frac{k_T^2 e^{\pm\Delta^\mp |z-ut|}}{(k_T^2 - (\Delta^\mp)^2) \sqrt{1 + \frac{4k_T^2}{\Omega^2}}} \\
&\times \left(J_1(\rho k_T) \frac{x}{\rho} \Delta^\mp, J_1(\rho k_T) \frac{y}{\rho} \Delta^\mp, J_0(\rho k_T) k_T \right) \\
&\times \left(G_0 \left(\frac{m_D + k_T}{2\sqrt{E_p T}} \right) - \frac{\pi m_D \Delta^\mp}{4\gamma} \left(\frac{\sqrt{k_T^2 + m_D^2} - m_D}{k_T \sqrt{k_T^2 + m_D^2}} \right) \right) \\
&\pm \frac{\alpha_s(Q_p^a)^2 m_D^2}{16u\pi} \int dk_T e^{-k_T |z-ut|} \left(\pm J_1(\rho k_T) \frac{x}{\rho} k_T, \pm J_1(\rho k_T) \frac{y}{\rho} k_T, -J_0(\rho k_T) k_T \right) \\
&\times \left(G_0 \left(\frac{m_D + k_T}{2\sqrt{E_p T}} \right) \mp \frac{\pi m_D k_T}{4\gamma} \left(\frac{\sqrt{k_T^2 + m_D^2} - m_D}{k_T \sqrt{k_T^2 + m_D^2}} \right) \right)
\end{aligned} \tag{6.36}$$

where \mp refers to the sign of $(z - ut)$ and

$$\Delta^\mp \equiv \frac{\Omega}{2} \left(1 \mp \sqrt{1 + \frac{4k_T^2}{\Omega^2}} \right). \tag{6.37}$$

The analogous result from (6.29) is given by

$$\begin{aligned}
\mathbf{g}_{TD}(\mathbf{x}, t) &= \frac{\alpha_s(Q_p^a)^2 m_D^2}{4\pi} \int dk_T \frac{k_T^2 e^{\pm\Delta^\mp |z-ut|}}{(k_T^2 - (\Delta^\mp)^2) \sqrt{1 + \frac{4k_T^2}{\Omega^2}}} \times \\
&\left(G_0 \left(\frac{m_D}{2\sqrt{E_p T}} \right) - \frac{\pi \Delta^\mp}{8\gamma m_D} \right) \left(J_1(\rho k_T) \frac{x}{\rho} \Delta^\mp, J_1(\rho k_T) \frac{y}{\rho} \Delta^\mp, J_0(\rho k_T) k_T \right) \\
&\pm \frac{\alpha_s(Q_p^a)^2 m_D^2}{16u\pi} \int dk_T e^{-k_T |z-ut|} \left(\pm J_1(\rho k_T) \frac{x}{\rho} k_T, \pm J_1(\rho k_T) \frac{y}{\rho} k_T, -J_0(\rho k_T) k_T \right) \\
&\times \left(G_0 \left(\frac{m_D}{2\sqrt{E_p T}} \right) \mp \frac{\pi k_T}{8\gamma m_D} \right).
\end{aligned} \tag{6.38}$$

In this section, I have presented in detail a method of solution for the linearized hydrodynamical equations of a QGP coupled to the source term generated by a fast

parton. The numerical results are presented in Sec. 6.3.1 below. In the next section, I solve the linearized hydrodynamical equations coupled to the source term derived in Chapter 4.

6.2 Source Term with Radiation

Recall the source term derived in Chapter 4, which included both the radiative and collisional energy losses. For the case of back to back fast partons created in an initial hard interaction at time $t = 0$, which then propagate for some time, t_M , before being absorbed by the medium, it is given by

$$J^\nu(x) = \frac{dE}{dt} (\Theta(t) - \Theta(t - t_M)) \times [\delta(\mathbf{x} - \mathbf{u}t) (1, \mathbf{u}) + \delta(\mathbf{x} + \mathbf{u}t) (1, -\mathbf{u})] \quad (6.39)$$

where $\Theta(t)$ is 1 if $t > 0$ and zero otherwise, and

$$\frac{dE}{dt} = \frac{\alpha_s C_2 m_D^2}{2} \ln \frac{2\sqrt{E_p T}}{m_D} + 0.474 \frac{\text{GeV}}{\text{fm}} + 0.51 t \frac{\text{GeV}}{\text{fm}^2}. \quad (6.40)$$

I am here interested in coupling this source to the linearized hydrodynamic equations presented in the previous section, which are written in momentum space as

$$\delta\epsilon(\mathbf{k}, \omega) = \frac{ikJ_L(\mathbf{k}, \omega) + J^0(\mathbf{k}, \omega)(i\omega - \Gamma_s k^2)}{\omega^2 - c_s^2 k^2 + i\Gamma_s \omega k^2}, \quad (6.41)$$

$$\mathbf{g}_L(\mathbf{k}, \omega) = \frac{i\omega \hat{k} J_L(\mathbf{k}, \omega) + ic_s^2 \mathbf{k} J^0(\mathbf{k}, \omega)}{\omega^2 - c_s^2 k^2 + i\Gamma_s \omega k^2}, \quad (6.42)$$

$$\mathbf{g}_T(\mathbf{k}, \omega) = \frac{i\mathbf{J}_T(\mathbf{k}, \omega)}{\omega + \frac{3}{4}i\Gamma_s k^2} \quad (6.43)$$

In order to proceed, it is necessary to obtain the Fourier transform of (6.39), as well as the decomposition of the source vector into longitudinal and transverse parts.

The spatial Fourier transform proceeds in a simple manner to give

$$\begin{aligned} J^\nu(\mathbf{k}, t) &= \int d^3\mathbf{x} e^{-i\mathbf{k}\cdot\mathbf{x}} J^\nu(x) \\ &= \frac{dE}{dt}(\Theta(t) - \Theta(t - t_M)) \times [e^{-itk_z} (1, \mathbf{u}) + e^{itk_z} (1, -\mathbf{u})] \end{aligned} \quad (6.44)$$

where $\mathbf{u} = \hat{z}$. At this point I decompose the vector part of the source and find

$$J_L(\mathbf{k}, t) = \frac{k_z}{k} \frac{dE}{dt}(\Theta(t) - \Theta(t - t_M)) (e^{-itk_z} - e^{itk_z}) \quad (6.45)$$

$$\mathbf{J}_T(\mathbf{k}, t) = \left(\mathbf{u} - \mathbf{k} \frac{k_z}{k^2} \right) \frac{dE}{dt}(\Theta(t) - \Theta(t - t_M)) (e^{-itk_z} - e^{itk_z}). \quad (6.46)$$

And similarly,

$$J^0 = \frac{dE}{dt}(\Theta(t) - \Theta(t - t_M)) (e^{-itk_z} + e^{itk_z}). \quad (6.47)$$

In order to take the time Fourier transform, it is helpful to introduce a small exponential damping factor, γ , into the above expressions, which will be set to zero before any terms are evaluated. dE/dt has a term which is constant in time and one which grows linearly in time, which I write as

$$\frac{dE}{dt} = \Delta E_0 + t \Delta E_1. \quad (6.48)$$

Using this notation, the relevant time Fourier transforms are

$$\begin{aligned} &\int dt \frac{dE}{dt}(\Theta(t) - \Theta(t - t_M)) (e^{-it(k_z - \omega - i\gamma)}) \\ &= (\Delta E_0 - \Delta E_1 \frac{\partial}{\partial \gamma}) \left(\frac{i(1 - e^{-t_M(ik_z + \gamma - i\omega)})}{\omega - k_z + i\gamma} \right) \end{aligned} \quad (6.49)$$

and

$$\begin{aligned} &\int dt \frac{dE}{dt}(\Theta(t) - \Theta(t - t_M)) (e^{it(k_z + \omega + i\gamma)}) \\ &= (\Delta E_0 - \Delta E_1 \frac{\partial}{\partial \gamma}) \left(\frac{i(1 - e^{t_M(ik_z - \gamma + i\omega)})}{\omega + k_z + i\gamma} \right). \end{aligned} \quad (6.50)$$

The expression for $\delta\epsilon$ takes the form

$$\begin{aligned}
\epsilon(x, t) &= \int \frac{d^4k}{(2\pi)^4} e^{i\mathbf{k}\cdot\mathbf{x}-i\omega t} \epsilon(\mathbf{k}, \omega) \\
&= i\hat{O} \int \frac{d^4k}{(2\pi)^4} e^{i\mathbf{k}\cdot\mathbf{x}-i\omega t} \times \\
&\quad \frac{(ik_z + i\omega - \Gamma_s k^2)(1 - e^{-tM(ik_z + \gamma - i\omega)})}{(\omega^2 - c_s^2 k^2 + i\Gamma_s \omega k^2)(\omega - k_z + i\gamma)} + \frac{(-ik_z + i\omega - \Gamma_s k^2)(1 - e^{tM(ik_z - \gamma + i\omega)})}{(\omega^2 - c_s^2 k^2 + i\Gamma_s \omega k^2)(\omega + k_z + i\gamma)}
\end{aligned} \tag{6.51}$$

where $\hat{O} = \Delta E_0 - \Delta E_1 \partial/\partial\gamma$. The details of the explicit evaluation of (6.51) are contained in Appendix G. Similarly, one has

$$\begin{aligned}
\mathbf{g}_L(x, t) &= i\hat{O} \int \frac{d^4k}{(2\pi)^4} e^{i\mathbf{k}\cdot\mathbf{x}-i\omega t} \frac{\mathbf{k}}{k^2} \times \\
&\quad \frac{(i\omega k_z + ic_s^2 k^2)(1 - e^{-T(ik_z + \gamma - i\omega)})}{(\omega^2 - c_s^2 k^2 + i\Gamma_s \omega k^2)(\omega - k_z + i\gamma)} + \frac{(-i\omega k_z + ic_s^2 k^2)(1 - e^{T(ik_z - \gamma + i\omega)})}{(\omega^2 - c_s^2 k^2 + i\Gamma_s \omega k^2)(\omega + k_z + i\gamma)}
\end{aligned} \tag{6.52}$$

and

$$\begin{aligned}
\mathbf{g}_T(x, t) &= i\hat{O} \int \frac{d^4k}{(2\pi)^4} e^{i\mathbf{k}\cdot\mathbf{x}-i\omega t} \frac{(-k_x k_z, -k_y k_z, k_T^2)}{k^2} \times \\
&\quad \frac{i(1 - e^{-T(ik_z + \gamma - i\omega)})}{(\omega + \frac{3}{4}i\Gamma_s k^2)(\omega - k_z + i\gamma)} + \frac{-i(1 - e^{T(ik_z - \gamma + i\omega)})}{(\omega + \frac{3}{4}i\Gamma_s k^2)(\omega + k_z + i\gamma)}.
\end{aligned} \tag{6.53}$$

The explicit evaluation of (6.52) and (6.53) are given in Appendix G. In Sec. 6.3.2 the numerical results of integrating the above expressions are presented. In that case, I will consider back to back quarks created at a time of $t = 0$ which then propagate until $t = 6$ fm before being absorbed by the medium. A time interval of 6 fm for a quark propagating in the medium is consistent with what may be expected in a heavy-ion collision.

6.3 Numerical Results

The technical details necessary to derive relevant quantities of the medium response in linearized hydrodynamics were presented in the previous two sections. The numerical results of integration are presented below.

6.3.1 Kinetic Theory Source Term

In Sec. 6.1 I obtained expressions for the hydrodynamic quantities $\delta\epsilon(\mathbf{x}, t)$, $\mathbf{g}_L(\mathbf{x}, t)$ and $\mathbf{g}_T(\mathbf{x}, t)$ for a medium coupled to the source derived in Chapter 3. I now consider the results of numerical integration. All calculations are performed for a gluon moving along the positive z axis at position ut and speed $u = 0.99955c$ ($\gamma \approx 33$). The strong coupling, α_s , is chosen to be $1/\pi$, the temperature is taken to be $T = 350$ MeV, and $E_p = 16$ GeV. As mentioned above, I will compare the solutions resulting from the the full source term and the delta function expanded source term, given by (6.28) and (6.29), respectively. I will also make a comparison of the results for a range of values of the shear viscosity to entropy density ratio, η/s , and speed of sound, c_s .

The solutions resulting from the the full source term and the delta function source are shown in Figures 6.1 and 6.2. In both Figures the results are plotted for $\eta/s = 1/4\pi$ and $c_s = c/\sqrt{3}$. Figure 6.1(a) shows a contour plot of $\delta\epsilon(\mathbf{x}, t)$ for each source. In both cases a well define Mach cone is visible in the trailing medium. Figure 6.1(b) shows the result for the magnitude of the momentum density, $|\mathbf{g}| = |\mathbf{g}_L(\mathbf{x}, t) + \mathbf{g}_T(\mathbf{x}, t)|$. One now sees both a sound contribution from $\mathbf{g}_L(\mathbf{x}, t)$, which excites a Mach cone, and a diffusive contribution from $\mathbf{g}_T(\mathbf{x}, t)$, which is excited in the region directly behind the source gluon. The diffusive momentum density produces flow almost exclusively in the direction of the source parton's velocity, while the Mach cone generates flow outward and perpendicular to it's boundary,

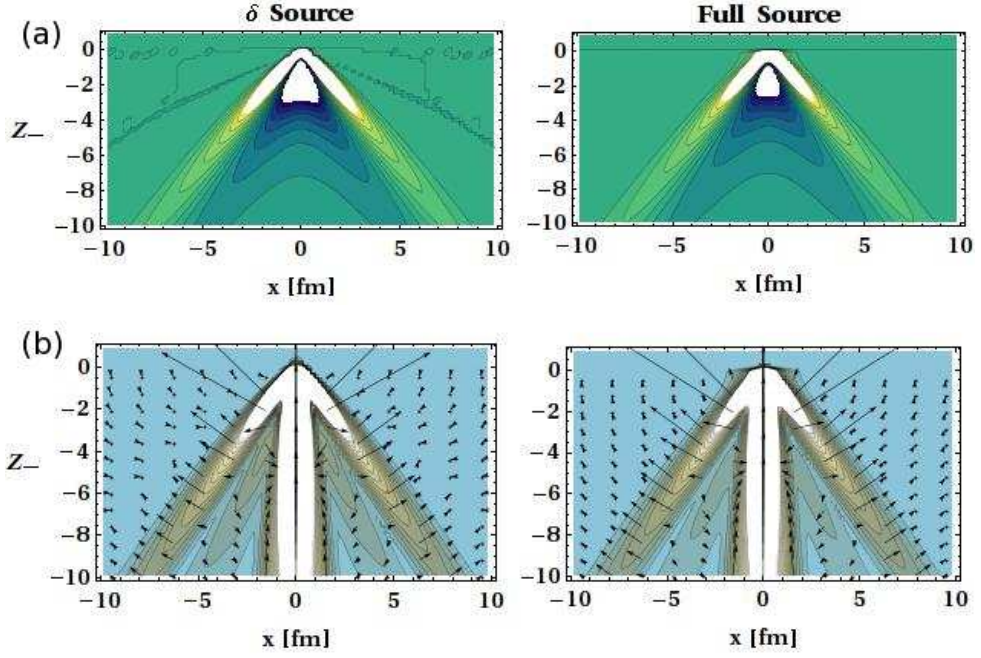


FIGURE 6.1: Plots of (a): the perturbed energy density, and (b): the perturbed momentum density, for both the full source term and the δ function expanded source term. Here, $\eta/s = 1/4\pi$ and $c_s = 0.57$. The direction of the momentum density is indicated by the arrows.

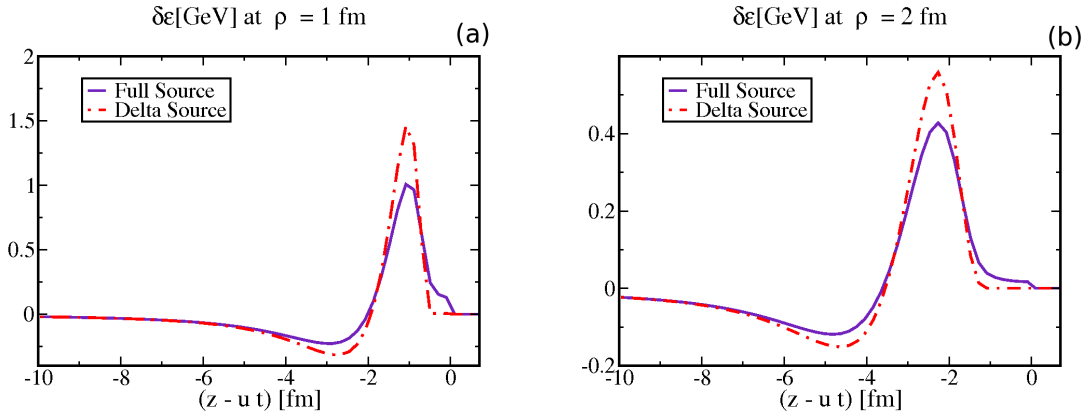


FIGURE 6.2: A comparison of the perturbed energy density generated by the full source term and the δ function expanded source term for two different values of ρ . The two results converge at a distance of about 5-6 fm behind the source parton for the chosen values of ρ .

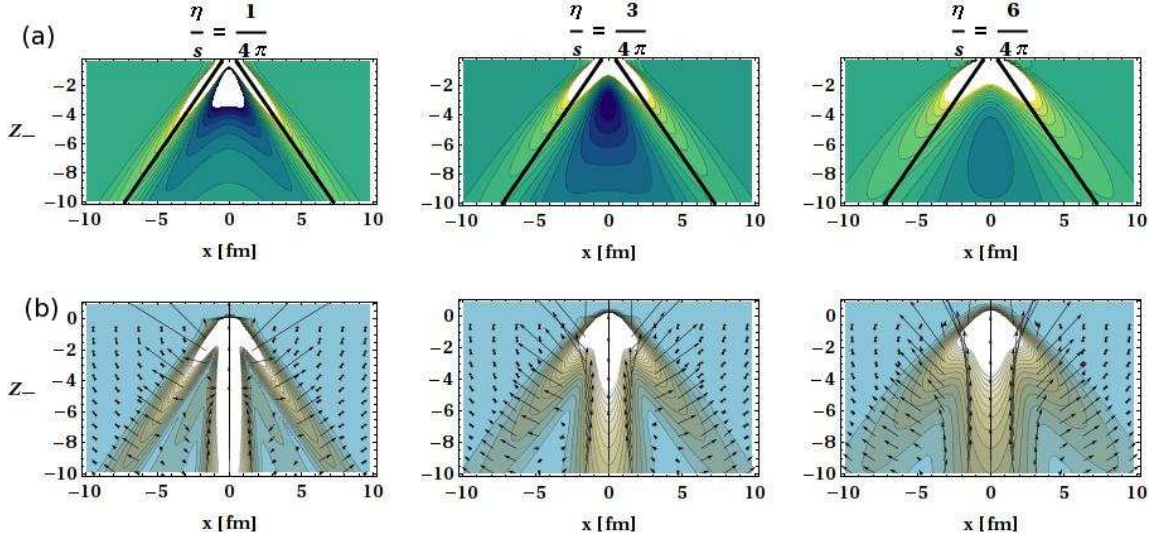


FIGURE 6.3: Plots of (a): the perturbed energy density, and (b): the perturbed momentum density for different values of the shear viscosity to entropy density ratio, η/s . The black lines in (a) are drawn where one would expect to find the boundary of a Mach cone in the absence of dissipative effects. Plots scaled by the radius, ρ , which factor in the conical broadening of the cone, are shown in Figure 6.4.

as indicated by the arrows. One can see from Figure 6.1 that the full source term and the delta function expanded source term provide qualitatively similar results, particularly in the region far from the source parton. In the region near $z_- = 0$, the full source solution has a noticeably larger transverse extent than the corresponding delta source result. A more quantitative comparison can be made by examining Figure 6.2 where $\delta\epsilon(\mathbf{x}, t)$ is plotted as a function of z_- for fixed ρ . Here one sees that the two results converge at a distance of about 5-6 fm behind the source parton for the chosen ρ values.

Results are next presented for three different values of the shear viscosity to entropy density ratio, η/s . The first value chosen for η/s is $1/4\pi \approx 0.08$, which has been proposed [21] as a universal lower bound for all relativistic quantum field theories and is calculated in the strongly coupled limit. The other two values for η/s are multiples of the previous value, $3/4\pi$ and $6/4\pi$, and are more consistent with the application of perturbation theory, which is the method used to calculate the source

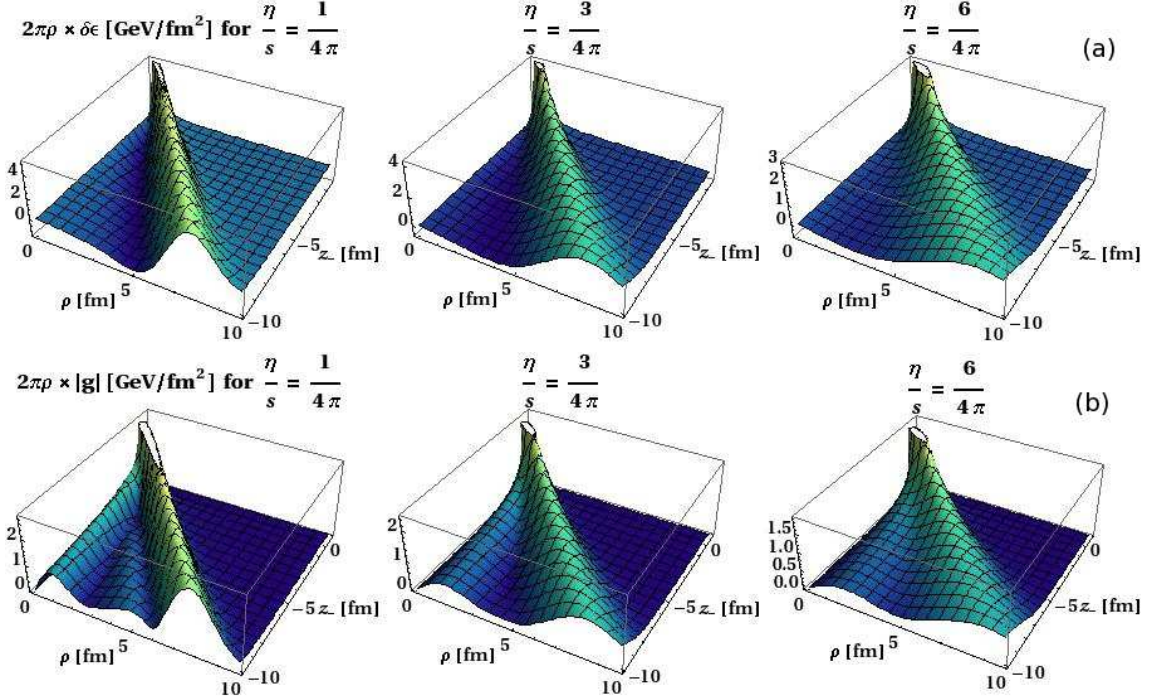


FIGURE 6.4: Plots of (a): the total perturbed energy density, and (b): the total perturbed momentum density, contained at a given radius in the $\rho - z_-$ plane for different values of η/s . As one can see in (b) the total perturbed momentum density carried by the sonic Mach cone exceeds that contained in the diffusive wake.

used in this paper. For example, Arnold *et al.* [73] found for the leading order result $\eta/s = 0.48$ for a gluonic plasma with $\alpha_s = 0.3$. More recently, Xu and Greiner found $\eta/s = 0.13$ for a gluonic plasma with the same value of α_s by going beyond leading order in the diluteness of the medium [74]. A small value of the shear viscosity, which is required by the RHIC data [75], is not necessarily incompatible with perturbation theory, especially if the viscosity is lowered by anomalous contributions [76].

The results for $\delta\epsilon(\mathbf{x}, t)$ and $|\mathbf{g}| = |\mathbf{g}_L(\mathbf{x}, t) + \mathbf{g}_T(\mathbf{x}, t)|$ for all three viscosities are shown in Figures 6.3 and 6.4, where $c_s = c/\sqrt{3}$. The black lines in the contour plots of Figure 6.3(a) are drawn along the slope $x = \pm\lambda(z - ut)$ which is where one would expect to find the boundary of a Mach cone in the absence of dissipative effects. In Figure 6.4, the total energy density (figure (a)), and magnitude of momentum

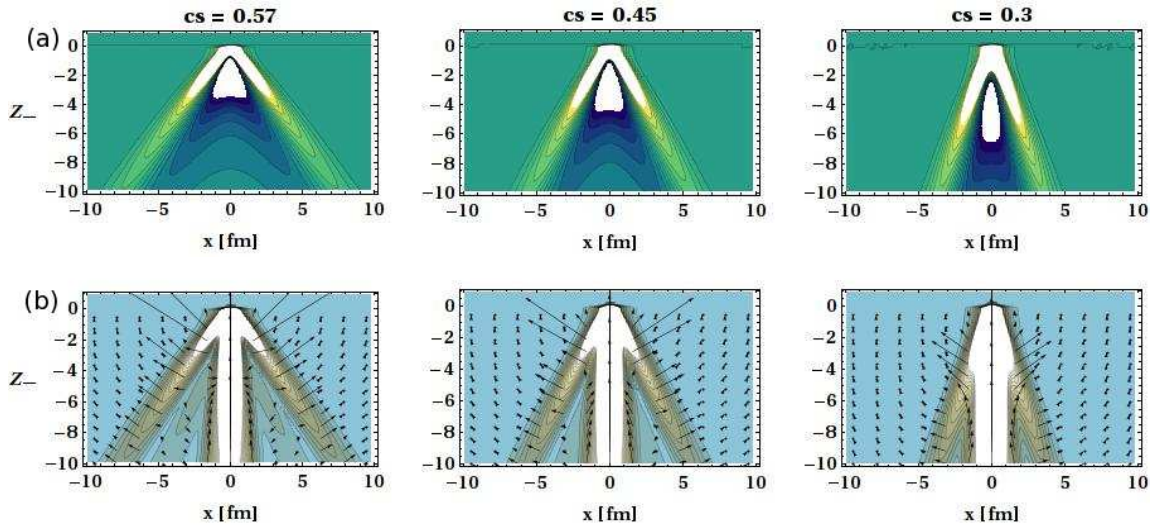


FIGURE 6.5: Plots of (a): the perturbed energy density, and (b): the perturbed momentum density for different values of the speed of sound, c_s . Plots scaled by the radius, ρ , which factor in the conical broadening of the cone, are shown in Figure 6.6.

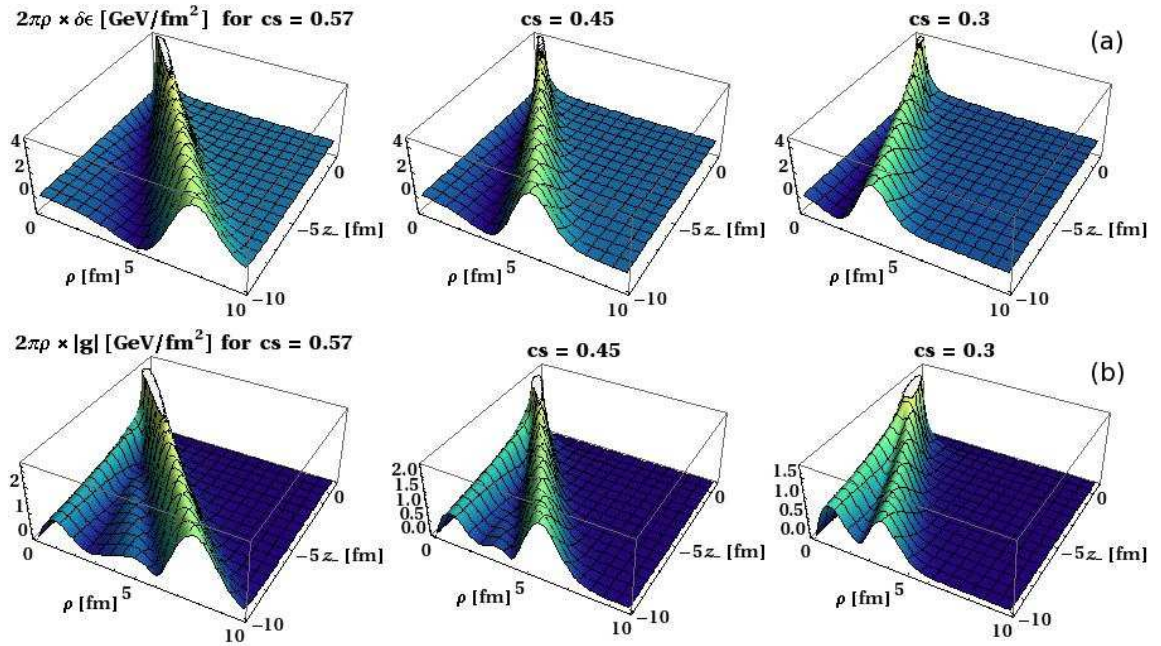


FIGURE 6.6: Plots of (a): the total perturbed energy density, and (b): the total perturbed momentum density, contained at a given radius in the $\rho - z_-$ plane for different values of c_s . The magnitude of the Mach cone, when integrated, is similar for the different plots.

density (figure (b)), contained at a given radius are shown. It is clear from the plots that the Mach cone broadens and weakens as the viscosity is increased.

Finally, results are shown for three different values of the speed of sound, c_s . The first value is $c_s = 0.57$, which is the limiting value for a conformal ideal relativistic gas, while the other two values are $c_s = 0.45, 0.3$. It's likely that the QGP produced at RHIC experiences a speed of sound close to all three of these values during its evolution [11]. The results are shown in Figures 6.5 and 6.6, where I have chosen $\eta/s = 1/4\pi$. One should note that the diffusive contribution, $\mathbf{g}_T(\mathbf{x}, t)$, is independent of the speed of sound.

The solution has been examined for different values of the shear viscosity to entropy density ratio and speed of sound. Additionally, the relevance of finite source structure has been investigated by performing an expansion in gradients of a delta function centered at the location of the source parton. Comparison of the medium response generated by the full source with that generated by the delta expanded one shows that the result is sensitive to the finite structure up to distances of several fm from the fast parton for the source examined here. In the next section I consider the numerical evaluation of the expressions derived in Sec. 6.2.

6.3.2 Radiative and Collisional Source Term

In Sec. 6.2 expressions for the hydrodynamic quantities $\delta\epsilon(\mathbf{x}, t)$, $\mathbf{g}_L(\mathbf{x}, t)$ and $\mathbf{g}_T(\mathbf{x}, t)$ were derived for a medium coupled to the source derived in Chapter 4. I now consider the numerical results from those calculations. I consider two quarks created at a time $t = 0$ which propagate back-to-back along the z axis until $t = 6$ fm, at which time they are assumed to be absorbed by the medium. The medium response is plotted below at times $t = 2, 4, 6, 8, 10,$ and 12 fm. The strong coupling, α_s , is chosen to be $1/\pi$, the temperature is taken to be $T = 350$ MeV, and $E_p = 50$ GeV. Additionally, $\eta/s = 0.2$ and $c_s = 0.57$.

On a technical note, it's necessary to point out that the expressions derived in Sec. 6.2 are only valid for times after the source is set to zero. To plot the medium response at $t = 2$, and 4 fm, it is necessary to set the source to zero and then do the calculation. So, for example, in the plots at $t = 4$ fm, the source is assumed to be zero at times greater than $t = 3.5$ fm, and similarly, in the plots at $t = 2$ fm, the source is assumed to be zero at times greater than $t = 1.5$ fm. In this way, one gets a good idea of what the solution looks like at the plotted time, even though there is a small delay resulting from the limitations of the expressions given in Sec. 6.2.

The results for $\delta\epsilon(\mathbf{x}, t)$ are shown in Figure 6.7. The plots are shown in the x - z plane, however, the results are cylindrically symmetric about the \hat{z} axis. One is able to get a sense of the time evolution of the medium response as the quarks propagate away from each other. The Mach cone formation is visible, particularly at later times. The radiative induced excitation leads to a t growth in the source strength, which manifests itself in the sharp rise of the induced wave at early times.

The results for $|g(\mathbf{x}, t)|$ are shown in Figure 6.8. These plots are also shown in the x - z plane, but the results are cylindrically symmetric about the \hat{z} axis. In this case, there is both a sound wave (from \mathbf{g}_L) and a diffusive wake (from \mathbf{g}_T). It is interesting to note in the plot shown at $t = 10$ fm, which is 4 fm after the source is absorbed by the medium, that the sound wave has separated from the diffusive wake to a large extent. This results because the sound wave propagates in the medium, whereas the diffusive wake is deposited locally. Once the source is turned off, the sound wave continues to propagate, but the diffusive part does not. This is directly relevant to the di-hadron correlation measurements discussed in Chapter 1. Recall that the double peak structure is observed for jets which are absorbed by the medium. The above plots show that when the jet is absorbed, the sound structure of the momentum density generated becomes enhanced compared to the diffusive part. The reader interested in seeing the full animated evolution of Figures 6.7 and 6.8

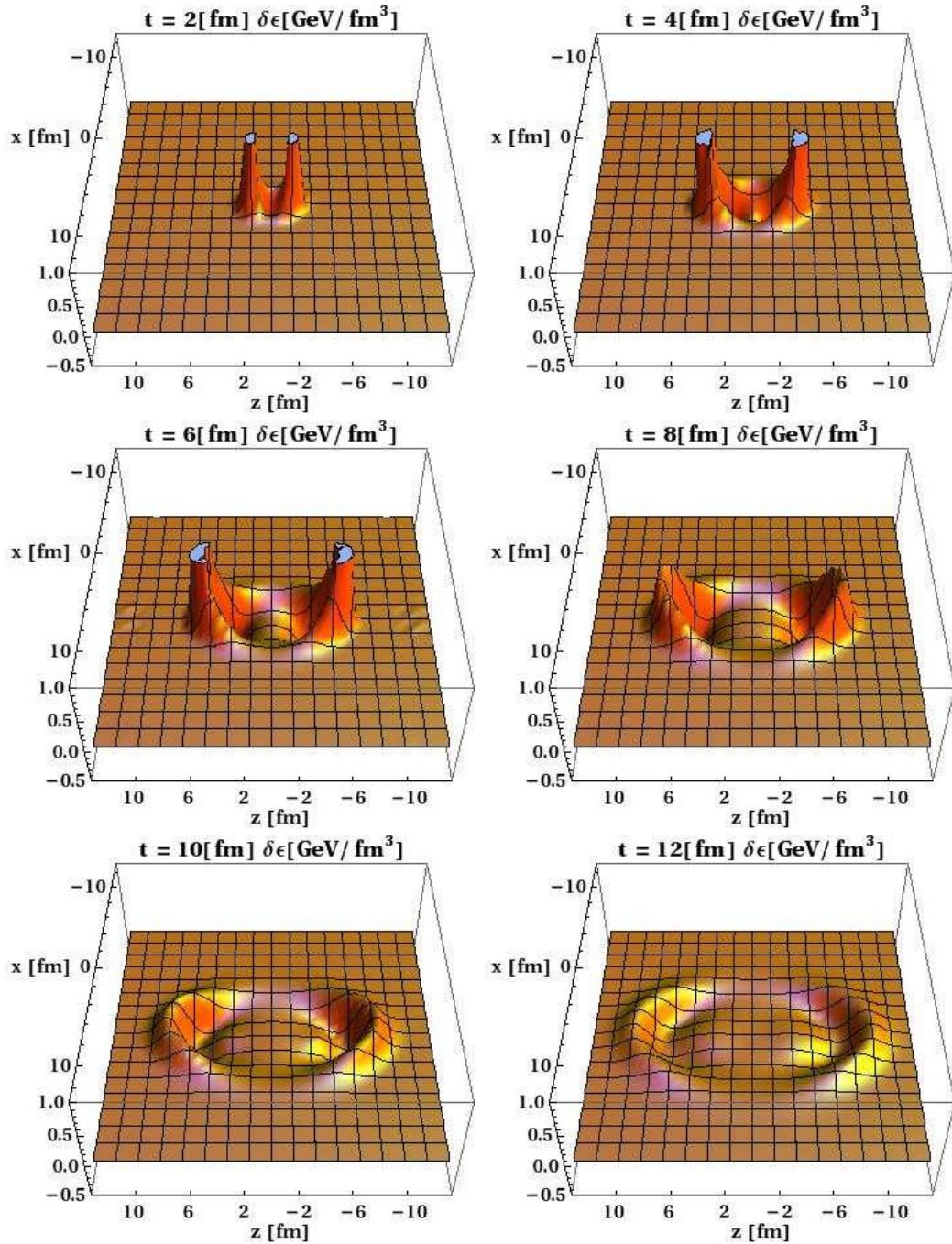


FIGURE 6.7: Time-evolution of $\delta\epsilon(\mathbf{x}, t)$. The plots are shown in the x - z plane, however, the results are cylindrically symmetric about the \hat{z} axis. The Mach cone formation is visible, particularly at later times. The radiative induced excitation leads to a t growth in the source strength, which manifests itself in the sharp rise of the induced wave at early times.

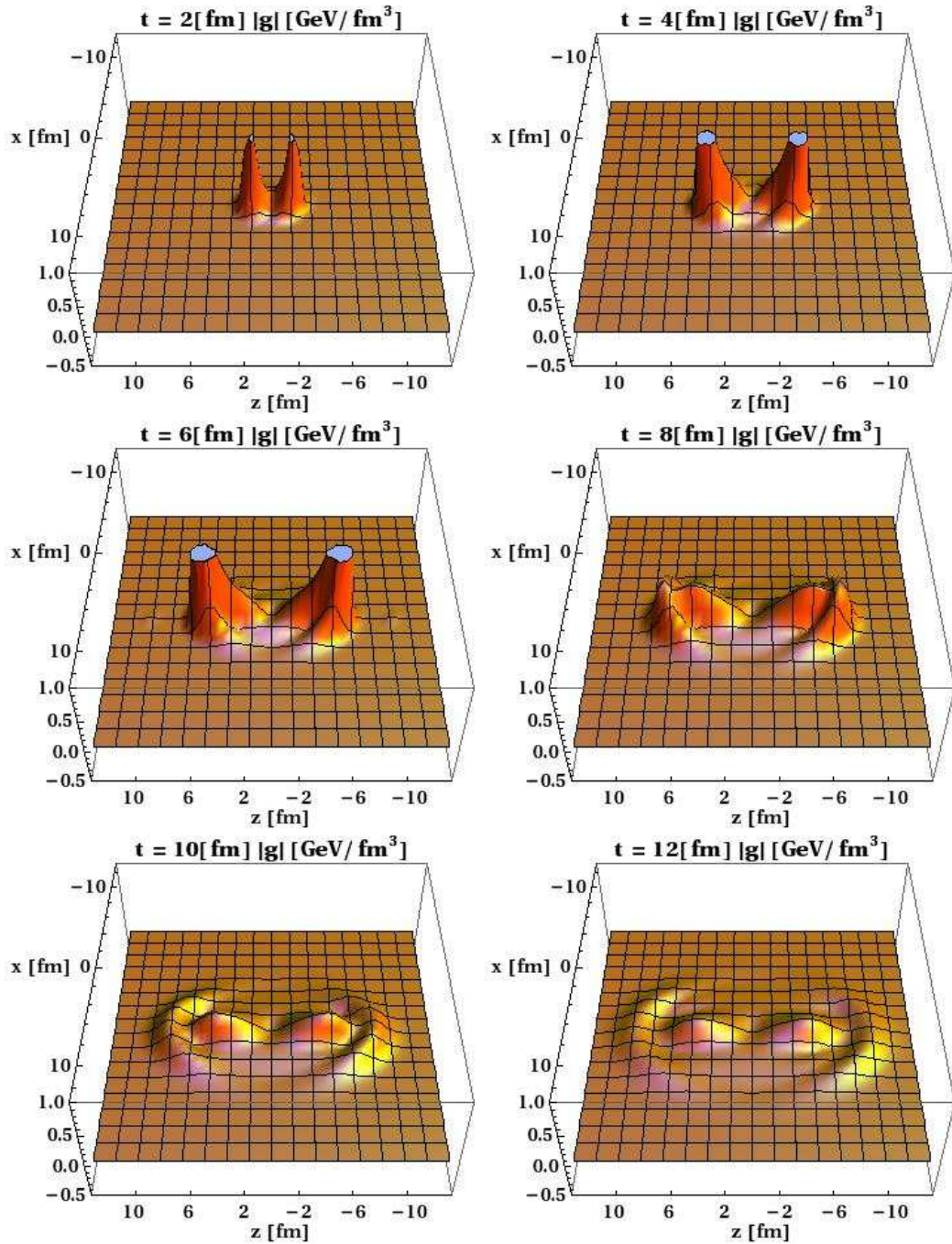


FIGURE 6.8: Time-evolution of $|g(\mathbf{x}, t)|$. The plots are shown in the x - z plane, however, the results are cylindrically symmetric about the \hat{z} axis. There is both a sound wave (from \mathbf{g}_L) and a diffusive wake (from \mathbf{g}_T). One can see in the plot shown at $t = 10$ fm, which is 4 fm after the source is absorbed by the medium, that the sound wave has separated from the diffusive wake to a large extent.

should visit the website: <https://fds.duke.edu/db/aas/Physics/grad/rbn2/files>.

6.4 Discussion and Conclusions

In this chapter results have been presented for the medium evolution of a static QGP coupled to the source terms discussed in Chapters 3 and 4. The primary numerical results are contained in the Figures above, where it has been shown that a conical sound wave is induced in the energy density and momentum density solutions, and that the momentum density also has a diffusive wake. It is interesting to consider how the results presented here compare to experimental data. In the di-hadron correlation functions measured at RHIC there is a double peak structure in the back-jet (source parton) distribution which has been interpreted by some as the result of Mach cone generated flow. In the spectrum presented here one indeed finds Mach cone generated flow but also finds a substantial diffusive flow, which seems to be missing from the RHIC data. In order to make a comparison, however, one must consider that the matter created in heavy ion collisions at RHIC rapidly expands in contrast to the static background assumed here. The diffusive momentum is deposited locally and is thus probably difficult to observe in an expanding medium. On the other hand, the Mach cone propagates at the speed of sound, which is of the same order of magnitude as the expansion velocities in the matter produced at RHIC, and is likely more readily observed experimentally. More will be said on the experimental implications in the next chapter.

Comparison of AdS/CFT and pQCD Results

As was mentioned in Chapter 2, the problem of a fast quark propagating through a strongly coupled $\mathcal{N} = 4$ supersymmetric Yang-Mills plasma has been examined [46, 47]. In this chapter, I will compare the results obtained in those calculations with what has been presented in this thesis. Gauge/string, or AdS/CFT, duality [77] has enabled many calculations to be handled analytically in the strongly coupled supersymmetric Yang-Mills plasma in the limit of the number of colors goes to infinity $N_c \rightarrow \infty$. Working in this limit, the authors of [47] have presented a detailed comparison of the hydrodynamic response of the background plasma to a fast quark and the exact solution. They found good agreement between the hydrodynamic description and the exact solution down to distances of about $1/T$ from the fast quark. In their work, the authors extracted the effective hydrodynamic source term generated by a fast quark in the theory and solved for the medium response in linearized hydrodynamics, similar to what was done in the previous chapter. For example, the source term presented there is expanded in gradients and written in

Fourier space as

$$\begin{aligned}
J^0(\mathbf{k}, \omega) &= \frac{\pi}{2} \sqrt{\lambda} T^2 u^2 \gamma 2\pi \delta(\omega - uk_z) \\
\mathbf{J}(\mathbf{k}, \omega) &= \frac{\pi}{2} \sqrt{\lambda} T^2 \gamma 2\pi \delta(\omega - uk_z) \left[\mathbf{u} \left(1 + i \frac{\omega}{\pi T} \right) - i u^2 \gamma \mathbf{k} \right]
\end{aligned} \tag{7.1}$$

where $\mathbf{u} = u\hat{z}$ is the velocity of the quark and $\sqrt{\lambda} = g\sqrt{N_c}$. For the most consistent comparison, recall the δ function expansion from Chapter 6, equation (6.29)

$$\begin{aligned}
J_D^0(\mathbf{k}, \omega) &= \frac{\alpha_s Q^2 m_D^2 u^2}{2} (2\pi) \delta(\omega - uk_z) \left(G_0 \left(\frac{m_D}{2\sqrt{E_p T}} \right) + \frac{i\pi(\mathbf{u} \cdot \mathbf{k})}{4 m_D \gamma} \right) \\
\mathbf{J}_D(\mathbf{k}, \omega) &= \frac{\alpha_s Q^2 m_D^2 u^2}{2} (2\pi) \delta(\omega - uk_z) \left(\mathbf{u} G_0 \left(\frac{m_D}{2\sqrt{E_p T}} \right) + \frac{i\pi}{8 m_D \gamma} (u^2 \mathbf{k} + \mathbf{u} \omega) \right)
\end{aligned} \tag{7.2}$$

In the above expression, $Q^2 = 4/3$ for a quark, $k_T = (k_x^2 + k_y^2)^{1/2}$, $\alpha_s = g^2/4\pi$ is the strong coupling, $m_D = gT$ and E_p is the energy of the quark.

The two results show some similarities and differences. To better highlight the comparison, it's useful to note that in the limit of $N_c \rightarrow \infty$ one can write for a quark

$$Q^2 = \frac{N_c^2 - 1}{2N_c} \rightarrow N_c/2 \tag{7.3}$$

in which case $\sqrt{N_c} = \sqrt{2} Q$. Then, the results in (7.1) are proportional to $\sqrt{2}\pi^2 T^2 \gamma g Q$ whereas the results in (7.2) are proportional to $T^2 g^4 Q^2/4$ (where factors of u^2 are taken as 1). Both are proportional to T^2 , however, the dependencies upon g and Q are noticeably different. Equally significant is that (7.1) is proportional to γ . The energy deposition of the AdS/CFT result is unbounded in the relativistic limit. For numerical comparison, choosing $g = 2$, $Q^2 = 4/3$ and $\gamma = 7$ one finds

$$\frac{\sqrt{2}\pi^2 T^2 \gamma g Q}{T^2 g^4 Q^2/4} \approx 42 \tag{7.4}$$

which is an enormous ratio.

There is another striking difference which may have phenomenological significance. The \mathbf{k} vector in \mathbf{J} shown in equation (7.1) is enhanced by a factor of γ , whereas in equation (7.2) it is suppressed by a factor of γ . Recall the discussion from Chapter 6 that terms in the source vector which are proportional to \mathbf{k} are especially efficient at generating sound waves. Naively, one then expects the AdS/CFT result to generate stronger hydrodynamic sound modes. However, consider that both equations (7.1) and (7.2) are an expansion in powers of the momentum, \mathbf{k} . On the other hand, (7.2) is taken in the relativistic limit, in which case it's not clear that $\gamma \mathbf{k} \ll 1$. In other words, the expansion in powers of \mathbf{k} given by (7.1) may not be valid in the relativistic limit, making a comparison questionable. This could be remedied by taking the Fourier transform of the full source (3.58), which I will not attempt here.

It is also interesting to compare the resulting medium response. In the upper panel of Figure 7.1 is plotted the solutions for the energy density and momentum density waves induced by a fast quark in the QGP using linearized hydrodynamics coupled to the relativistic limit of the source term derived in Chapter 3. In the lower panel is the same for the exact solution obtained in the AdS/CFT correspondence mentioned above. The plots have been scaled to dimensionless variables. One observes a similar structure in the two cases.

As was mentioned previously, a study was performed [40] which compared the azimuthal particle spectrum generated by a fast parton using an isochronous Cooper-Frye freeze-out from a static medium, using the source term derived in Chapter 3 of this thesis, here called the pQCD model, and the one obtained from AdS/CFT mentioned above. The authors found qualitatively different results when using the different models of the jet-medium interaction. In particular, they found that the long distance features of the medium response are too weak to generate a double peak structure at hadron freeze-out in either model. However, in the region immediately

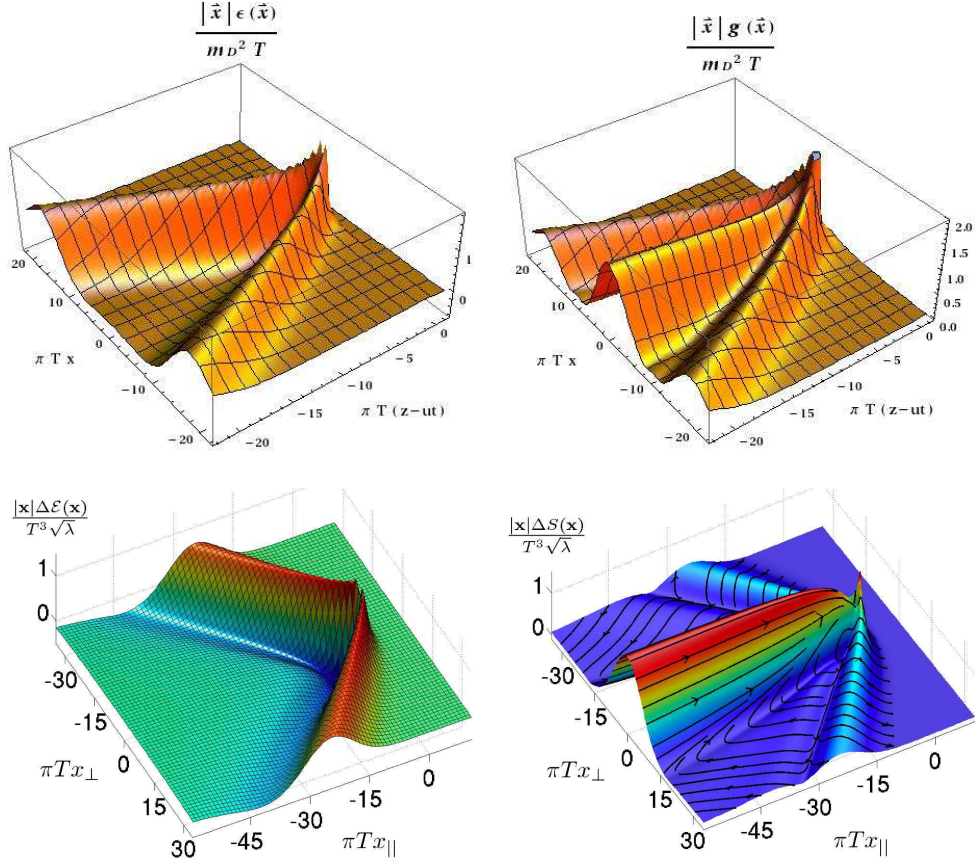


FIGURE 7.1: Comparing AdS/CFT and pQCD medium response. The upper panel shows the solutions [42] for the energy density and momentum density waves induced by a fast quark in the QGP using linearized hydrodynamics coupled to the relativistic limit of the source term derived in Chapter 3. The lower panel shows the same for the exact solution obtained in the AdS/CFT correspondence [47] mentioned in the main text.

near the fast quark, they found that strongly induced transverse flow present in the AdS/CFT model, but absent in the pQCD model, is strong enough to generate a double peak structure in the azimuthal particle spectrum. Their conclusion is that the anomalous azimuthal hadron correlations observed at RHIC are likely the result of flow generated by the non-equilibrium Neck zone in the AdS/CFT case, a contribution which does not obey Mach's law [41].

It is important to note that in the isochronous Cooper-Frye freeze-out scenario

the entire volume of matter is assumed to hadronize at the same time, independent of physical processes. This is in contrast to the freeze-out in a heavy ion collision, which occurs as the result of an expanding and cooling medium. The effect of an isochronous freeze-out scenario is that any cylindrically symmetric, or conical, contributions tend to be washed out (see the discussion in [45]). Any rigorous comparison to experimental results will require incorporating a realistic source term in an expanding medium, and using a realistic freeze-out scenario.

Summary

This thesis presented research concerning how hot quantum chromodynamic (QCD) matter, or the quark gluon plasma (QGP), responds to a fast parton. The QGP is formed when strongly interacting matter undergoes a transition at high temperature or high density from hadronic bound states to deconfined quarks and gluons and is experimentally accessible at high temperature in relativistic heavy-ion collisions, such as those done at the Relativistic Heavy-Ion Collider (RHIC) at Brookhaven National Lab and in the near future at the Large Hadron Collider (LHC) at CERN. Experimental measurements of hadron azimuthal correlations suggest that fast partons may generate conical, Mach-like, disturbances in the plasma. The work presented in this thesis develops and applies new theoretical methods that, when compared with measurements of hadron azimuthal correlations, could shed light on important properties of the quark gluon plasma such as the equation of state and transport coefficients like viscosity.

I investigated how the QGP responds to a fast parton by evaluating the source of energy and momentum generated by the fast parton in the medium. I developed

formalisms for evaluating the source of energy and momentum in perturbation theory with three different methods: classical kinetic theory, finite temperature field theory, and by including the energy lost by the hard parton to radiation. In Chapter 3, my approach was to treat the fast parton as the source of an external field in the medium using a Vlasov equation. It was possible to obtain an analytic expression for the source in the case without screening, as shown in (3.57) and (3.58). The total energy deposited per unit time by the fast parton in the medium predicted by (3.57) was shown to match the standard leading-logarithmic result for collisional energy loss in the QGP.

In Chapter 4, I adopted a different approach in order to include the radiative energy lost by the fast parton into the source of energy and momentum, something which was not included in the calculation of Chapter 3. Instead of considering the spatial structure of the source term, I gave attention to the the rate of energy absorbed by the medium and how that changes with time when radiative energy losses are included. The numerical results of this analysis were presented in Fig. 4.1, where it is seen that the rate of energy absorbed by the medium increases roughly linearly in time. In Chapter 5, I introduced and used the formalism of finite temperature field theory to calculate the source. The dynamics of a scalar field with quartic interaction coupled to a source current was analyzed in the field theory approach, and then in the Vlasov approach. Equations (5.40) and (5.54) showed the final results, from which it is seen that the source of energy and momentum in the scalar field theory is a total gradient with zero net energy deposition.

In Chapter 6, I obtained the response of the medium by coupling the source terms of Chapters 3 and 4 to a linearized hydrodynamic evolution. The medium response to the source derived in Chapter 3 was analyzed for different viscosities, speeds of sound, and for the relevance of finite spatial structure of the source. The results show a Mach cone formation in the medium, that weakens and broadens

as viscosity is increased. Additionally, the result was shown to be sensitive to the finite structure of the source term up to distances of several femtometers from the fast parton. The time evolution of the medium response to the source of Chapter 4 was also presented. The Mach cone formation was visible, particularly at later times. The radiative induced excitation led to a time growth in the source strength, which manifested itself in the sharp rise of the induced energy density wave at early times. The result for the magnitude of the momentum density showed that the sound wave separated from the diffusive wake to a large extent at later times. This may be directly relevant to the di-hadron correlation measurements discussed in Chapter 1. The double peak structure in these measurements is observed for jets that are absorbed by the medium. My results show that when the jet is absorbed, the sound structure of the momentum density generated becomes enhanced compared to the diffusive part. The reader interested in seeing the full animated evolution of the response of the medium to the source of Chapter 4 should visit the website: <https://fds.duke.edu/db/aas/Physics/grad/rbn2/files>.

Finally, in Chapter 7, I presented a comparison of the source of energy and momentum and the medium response of perturbative QCD (from Chapter 3 in this thesis) with that from the AdS/CFT gauge/string duality. Equation (7.4) compared the strength of the source in the two theories and Figure 7.1 compared the shape of the medium response.

While the goal of this thesis was to examine how the QGP at high temperature responds to fast partons, there are still many interesting questions which have yet to be answered. One of these is whether a rigorous theoretical calculation can conclusively equate the away side hadron correlation measurements with conical flow induced by fast partons. As was mentioned in Chapters 2 and 7, there are several monumental challenges that must be overcome to do this, the foremost of which is to implement a physically realistic formalism to describe the hadronization and

freeze-out of the partonic matter.

Another question relevant to the theoretical treatment of the away side hadron correlation measurements is whether or not hydrodynamics is the appropriate theory to describe the problem of a fast parton in a heavy-ion collision. As was discussed in Chapter 1, nearly ideal hydrodynamics has been successful in modeling the bulk evolution of a relativistic heavy-ion collision. However, the two problems are qualitatively different. The bulk evolution of the nuclear medium is a geometrically smooth system, for which gradient terms are small. On the other hand, a fast parton generates large gradients in the medium. The region where one finds the highest concentration of energy and momentum deposition is also the region where the hydrodynamic treatment becomes most questionable.

There are other interesting open questions related to the formal treatment of the source and medium interaction. For instance, the energy-momentum tensor of the AdS/CFT string theory coupled to a fast quark has been solved for exactly. As discussed in Chapter 2, it's unlikely the same can be done for QCD, however, the question remains as to how far the QCD evaluation can be taken. In particular, solving for the energy-momentum tensor in non-hydrodynamic regions could provide a qualitatively different perspective on the source/medium interaction. A similar question is what is the form of the complete hydrodynamic source term in QCD, including processes up to $(g^4T)^{-1}$. Also, it is yet to be seen if the field theoretic methods of Chapter 5 provide significant corrections to the Vlasov derived source term of Chapter 3.

The response of the QGP to fast partons will continue to receive interest from the heavy-ion community because of its central role in understanding QCD at high temperature. Whether or not conical flow generates the double peak seen in the di-hadron correlation measurements, there is still a medium response to fast partons. The forthcoming experiments at the LHC will allow the QGP to be probed at higher

energies than ever before and will improve the experimental capabilities for measuring the hadron correlation structure. I anticipate improved experimental results will be available to continue to help guide the theoretical development.

Appendix A: Derivation of (3.18) - (3.20)

In the HTL approximation, the source fields obey Maxwell's equations, which are given by

$$\nabla \cdot \mathbf{D}(\mathbf{x}, t) = \rho(\mathbf{x}, t) \quad (\text{A-1})$$

$$\nabla \times \mathbf{E}(\mathbf{x}, t) = -\frac{\partial \mathbf{B}(\mathbf{x}, t)}{\partial t} \quad (\text{A-2})$$

$$\nabla \cdot \mathbf{B}(\mathbf{x}, t) = 0 \quad (\text{A-3})$$

$$\nabla \times \mathbf{B}(\mathbf{x}, t) = \mathbf{j}(\mathbf{x}, t) + \frac{\partial \mathbf{D}(\mathbf{x}, t)}{\partial t} \quad (\text{A-4})$$

where the source density is

$$\rho(\mathbf{x}, t) = gQ_p \delta(\mathbf{x} - \mathbf{u}t) \quad (\text{A-5})$$

$$\mathbf{j}(\mathbf{x}, t) = \mathbf{u}\rho(\mathbf{x}, t) \quad (\text{A-6})$$

(in the above equations \mathbf{u} is the source particle's velocity and I have suppressed the color index, which I will restore in the final result). It is convenient to solve for the

fields by taking the Fourier transform of Maxwell's equations. Using the general rule

$$F(\mathbf{x}, t) = \frac{1}{(2\pi)^4} \int d^3k \int d\omega e^{i\mathbf{k}\cdot\mathbf{x} - i\omega t} F(\mathbf{k}, \omega) \quad (\text{A-7})$$

it is found that

$$i\mathbf{k} \cdot \mathbf{D}(\mathbf{k}, \omega) = \rho(\mathbf{k}, \omega) \quad (\text{A-8})$$

$$i\mathbf{k} \times \mathbf{E}(\mathbf{k}, \omega) = i\omega \mathbf{B}(\mathbf{k}, \omega) \quad (\text{A-9})$$

$$i\mathbf{k} \cdot \mathbf{B}(\mathbf{k}, \omega) = 0 \quad (\text{A-10})$$

$$i\mathbf{k} \times \mathbf{B}(\mathbf{k}, \omega) = \mathbf{j}(\mathbf{k}, \omega) - i\omega \mathbf{D}(\mathbf{k}, \omega) \quad (\text{A-11})$$

where

$$\rho(\mathbf{k}, \omega) = 2\pi g Q_p \delta(\omega - \mathbf{u} \cdot \mathbf{k}) \quad (\text{A-12})$$

$$\mathbf{j}(\mathbf{k}, \omega) = \mathbf{u} \rho(\mathbf{k}, \omega). \quad (\text{A-13})$$

The function \mathbf{D} is related to \mathbf{E} through the dielectric tensor ϵ_{ij} :

$$D_i = \epsilon_{ij} E_j \quad (\text{A-14})$$

(the summation over j is implied and I now suppress the (\mathbf{k}, ω) notation). In an isotropic medium the dielectric tensor can be decomposed into transverse and longitudinal parts such that

$$\epsilon_{ij} = \epsilon_L \frac{k_i k_j}{k^2} + \epsilon_T \left(\delta_{ij} - \frac{k_i k_j}{k^2} \right) \quad (\text{A-15})$$

and \mathbf{D} is now written as

$$\mathbf{D} = \epsilon_L \mathbf{E}_L + \epsilon_T \mathbf{E}_T \quad (\text{A-16})$$

where $\mathbf{E}_L = \hat{\mathbf{k}}(\hat{\mathbf{k}} \cdot \mathbf{E})$ and $\mathbf{E}_T = \mathbf{E} - \mathbf{E}_L$. One should note that $\mathbf{k} \cdot \mathbf{E}_T = 0$ and $\mathbf{k} \times \mathbf{E}_L = 0$. Maxwell's equations now take the form

$$i\epsilon_L \mathbf{k} \cdot \mathbf{E}_L = \rho \quad (\text{A-17})$$

$$i\mathbf{k} \times \mathbf{E}_T = i\omega \mathbf{B} \quad (\text{A-18})$$

$$i\mathbf{k} \cdot \mathbf{B} = 0 \quad (\text{A-19})$$

$$i\mathbf{k} \times \mathbf{B} = \mathbf{u}\rho - i\omega(\epsilon_L \mathbf{E}_L + \epsilon_T \mathbf{E}_T). \quad (\text{A-20})$$

An equation for \mathbf{B} can be obtained by crossing \mathbf{k} into (A-20) which combines with (A-18) and (A-19) to yield (with color index restored)

$$\mathbf{B}^a = \frac{2\pi ig Q_p^a (\mathbf{k} \times \mathbf{u})}{k^2 - \epsilon_T \omega^2} \delta(\omega - \mathbf{u} \cdot \mathbf{k}). \quad (\text{A-21})$$

One can then obtain \mathbf{E}_T by crossing \mathbf{k} into (A-18)

$$\mathbf{E}_T^a = \frac{\omega}{k^2} \mathbf{B} \times \mathbf{k} = \frac{2\pi ig Q_p^a \omega (\mathbf{u} k^2 - \mathbf{k}(\mathbf{k} \cdot \mathbf{u}))}{k^2(k^2 - \epsilon_T \omega^2)} \delta(\omega - \mathbf{u} \cdot \mathbf{k}). \quad (\text{A-22})$$

Combining (A-21) and (A-22) with (A-20) yields

$$\begin{aligned} \mathbf{E}_L^a &= (-1) \frac{i}{\epsilon_L \omega} \left(\mathbf{u}\rho + i \frac{k^2}{\omega} \mathbf{E}_T - i\omega \epsilon_T \mathbf{E}_T \right) \\ &= - \frac{2\pi ig Q_p^a (\mathbf{k} \cdot \mathbf{u})}{\epsilon_L \omega k^2} \mathbf{k} \delta(\omega - \mathbf{u} \cdot \mathbf{k}). \end{aligned} \quad (\text{A-23})$$

These results can be back transformed to position space to yield (3.18 - 3.20).

Appendix B: Details of obtaining (3.25)

In this appendix, I will show how the form of equation (3.25) was obtained. The relevant starting point is equation (3.22), which is written as

$$\int \frac{d\mathbf{p}}{(2\pi)^3} \frac{p^\mu p^\nu}{p^0} \frac{\partial f_0}{\partial x^\mu} = \int \frac{d\mathbf{p}}{(2\pi)^3} p^\nu \nabla_{p_i} D_{ij} \nabla_{p_j} f_0 \quad (\text{B-1})$$

where $p^\nu = (E, \mathbf{p})$ and I have used $v^\mu = p^\mu/p^0$. As discussed in Chapter 3, assuming the medium is locally thermal, in the frame comoving with any fluid element the following thermodynamic relations are valid

$$\int \frac{d\mathbf{p}}{(2\pi)^3} \frac{p^\mu p^\nu}{p^0} f_0 = (\epsilon + p)\delta^{0\mu}\delta^{0\nu} - pg^{\mu\nu}. \quad (\text{B-2})$$

I will be interested in evaluating the left-hand-side of (B-1). For any given volume element of the medium moving with a velocity, \mathbf{u} , the energy and momentum are related to the values in the comoving frame by

$$\mathbf{p} = \mathbf{p}' + \gamma\mathbf{u} \left(\frac{\gamma\mathbf{u} \cdot \mathbf{p}'}{\gamma + 1} + E' \right) \quad (\text{B-3})$$

and

$$E = \gamma(E' + \mathbf{p}' \cdot \mathbf{u}) \quad (\text{B-4})$$

where the primed quantities are the values in the comoving frame and $\gamma = 1/\sqrt{1 - \mathbf{u}^2}$. Similarly, the Jacobian determinant for this transformation is

$$d\mathbf{p} = d\mathbf{p}' \frac{E}{E'}. \quad (\text{B-5})$$

Thus, for the left-hand-side of (B-1), one has

$$\partial_\mu \int \frac{d\mathbf{p}}{(2\pi)^3} \frac{p^\mu p^\nu}{p^0} f_0 = \partial_\mu \int \frac{d\mathbf{p}'}{(2\pi)^3} \frac{p'^\mu p'^\nu}{p'^0} f_0 \quad (\text{B-6})$$

where

$$p^\mu = \left[\gamma(p'^0 + \mathbf{p}' \cdot \mathbf{u}), \mathbf{p}' + \gamma\mathbf{u} \left(\frac{\gamma\mathbf{u} \cdot \mathbf{p}'}{\gamma + 1} + p'^0 \right) \right]^\mu. \quad (\text{B-7})$$

What is left is to now explicitly evaluate the right-hand-side of (B-6). For instance, using (B-2),

$$\int \frac{d\mathbf{p}'}{(2\pi)^3} \frac{(p'^0)^2}{p'^0} f_0 = (w^0)^2(\epsilon + p) - p \quad (\text{B-8})$$

where I have defined the medium 4-velocity $w^\mu = \gamma(1, \mathbf{u})^\mu$. Also,

$$\int \frac{d\mathbf{p}'}{(2\pi)^3} \frac{p^0 p^i}{p'^0} f_0 = w^0 w^i (\epsilon + p) \quad (\text{B-9})$$

and

$$\int \frac{d\mathbf{p}'}{(2\pi)^3} \frac{p^i p^j}{p'^0} f_0 = w^i w^j (\epsilon + p) + \delta^{ij} p. \quad (\text{B-10})$$

The results (B-8 - B-10) can be combined into one expression

$$\int \frac{d\mathbf{p}'}{(2\pi)^3} \frac{p^\mu p^\nu}{p'^0} f_0 = T^{\mu\nu} \quad (\text{B-11})$$

where $T^{\mu\nu} \equiv w^\mu w^\nu (\epsilon + p) - g^{\mu\nu} p$. Combining the above results with (B-1) yields equation (3.25)

$$\partial_\mu T^{\mu\nu} = J^\nu. \quad (\text{B-12})$$

Appendix C: Explicit evaluation of the $\hat{\mathbf{v}}$ integration

In going from Eq. (3.34) to (3.35) and (3.36) I performed an integration over $\hat{\mathbf{v}}$ by choosing a frame in which $\mathbf{k}' = k' \hat{\mathbf{z}}$, performing the integral, and then rotating back into a frame in which \mathbf{k}' is arbitrary. In this appendix the explicit details involved will be given. The relevant starting point is

$$\int d\hat{\mathbf{v}} \frac{\hat{\mathbf{v}} \cdot \mathbf{E}'^a (\delta_{0\nu} \hat{\mathbf{v}} \cdot \mathbf{E}^a + \delta_{i\nu} (E_i^a + (\hat{\mathbf{v}} \times \mathbf{B})_i^a))}{4\pi(\omega' - \mathbf{k}' \cdot \hat{\mathbf{v}} + i\epsilon)} \quad (\text{C-1})$$

where \mathbf{E}'^a is short for $\mathbf{E}^a(k')$, etc. There are two basic integrals to consider, which have the form

$$\int d\hat{\mathbf{v}} \frac{\hat{\mathbf{v}}_j}{4\pi(\omega' - \mathbf{k}' \cdot \hat{\mathbf{v}} + i\epsilon)} \equiv I_j \quad (\text{C-2})$$

$$\int d\hat{\mathbf{v}} \frac{\hat{\mathbf{v}}_j \hat{\mathbf{v}}_m}{4\pi(\omega' - \mathbf{k}' \cdot \hat{\mathbf{v}} + i\epsilon)} \equiv I_{jm}. \quad (\text{C-3})$$

Now specify that $\mathbf{k}' = k'\hat{\mathbf{z}}$ and consider that since $\hat{\mathbf{v}} = (\sin\theta\cos\phi, \sin\theta\sin\phi, \cos\theta)$ the integral over $d\phi$ will ensure that only I_z survives in (C-2). Making the replacement $d\hat{\mathbf{v}} \rightarrow \int d\theta d\phi \sin\theta$ gives

$$\begin{aligned} I_z &= \int d\theta d\phi \frac{\sin\theta\cos\theta}{4\pi(\omega' - k'\cos\theta + i\epsilon)} \\ &= \frac{1}{2} \int_{-1}^1 \frac{d\xi \xi}{(\omega' - k'\xi + i\epsilon)} \equiv \Omega_1. \end{aligned} \quad (\text{C-4})$$

Similarly, in (C-3) the integral over $d\phi$ ensures only I_{xx} , I_{yy} , and I_{zz} contribute:

$$I_{xx} = I_{yy} = \frac{1}{4} \int_{-1}^1 \frac{d\xi(1-\xi^2)}{(\omega' - k'\xi + i\epsilon)} \equiv \Omega_2 \quad (\text{C-5})$$

and

$$I_{zz} = \frac{1}{2} \int_{-1}^1 \frac{d\xi \xi^2}{(\omega' - k'\xi + i\epsilon)} \equiv \Omega_3. \quad (\text{C-6})$$

The Ω_i terms are evaluated with the result

$$\Omega_1(k) = \frac{1}{2k} \left(\frac{\omega}{k} \ln \left[\frac{k+\omega}{k-\omega} \right] - \frac{\pi i \omega}{k} - 2 \right) \quad (\text{C-7})$$

$$\begin{aligned} \Omega_2(k) &= \frac{1}{4k} \left(\left(1 - \frac{\omega^2}{k^2}\right) \ln \left[\frac{k+\omega}{k-\omega} \right] \right. \\ &\quad \left. - \pi i \left(1 - \frac{\omega^2}{k^2}\right) + 2\frac{\omega}{k} \right) \end{aligned} \quad (\text{C-8})$$

$$\Omega_3(k) = \frac{\omega}{2k^2} \left(\frac{\omega}{k} \ln \left[\frac{k+\omega}{k-\omega} \right] - \frac{\pi i \omega}{k} - 2 \right) = \frac{\omega}{k} \Omega_1(k). \quad (\text{C-9})$$

Equations (C-4 - C-6) can be rewritten as

$$I_j = \delta_{jz} \Omega_1 \quad (\text{C-10})$$

$$\begin{aligned} I_{jm} &= (\delta_{jx}\delta_{mx} + \delta_{jx}\delta_{mx}) \Omega_2 + \delta_{jz}\delta_{mz} \Omega_3 \\ &= \delta_{jm} \Omega_2 + \delta_{jz}\delta_{mz} \left(\frac{\omega}{k} \Omega_1 - \Omega_2 \right). \end{aligned} \quad (\text{C-11})$$

In the above expressions the subscript z denotes the orientation of the \mathbf{k}' vector. Generalizing to an arbitrary \mathbf{k}' is done by making the replacement $\delta_{jz} \rightarrow \mathbf{k}'_j$ in (C-10) and (C-11). Going back to (C-1) (and suppressing the color index) I find

$$\begin{aligned}
& \int d\hat{\mathbf{v}} \frac{\hat{\mathbf{v}} \cdot \mathbf{E}'^a (\delta_{0\nu} \hat{\mathbf{v}} \cdot \mathbf{E}^a + \delta_{i\nu} (E_i^a + (\hat{\mathbf{v}} \times \mathbf{B})_i^a))}{4\pi(\omega' - \mathbf{k}' \cdot \hat{\mathbf{v}} + i\epsilon)} = \\
& \delta_{0\nu} E'_j E'_m I_{jlm} + \delta_{i\nu} (E'_j E'_i I_j + \epsilon_{imk} I_{jlm} E'_j B_k) = \\
& \delta_{0\nu} \left((\mathbf{E}' \cdot \mathbf{E}) \Omega_2 + (\hat{\mathbf{k}}' \cdot \mathbf{E}') (\hat{\mathbf{k}}' \cdot \mathbf{E}) \left(\frac{\omega}{k} \Omega_1 - \Omega_2 \right) \right) + \\
& \delta_{i\nu} \left((\hat{\mathbf{k}}' \cdot \mathbf{E}') E_i \Omega_1 + \right. \\
& \quad \left. \left((\mathbf{E}' \times \mathbf{B})_i \Omega_2 + (\hat{\mathbf{k}}' \cdot \mathbf{E}') (\hat{\mathbf{k}}' \times \mathbf{B})_i \left(\frac{\omega}{k} \Omega_1 - \Omega_2 \right) \right) \right)
\end{aligned} \tag{C-12}$$

which is the result given in (3.35) and (3.36).

Appendix D: Evaluation of ξ_1, \dots, ξ_6

In Sec. 3.3, I put off the explicit evaluation of the terms ξ_1, \dots, ξ_6 and directly went to the results (3.57) and (3.58). In this appendix, I will give a detailed derivation of the expressions:

$$\begin{aligned}
\begin{bmatrix} \xi_1 \\ \xi_2 \\ \xi_3 \\ \xi_4 \end{bmatrix} & \equiv \int dk_z dk_T \frac{e^{i(z-ut)kz} \Omega_1(k)}{k D_L(k)} \begin{bmatrix} J_0(\rho k_T) k_T k^2 \\ J_0(\rho k_T) k_T k_z^2 \\ J_0(\rho k_T) k_T^3 \\ J_1(\rho k_T) k_z k_T^2 \end{bmatrix} \\
\begin{bmatrix} \xi_5 \\ \xi_6 \end{bmatrix} & \equiv \int dk_z dk_T \frac{e^{i(z-ut)kz} \Omega_2(k)}{k^2 D_T(k)} \begin{bmatrix} J_0(\rho k_T) k_z k_T^3 \\ J_1(\rho k_T) k_T^2 k_z^2 \end{bmatrix}.
\end{aligned} \tag{D-1}$$

Here, I am interested in the unscreened source term which is found by setting $D_L(k) = k^2$ and $D_T(k) = k^2 - u^2 k_z^2$. I start by changing to polar coordinates (i.e., k and θ , where $k_z = k \cos \theta$ and $k_T = k \sin \theta$) in which case the two Ω terms

can be written as

$$\Omega_1(k) = \frac{G_1(\theta)}{2k} \quad (\text{D-2})$$

$$\Omega_2(k) = \frac{G_2(\theta)}{4k} \quad (\text{D-3})$$

where

$$G_1(\theta) = 2u \cos \theta \tanh^{-1}[u \cos \theta] - i\pi u \cos \theta - 2 \quad (\text{D-4})$$

and

$$G_2(\theta) = 2 \tanh^{-1}[u \cos \theta](1 - u^2 \cos^2 \theta) - i\pi(1 - u^2 \cos^2 \theta) + 2u \cos \theta. \quad (\text{D-5})$$

Defining $\Lambda(\theta)$ as some generic function, I now write the general form of the k integration as

$$\xi_i = \int dk d\theta \sin \theta e^{ik((z-ut) \cos \theta)} \begin{bmatrix} J_0(\rho k \sin \theta) \\ J_1(\rho k \sin \theta) \end{bmatrix} \Lambda_i(\theta) \quad (\text{D-6})$$

which can be evaluated using the relations [78]:

$$\int_0^\infty dk e^{iky} J_0(kb) = \frac{1}{\sqrt{b^2 - (y + i\epsilon)^2}} \quad (\text{D-7})$$

$$\int_0^\infty dk e^{iky} J_1(kb) = \frac{1}{b} \left(1 + \frac{iy}{\sqrt{b^2 - (y + i\epsilon)^2}} \right) \quad (\text{D-8})$$

where $b > 0$ and ϵ is a positive infinitesimal quantity. Defining $a \equiv (z - ut)/\rho$ and using the above integrals allows

$$\begin{aligned} \xi_i &= \int dk d\theta \sin \theta e^{ik((z-ut) \cos \theta)} \begin{bmatrix} J_0(\rho k \sin \theta) \\ J_1(\rho k \sin \theta) \end{bmatrix} \Lambda_i(\theta) \\ &= \int_0^\pi d\theta \frac{1}{\rho} \left[1 + \frac{\frac{\sin \theta}{\sqrt{\sin^2 \theta - (a \cos \theta + i\epsilon)^2}}}{\rho \sqrt{\sin^2 \theta - (a \cos \theta + i\epsilon)^2}} \right] \Lambda_i(\theta) \\ &\equiv \int_0^\pi d\theta \frac{1}{\rho} \begin{bmatrix} U(\theta) \\ L(\theta) \end{bmatrix} \Lambda_i(\theta). \end{aligned} \quad (\text{D-9})$$

where I have set $t = 0$ for conciseness. Explicitly, the terms look like

$$\begin{aligned} \begin{bmatrix} \xi_1 \\ \xi_2 \\ \xi_4 \end{bmatrix} &= \int_0^\pi d\theta \frac{1}{2\rho} G_1(\theta) \begin{bmatrix} U(\theta) \\ U(\theta) \cos^2 \theta \\ L(\theta) \cos \theta \sin \theta \end{bmatrix} \\ \begin{bmatrix} \xi_5 \\ \xi_6 \end{bmatrix} &= \int_0^\pi d\theta \frac{1}{4\rho} G_2(\theta) \begin{bmatrix} U(\theta) \cos \theta \sin^2 \theta \\ L(\theta) \cos^2 \theta \sin \theta \end{bmatrix}. \end{aligned} \quad (\text{D-10})$$

where ξ_3 is omitted since it will not appear in the final expressions.

It is imperative to consider symmetry before trying to evaluate the various terms. For instance, in ξ_1, \dots, ξ_4 the imaginary part of $U(\theta)$ and the real part of $L(\theta)$ only need to multiply against the term $-i\pi u \cos \theta$ due to symmetry considerations. Similarly, the real part of $U(\theta)$ and the imaginary part of $L(\theta)$ do not need to multiply against $-i\pi u \cos \theta$. It turns out that due to symmetry the terms involving the imaginary part of $U(\theta)$ and the real part of $L(\theta)$ are easier to evaluate than those involving the real part of $U(\theta)$ and the imaginary part of $L(\theta)$. It makes sense to first get these simpler expressions out of the way and then focus on the more tedious ones. I introduce the notation $\xi_i = \xi_{ia} + \xi_{ib}$, where ξ_{ia} now denotes terms involving the imaginary part of $U(\theta)$ and the real part of $L(\theta)$. Using *Mathematica 6.0* these terms can be evaluated and I find

$$\begin{aligned} \begin{bmatrix} \xi_{1a} \\ \xi_{2a} \\ \xi_{4a} \end{bmatrix} &= \begin{bmatrix} \frac{\pi a u}{\rho \chi^2} \\ \frac{\pi a u (3+a^2)}{3\rho \chi^4} \\ -\frac{i\pi u}{3\rho} \left(1 - \frac{z a (3+a^2)}{\rho \chi^4}\right) \end{bmatrix} \\ \begin{bmatrix} \xi_{5a} \\ \xi_{6a} \end{bmatrix} &= \begin{bmatrix} \frac{\pi a^3}{3\rho \chi^4} \\ -\frac{i\pi}{6\rho} \left(1 - \frac{z a (3+a^2)}{\rho \chi^4}\right) \end{bmatrix} \end{aligned} \quad (\text{D-11})$$

where $\chi \equiv \sqrt{1+a^2}$.

Now I turn to the more involved ξ_{ib} terms which involve the real part of $U(\theta)$

and the imaginary part of $L(\theta)$. It is convenient to note that

$$\operatorname{Re}[U(\theta)] = \sin \theta \operatorname{Re} \left[\frac{1}{\sqrt{\sin^2 \theta - a^2 \cos^2 \theta}} \right] \quad (\text{D-12})$$

$$\operatorname{Im}[L(\theta)] = \frac{z \cos \theta}{\rho} \operatorname{Re} \left[\frac{1}{\sqrt{\sin^2 \theta - a^2 \cos^2 \theta}} \right]. \quad (\text{D-13})$$

For the sake of bookkeeping, I note there are 7 distinct integrations which need to be performed. These terms are given by the real parts of

$$\varphi_i = \int d\theta \frac{\sin \theta}{\sqrt{\sin^2 \theta - a^2 \cos^2 \theta}} T_i \quad (\text{D-14})$$

where

$$\begin{bmatrix} T_1 \\ T_2 \\ T_3 \\ T_4 \\ T_5 \\ T_6 \\ T_7 \end{bmatrix} \equiv \begin{bmatrix} 1 \\ \cos^2 \theta \\ \cos \theta \tanh^{-1}[u \cos \theta] \\ \cos^3 \theta \tanh^{-1}[u \cos \theta] \\ \cos \theta \sin^2 \theta \tanh^{-1}[u \cos \theta] \\ \cos^2 \theta \sin^2 \theta / (1 - u^2 \cos^2 \theta) \\ \cos^4 \theta / (1 - u^2 \cos^2 \theta) \end{bmatrix}. \quad (\text{D-15})$$

In terms of these the ξ_{ib} are

$$\begin{bmatrix} \xi_{1b} \\ \xi_{2b} \\ \xi_{4b} \\ \xi_{5b} \\ \xi_{6b} \end{bmatrix} = \frac{1}{\rho} \begin{bmatrix} u\varphi_3 - \varphi_1 \\ u\varphi_4 - \varphi_2 \\ \frac{z}{\rho}(u i \varphi_4 - i \varphi_2) \\ (\varphi_5 + u\varphi_6)/2 \\ \frac{z}{2\rho}(i\varphi_4 + i u \varphi_7) \end{bmatrix}. \quad (\text{D-16})$$

Using *Mathematica 6.0* I find for the real parts of the φ terms:

$$\varphi_1 = \frac{\pi}{\chi} \quad (\text{D-17})$$

$$\varphi_2 = \frac{\pi}{2\chi^3} \quad (\text{D-18})$$

$$\varphi_3 = \frac{\pi}{u\chi^2} \left(\chi - \sqrt{a^2 + 1/\gamma^2} \right) \quad (\text{D-19})$$

$$\varphi_4 = \frac{(\chi^2 + 2u^2)}{3u^2\chi^2} \varphi_3 - \frac{\pi}{6u\chi^3} \quad (\text{D-20})$$

$$\varphi_5 = \varphi_3 - \varphi_4 \quad (\text{D-21})$$

$$\varphi_6 = \frac{\pi}{\gamma^2 u^4} \left(\frac{2\chi^2 + \gamma^2 u^2}{2\chi^3} - \frac{1}{\sqrt{a^2 + 1/\gamma^2}} \right) \quad (\text{D-22})$$

$$\varphi_7 = \frac{\pi}{u^2} \left(-\frac{1}{\chi} + \frac{1}{\sqrt{a^2 + 1/\gamma^2}} \right) - \varphi_6 \quad (\text{D-23})$$

Combining the above results I find

$$\xi_1 = \frac{-\pi \left(\sqrt{a^2 + 1/\gamma^2} - au \right)}{\rho\chi^2}$$

$$\xi_5 = \frac{\pi \left(2\sqrt{a^2 + \frac{1}{\gamma^2}}\gamma^2 (a^3 u^3 + \chi^3) + (1 + a^2\gamma^2) (2u^2 + \chi^2(1 - 3u^2)) - 3\chi^4 \right)}{6\rho u^3 \chi^4 \sqrt{a^2 + \frac{1}{\gamma^2}}\gamma^2}$$

$$\xi_1 - u^2 \xi_2 = -\frac{\pi}{3\rho\chi^4} \left(au^3 (2 + \chi^2) + \chi^2 (\chi - 3au) + 2\sqrt{a^2 + \frac{1}{\gamma^2}} (\chi^2 - u^2) \right) \quad (\text{D-24})$$

$$u\xi_2 - u^2 \xi_5 = \frac{\pi u \left(a \left(-2a\gamma^2 + 2u\gamma^2 \sqrt{a^2 + \frac{1}{\gamma^2}} + a \right) - 1 \right)}{2\chi^4 \sqrt{a^2 + \frac{1}{\gamma^2}}\gamma^2}$$

$$u\xi_6 + 2\xi_4 = \frac{i\pi z \left(-a^2 + (a^2 + 3)ua\sqrt{a^2 + \frac{1}{\gamma^2}} + 2u^2 - 1 \right)}{2\chi^4 \sqrt{a^2 + \frac{1}{\gamma^2}}\rho} - \frac{i\pi u}{2}$$

which are combined with (3.49) to yield (3.57) and (3.58).

Appendix E: Numerically Integrating Equation (3.40)

As mentioned in Sec.3.4, the evaluation of the 12 ξ_i terms listed in (3.40) with medium screening included must be done numerically. In this appendix I will discuss

the specific techniques used to perform these numerical integrations. The ξ_i terms are given by

$$\begin{bmatrix} \xi_1 \\ \xi_2 \\ \xi_3 \\ \xi_4 \end{bmatrix} \equiv \int dk_z dk_T \frac{e^{i(z-ut)k_z} \Omega_1(k)}{k D_L(k)} \begin{bmatrix} J_0(\rho k_T) k_T k^2 \\ J_0(\rho k_T) k_T k_z^2 \\ J_0(\rho k_T) k_T^3 \\ J_1(\rho k_T) k_z k_T^2 \end{bmatrix} \quad (\text{E-1})$$

$$\begin{bmatrix} \xi_5 \\ \xi_6 \end{bmatrix} \equiv \int dk_z dk_T \frac{e^{i(z-ut)k_z} \Omega_2(k)}{k^2 D_T(k)} \begin{bmatrix} J_0(\rho k_T) k_z k_T^3 \\ J_1(\rho k_T) k_T^2 k_z^2 \end{bmatrix} \quad (\text{E-2})$$

$$\begin{bmatrix} \xi_7 \\ \xi_8 \end{bmatrix} \equiv \int dk_z dk_T \frac{e^{i(z-ut)k_z}}{D_L(k)} \begin{bmatrix} J_1(\rho k_T) k_T^2 \\ J_0(\rho k_T) k_z k_T \end{bmatrix} \quad (\text{E-3})$$

$$\begin{bmatrix} \xi_9 \\ \xi_{10} \\ \xi_{11} \\ \xi_{12} \end{bmatrix} \equiv \int dk_z dk_T \frac{e^{i(z-ut)k_z}}{k^2 D_T(k)} \begin{bmatrix} J_1(\rho k_T) k_T^2 k^2 \\ J_1(\rho k_T) k_T^4 \\ J_1(\rho k_T) k_T^2 k_z^2 \\ J_0(\rho k_T) k_z k_T^3 \end{bmatrix} \quad (\text{E-4})$$

where the k_z integration runs from $\pm\infty$ and the k_T integration ranges from $0 \rightarrow \infty$. Since each ξ_i contains a double integration which ranges over an infinite interval, care must be taken to cast each term in a form that will tend to zero as quickly as possible in order to make numerical evaluation feasible. In the case of the integrals over dk_z , we can take advantage by the exponential term $e^{i(z-ut)k_z}$ by *bending the contour* in the imaginary plane. The strategy works as follows: start with a function of the form

$$\int_{-\infty}^{\infty} e^{i(z-ut)k_z} f(k_z) dk_z \quad (\text{E-5})$$

where $f(k_z)$ is an analytic function. Next, bend the contour of the integral in the complex plane by making the variable change

$$k_z \rightarrow r e^{i\alpha \text{Sign}[r]} \quad (\text{E-6})$$

and

$$dk_z \rightarrow dr e^{i\alpha \text{Sign}[r]} \quad (\text{E-7})$$

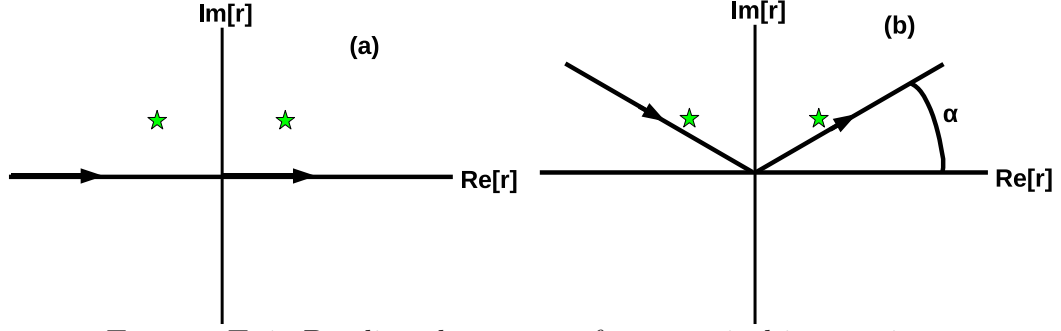


FIGURE E-1: Bending the contour for numerical integration.

where the limits of integration on r are from $-\infty$ to ∞ . Under this change, (E-5) becomes

$$\int_{-\infty}^{\infty} \exp[i(z - ut)re^{i\alpha\text{Sign}[r]}]f(re^{i\alpha\text{Sign}[r]})e^{i\alpha\text{Sign}[r]}dr \quad (\text{E-8})$$

and now the exponential term is damped in (E-8) [provided α has the same sign as $(z - ut)$] making the integral more numerically manageable. (E-8) and (E-5) will be equivalent if the integrand vanishes as $r \rightarrow \pm\infty$ and no poles from $f(k_z)$ are crossed when bending the contour (this places a restriction on the value of α). This method is illustrated in Figure E-1, where diagram (a) shows the integration contour before bending, and diagram (b) shows it after bending. The two green-yellow stars indicate the possible location of poles, which restrict how large α can be.

Before applying this technique it is necessary to consider where the ξ_i have poles. Any poles located directly on the imaginary axis will not affect the result so we can ignore those. That leaves us to consider where the zeros of $D_T(uk_z)$ and $D_L(uk_z)$ are. An analytic solution for the zeros of $D_T(uk_z)$ and $D_L(uk_z)$ is impossible because of the logarithmic terms. However, the zeros can be searched for numerically. Using the parameters $\mathbf{u} = 0.99\hat{z}$ and $m_D = 0.4$ GeV, it is found that all poles are sufficiently close to the imaginary axis so that the value of α used is not restricted for any reasonable value for terms with $D_T(uk_z)$ in the denominator. I choose to use $|\alpha| = 1$. However, for terms with $D_L(uk_z)$ in the denominator, it is found that for values of

$k_T \lesssim 1/2$ poles become increasingly close to the real axis. For this reason, I choose to break up the integration in the terms with $D_L(uk_z)$ in the denominator into a term

$$\int_1^\infty dk_T \int_{-\infty}^\infty dk_z \quad (\text{E-9})$$

which I bend in the complex plane with a value of $|\alpha| = 1$ and a term

$$\int_0^1 dk_T \int_{-\infty}^\infty dk_z \quad (\text{E-10})$$

which I do not bend in the complex plane. For the terms I do not bend in the complex plane it is usually necessary to subtract off the asymptotic form of the k_z integration in order to make the numerical integration efficient. The asymptotic form must then be added back. Similarly, for the terms I do bend in the complex plane, I usually must subtract off the asymptotic form of the k_T integration to provide efficient convergence.

In the case of $z = ut$, it does not make sense to bend the k_z integral in the complex plane since there will be no damping term from the exponential. In this case, I instead perform the numerical integration by subtracting off the unscreened form of ξ_i in the integrand (which has the same large k form) and then re-adding after evaluation.

To make these ideas more concrete, consider ξ_7 for the case of $z \neq ut$. I write

$$\int_{-\infty}^\infty dk_z \int_1^\infty dk_T e^{i(z-ut)k_z} J_1(\rho k_T) \left(\frac{k_T^2}{D_L(uk_z)} - 1 \right) \quad (\text{E-11})$$

where I have subtracted 1 to make the k_T integration more efficient. I bend the above contour in the complex plane and perform the integration and then re-add

$$\int_{-\infty}^\infty dk_z \int_1^\infty dk_T e^{i(z-ut)k_z} J_1(\rho k_T) \sim \delta(z - ut) \quad (\text{E-12})$$

which can be ignored, since it only contributes when $z = ut$. Next, I integrate

$$\begin{aligned}
& \int_{-1}^1 dk_z \int_0^1 dk_T e^{i(z-ut)k_z} J_1(\rho k_T) \frac{k_T^2}{D_L(uk_z)} \\
& + \int_1^\infty dk_z \int_0^1 dk_T e^{i(z-ut)k_z} J_1(\rho k_T) \left(\frac{k_T^2}{D_L(uk_z)} - \frac{k_T^2}{k_z^2} \right) \\
& + \int_{-1}^{-\infty} dk_z \int_0^1 dk_T e^{i(z-ut)k_z} J_1(\rho k_T) \left(\frac{k_T^2}{D_L(uk_z)} - \frac{k_T^2}{k_z^2} \right)
\end{aligned} \tag{E-13}$$

where I have subtracted k_T^2/k_z^2 to make the k_z integration more efficient. I then must re-add

$$\begin{aligned}
2\text{Re} \left[\int_1^\infty dk_z \int_0^1 dk_T e^{i(z-ut)k_z} J_1(\rho k_T) \frac{k_T^2}{k_z^2} \right] = \\
\frac{J_2(\rho)}{\rho} (2(\cos(z) + z\text{Si}(z)) - \pi|z|).
\end{aligned} \tag{E-14}$$

Considering ξ_7 for the case of $z = ut$, I write

$$\int_{-\infty}^\infty dk_z \int_0^\infty dk_T J_1(\rho k_T) \left(\frac{k_T^2}{D_L(uk_z)} - \frac{k_T^2}{k_T^2 + k_z^2} \right) \tag{E-15}$$

and then analytically re-add [see (3.49)]

$$\begin{aligned}
& \int_{-\infty}^\infty dk_z \int_0^\infty dk_T e^{i(z-ut)k_z} J_1(\rho k_T) \frac{k_T^2}{k_T^2 + k_z^2} \\
& = \frac{\pi\rho}{(\rho^2 + (z-ut)^2)^{3/2}}
\end{aligned} \tag{E-16}$$

and evaluate at $z = ut$.

Appendix F: Obtaining the Fourier Representation of (3.43) and (6.20)

In Sec.6.1.2 the explicit determination of the Fourier transform of the full source was put off to this appendix. Including the damping factor, $e^{-\rho m}$, one has for the inverse

Fourier transforms of (3.43) and (6.20)

$$\mathbf{J}(\mathbf{k}, \omega) = \frac{\alpha_s(Q_p^a)^2 m_D^2 u^2}{8\pi} \times \int d^4x e^{ik \cdot x - \rho m} \left(\frac{\gamma \mathbf{u}}{(z_-^2 \gamma^2 + \rho^2)^{3/2}} + \nabla \frac{u^2}{2(z_-^2 \gamma^2 + \rho^2)} \right) \quad (\text{F-1})$$

and

$$\mathcal{J}^0(\mathbf{k}, \omega) = \frac{\alpha_s(Q_p^a)^2 m_D^2 \gamma u^2}{8\pi} \times \int d^4x e^{ik \cdot x - \rho m} \left(\frac{1}{(z_-^2 \gamma^2 + \rho^2)^{3/2}} - \frac{\gamma u z_-}{(z_-^2 \gamma^2 + \rho^2)^2} \right). \quad (\text{F-2})$$

After an integration by parts, the second term in (F-1) takes the form

$$\int d^4x \frac{u^2 e^{ik \cdot x - \rho m}}{2(z_-^2 \gamma^2 + \rho^2)} (i\mathbf{k} + m(\cos \phi, \sin \phi, 0)) \quad (\text{F-3})$$

where I am working in plane polar coordinates, ρ and ϕ , such that $x = \rho \cos \phi$ and $y = \rho \sin \phi$.

It is clear there are three distinct integral forms which need to be evaluated. After (trivially) integrating out the t dependence to bring down a factor of $2\pi\delta(\omega - uk_z)$, the three distinct integral forms are

$$\int \frac{d\mathbf{x} e^{-i\mathbf{k} \cdot \mathbf{x} - \rho m}}{(z^2 \gamma^2 + \rho^2)} \begin{bmatrix} (1, \cos \phi, \sin \phi) \\ \frac{z}{(z^2 \gamma^2 + \rho^2)} \\ \frac{1}{\sqrt{z^2 \gamma^2 + \rho^2}} \end{bmatrix} \equiv \begin{bmatrix} \Lambda_1 \\ \Lambda_2 \\ \Lambda_3 \end{bmatrix}. \quad (\text{F-4})$$

The exponential dependence upon the variable ϕ is in the term $-i\rho(k_x \cos \phi + k_y \sin \phi)$. Re-writing this term as $-i\rho k_T \cos[\phi - \alpha]$, where $k_x = k_T \cos \alpha$ and $k_y = k_T \sin \alpha$, the ϕ integration can be done using the relations

$$\int_0^{2\pi} \frac{d\phi}{2\pi} \begin{bmatrix} 1 \\ \cos \phi \\ \sin \phi \end{bmatrix} \exp[\pm i k_T \rho (\cos[\phi - \alpha])] = \begin{bmatrix} J_0(\rho k_T) \\ \pm i J_1(\rho k_T) \cos \alpha \\ \pm i J_1(\rho k_T) \sin \alpha \end{bmatrix} \quad (\text{F-5})$$

where $J_i(x)$ is the Bessel function of the first kind of order i . The final result for Λ_2 is obtained by using the relation

$$\int_{-\infty}^{\infty} dz \int_0^{\infty} d\rho \frac{e^{-izk_z - \rho m} J_0(\rho k_T) z \rho}{(\rho^2 + \gamma^2 z^2)^2} = \frac{ik_z \pi}{2\gamma^2 \sqrt{k_z^2 + (k_T^2 + m^2) \gamma^2 + 2m\gamma|k_z|}} \quad (\text{F-6})$$

which gives, in the large γ limit,

$$\Lambda_2 = -\frac{(2\pi) ik_z \pi}{2\gamma^3 \sqrt{k_T^2 + m^2}}. \quad (\text{F-7})$$

The first component of Λ_1 , denoted by Λ_{1a} , requires evaluating

$$\int_{-\infty}^{\infty} dz \int_0^{\infty} d\rho \frac{e^{-izk_z - \rho m} J_0(\rho k_T) \rho}{(\rho^2 + \gamma^2 z^2)} = \frac{\pi}{\sqrt{k_z^2 + (k_T^2 + m^2) \gamma^2 + 2m\gamma|k_z|}}. \quad (\text{F-8})$$

The second two components of Λ_1 , denoted by Λ_{1b} , can be determined after evaluating

$$\int_{-\infty}^{\infty} dz \int_0^{\infty} d\rho \frac{e^{-izk_z - \rho m} J_1(\rho k_T) \rho}{(\rho^2 + \gamma^2 z^2)} = \frac{\pi}{k_T \gamma} \left(1 - \frac{m\gamma + |k_z|}{\sqrt{k_z^2 + (k_T^2 + m^2) \gamma^2 + 2m\gamma|k_z|}} \right). \quad (\text{F-9})$$

Again, working in the large γ limit, this gives for Λ_1

$$\Lambda_{1a} = \frac{2\pi^2}{\gamma \sqrt{k_T^2 + m^2}} \quad (\text{F-10})$$

$$\Lambda_{1b} = -\frac{2\pi^2 i}{\gamma k_T} \left(1 - \frac{m}{\sqrt{k_T^2 + m^2}} \right) (\cos \alpha, \sin \alpha).$$

To determine Λ_3 it is necessary to evaluate

$$\int_{-\infty}^{\infty} dz \int_0^{\infty} d\rho \frac{e^{-izk_z - \rho m} J_0(\rho k_T) \rho}{(z^2 \gamma^2 + \rho^2)^{3/2}}. \quad (\text{F-11})$$

The above form of (F-11) is difficult to evaluate analytically. However, it can be made more manageable by including the screening factor in the z , rather than ρ , integration. In this case, one has in the large γ limit

$$\int_{-\infty}^{\infty} dz \int_0^{\infty} d\rho \frac{e^{-izk_z - \gamma|z|m} J_0(\rho k_T) \rho}{(z^2 \gamma^2 + \rho^2)^{3/2}} = \frac{2}{\gamma} G_0 \left(\frac{m + k_T}{2\sqrt{E_p T}} \right) \quad (\text{F-12})$$

where $z_{min} = (2\gamma\sqrt{E_p T})^{-1}$ has been used as a short distance cutoff in the z integration. This gives for Λ_3

$$\Lambda_3 = \frac{4\pi}{\gamma} G_0 \left(\frac{m + k_T}{2\sqrt{E_p T}} \right). \quad (\text{F-13})$$

It is now possible to write down the final result for (F-2) and (F-1). Remembering to include the factor of $2\pi\delta(\omega - uk_z)$ from the t integration, one has

$$\begin{aligned} J^0(\mathbf{k}, \omega) &= \frac{\alpha_s(Q_p^a)^2 m_D^2 u^2}{2} (2\pi)\delta(\omega - uk_z) \\ &\quad \times \left(G_0 \left(\frac{m + k_T}{2\sqrt{E_p T}} \right) + \frac{i\pi(\mathbf{u} \cdot \mathbf{k})}{4\gamma\sqrt{k_T^2 + m^2}} \right) \\ \mathbf{J}(\mathbf{k}, \omega) &= \frac{\alpha_s(Q_p^a)^2 m_D^2 u^2}{2} (2\pi)\delta(\omega - uk_z) \\ &\quad \times \left(\mathbf{u} G_0 \left(\frac{m + k_T}{2\sqrt{E_p T}} \right) \right. \\ &\quad \left. + \frac{i\pi}{4\gamma} \left(\frac{\sqrt{k_T^2 + m^2} - m}{k_T^2} \right) \left(u^2 \mathbf{k} + \frac{\mathbf{u}(\mathbf{u} \cdot \mathbf{k})m}{\sqrt{k_T^2 + m^2}} \right) \right) \end{aligned} \quad (\text{F-14})$$

which is the result quoted in (6.28).

Appendix G: Evaluating (6.51)

I here consider the evaluation of

$$\begin{aligned}
\epsilon(x, t) &= \int \frac{d^4k}{(2\pi)^4} e^{i\mathbf{k}\cdot\mathbf{x}-i\omega t} \epsilon(\mathbf{k}, \omega) \\
&= i\hat{O} \int \frac{d^4k}{(2\pi)^4} e^{i\mathbf{k}\cdot\mathbf{x}-i\omega t} \times \\
&\quad \frac{(ik_z + i\omega - \Gamma_s k^2)(1 - e^{-t_M(ik_z + \gamma - i\omega)})}{(\omega^2 - c_s^2 k^2 + i\Gamma_s \omega k^2)(\omega - k_z + i\gamma)} + \frac{(-ik_z + i\omega - \Gamma_s k^2)(1 - e^{t_M(ik_z - \gamma + i\omega)})}{(\omega^2 - c_s^2 k^2 + i\Gamma_s \omega k^2)(\omega + k_z + i\gamma)}
\end{aligned} \tag{G-1}$$

where $\hat{O} = \Delta E_0 - \Delta E_1 \partial/\partial\gamma$, as was discussed in Chapter 6. The first step is to perform a contour integration in ω . The poles are all in the lower complex plane and are given by

$$\begin{aligned}
\omega &= -\frac{i\Gamma_s k^2}{2} \pm \sqrt{c_s^2 k^2 - \Gamma_s^2 k^4/4}, \text{ and } \pm k_z - i\gamma \\
&= -\frac{i\Gamma_s k^2}{2} \pm c_s k, \text{ and } \pm k_z - i\gamma
\end{aligned} \tag{G-2}$$

where the second order dissipative term has been dropped in the second line. I am here taking $t > t_M > 0$ such that it is necessary to close the contour in the lower complex plane for all terms in (G-1). It is helpful to note that the residues from the poles given by $\omega = \pm k_z - i\gamma$ contribute to zero (as the reader can check) and can be ignored.

The first term from (G-1) requires evaluating

$$\int \frac{d\omega}{2\pi} \frac{(ik_z + i\omega - \Gamma_s k^2)(e^{-i\omega t} - e^{-i\omega(t-t_M)-t_M(ik_z + \gamma)})}{(\omega + i\frac{\Gamma_s k^2}{2} - c_s k)(\omega + i\frac{\Gamma_s k^2}{2} + c_s k)(\omega - k_z + i\gamma)}. \tag{G-3}$$

Summing over the residues gives

$$\begin{aligned}
& -i \left[\frac{(ik_z + i\omega - \Gamma_s k^2)(e^{-i\omega t} - e^{-i\omega(t-t_M)-t_M(ik_z+\gamma)})}{(\omega - k_z + i\gamma)} \frac{1}{(\omega + i\frac{\Gamma_s k^2}{2} + c_s k)} \right]_{\omega=+} + \\
& -i \left[\frac{(ik_z + i\omega - \Gamma_s k^2)(e^{-i\omega t} - e^{-i\omega(t-t_M)-t_M(ik_z+\gamma)})}{(\omega - k_z + i\gamma)} \frac{1}{(\omega + i\frac{\Gamma_s k^2}{2} - c_s k)} \right]_{\omega=-} .
\end{aligned} \tag{G-4}$$

where $]_{\omega=\pm}$ means to evaluate the expression at $\omega = -\frac{i\Gamma_s k^2}{2} \pm c_s k$. Plugging in the appropriate expressions gives

$$\begin{aligned}
& i \left[\frac{(ik_z + ic_s k - \Gamma_s H k^2)(e^{-\Gamma_s H k^2 t - ic_s k t} - e^{(-\Gamma_s k^2 H - ic_s k)(t-t_M)-t_M(ik_z+\gamma)})}{2c_s k(k_z - c_s k + i\Gamma_s H k^2 - i\gamma)} \right] - \\
& i \left[\frac{(ik_z - ic_s k - \Gamma_s H k^2)(e^{-\Gamma_s H k^2 t + ic_s k t} - e^{(-\Gamma_s k^2 H + ic_s k)(t-t_M)-t_M(ik_z+\gamma)})}{2c_s k(k_z + c_s k + i\Gamma_s H k^2 - i\gamma)} \right]
\end{aligned} \tag{G-5}$$

where $\Gamma_s H = \Gamma_s/2$. The expression resulting from the first term is therefore

$$\begin{aligned}
\delta\epsilon_a(x, t) = (-)\hat{O} \int \frac{d^3 k}{(2\pi)^3} \frac{e^{i\mathbf{k}\cdot\mathbf{x} - \Gamma_s H k^2 t}}{2c_s k} \times \\
\left[\frac{(ik_z + ic_s k - \Gamma_s H k^2)(e^{-ic_s k t} - e^{-ic_s k(t-t_M)-t_M(ik_z+\gamma-\Gamma_s H k^2)})}{(k_z - c_s k + i\Gamma_s H k^2 - i\gamma)} - \right. \\
\left. \frac{(ik_z - ic_s k - \Gamma_s H k^2)(e^{ic_s k t} - e^{ic_s k(t-t_M)-t_M(ik_z+\gamma-\Gamma_s H k^2)})}{(k_z + c_s k + i\Gamma_s H k^2 - i\gamma)} \right]
\end{aligned} \tag{G-6}$$

where the subscript a is meant to indicate this is the first term from (G-1). Performing the ϕ integration and switching to spherical coordinates leaves

$$\begin{aligned}
\delta\epsilon_a(x, t) = (-)\hat{O} \int \frac{dk du J_0(\rho k \sqrt{1-u^2})}{(2\pi)^2} \frac{k e^{-\Gamma_s H k^2 t + ik_z z}}{2c_s} \times \\
\left[\frac{(iku + ic_s k - \Gamma_s H k^2)(e^{-ic_s k t} - e^{-ic_s k(t-t_M)-t_M(iku+\gamma-\Gamma_s H k^2)})}{(ku - c_s k + i\Gamma_s H k^2 - i\gamma)} - \right. \\
\left. \frac{(iku - ic_s k - \Gamma_s H k^2)(e^{ic_s k t} - e^{ic_s k(t-t_M)-t_M(iku+\gamma-\Gamma_s H k^2)})}{(ku + c_s k + i\Gamma_s H k^2 - i\gamma)} \right]
\end{aligned} \tag{G-7}$$

which is evaluated can be evaluated numerically after performing the derivative in \hat{O} and setting $\gamma = 0$. In the expression, $u = \cos \theta$ and $\rho = \sqrt{x^2 + y^2}$.

The second term from (G-1) can be evaluated in a completely analogous manner to leave

$$\begin{aligned} \delta\epsilon_b(x, t) = (-)\hat{O} \int \frac{dk du J_0(\rho k \sqrt{1-u^2})}{(2\pi)^2} \frac{k e^{-\Gamma_s H k^2 t + i k_z z}}{2c_s} \times \\ \left[\frac{(-iku + ic_s k - \Gamma_s H k^2)(e^{-ic_s k t} - e^{-ic_s k(t-t_M) + t_M(iku - \gamma + \Gamma_s k^2 H)})}{(-ku - c_s k + i\Gamma_s H k^2 - i\gamma)} + \right. \\ \left. \frac{(iku + ic_s k + \Gamma_s H k^2)(e^{ic_s k t} - e^{ic_s k(t-t_M) + t_M(iku - \gamma + \Gamma_s k^2 H)})}{(-ku + c_s k + i\Gamma_s H k^2 - i\gamma)} \right] \end{aligned} \quad (\text{G-8})$$

and the final result for $\delta\epsilon$ is the sum of $\delta\epsilon_a$ and $\delta\epsilon_b$.

Next consider the longitudinal momentum density, which has the form

$$\begin{aligned} \mathbf{g}_L(x, t) = i\hat{O} \int \frac{d^4 k}{(2\pi)^4} e^{i\mathbf{k}\cdot\mathbf{x} - i\omega t} \frac{\mathbf{k}}{k^2} \times \\ \frac{(i\omega k_z + ic_s^2 k^2)(1 - e^{-t_M(ik_z + \gamma - i\omega)})}{(\omega^2 - c_s^2 k^2 + i\Gamma_s \omega k^2)(\omega - k_z + i\gamma)} + \frac{(-i\omega k_z + ic_s^2 k^2)(1 - e^{t_M(ik_z - \gamma + i\omega)})}{(\omega^2 - c_s^2 k^2 + i\Gamma_s \omega k^2)(\omega + k_z + i\gamma)}. \end{aligned} \quad (\text{G-9})$$

The evaluation of $\mathbf{g}_L(x, t)$ proceeds analogously with the calculation of $\delta\epsilon$. The result is given by

$$\begin{aligned} \mathbf{g}_{L1a}(x, t) = (-)\hat{O} \int \frac{dk du}{(2\pi)^2} \frac{e^{-\Gamma_s H k^2 t + iku}}{2c_s} \times \\ \left(i\sqrt{1-u^2} J_1(k\rho\sqrt{1-u^2}) \cos \alpha, i\sqrt{1-u^2} J_1(k\rho\sqrt{1-u^2}) \sin \alpha, u J_0(k\rho\sqrt{1-u^2}) \right) \times \\ \left[\frac{(iku(c_s k - i\Gamma_s H k^2) + ic_s^2 k^2)(e^{-ic_s k t} - e^{-ic_s k(t-t_M) - t_M(iku + \gamma - \Gamma_s H k^2)})}{(ku - c_s k + i\Gamma_s H k^2 - i\gamma)} - \right. \\ \left. \frac{(iku(-c_s k - i\Gamma_s H k^2) + ic_s^2 k^2)(e^{ic_s k t} - e^{ic_s k(t-t_M) - t_M(iku + \gamma - \Gamma_s H k^2)})}{(ku + c_s k + i\Gamma_s H k^2 - i\gamma)} \right] \end{aligned} \quad (\text{G-10})$$

and

$$\begin{aligned}
\mathbf{g}_{L1b}(x, t) = & (-)\hat{O} \int \frac{dkdu}{(2\pi)^2} \frac{e^{-\Gamma_s H k^2 t + iku}}{2c_s} \times \\
& \left(i\sqrt{1-u^2} J_1(k\rho\sqrt{1-u^2}) \cos \alpha, i\sqrt{1-u^2} J_1(k\rho\sqrt{1-u^2}) \sin \alpha, uJ_0(k\rho\sqrt{1-u^2}) \right) \times \\
& \left[\frac{(iku(-c_s k + i\Gamma_s H k^2) + ic_s^2 k^2)(e^{-ic_s k t} - e^{-ic_s k(t-t_M) - t_M(-iku + \gamma - \Gamma_s H k^2)})}{(-ku - c_s k + i\Gamma_s H k^2 - i\gamma)} - \right. \\
& \left. \frac{(iku(c_s k + i\Gamma_s H k^2) + ic_s^2 k^2)(e^{ic_s k t} - e^{ic_s k(t-t_M) - t_M(-iku + \gamma - \Gamma_s H k^2)})}{(-ku + c_s k + i\Gamma_s H k^2 - i\gamma)} \right]
\end{aligned} \tag{G-11}$$

where α is the position space azimuthal angle around the \hat{z} axis. The above integrals are performed numerically.

The transverse momentum density is given by the expression

$$\begin{aligned}
\mathbf{g}_T(x, t) = & i\hat{O} \int \frac{d^4k}{(2\pi)^4} e^{i\mathbf{k}\cdot\mathbf{x} - i\omega t} \frac{(-k_x k_z, -k_y k_z, k_T^2)}{k^2} \times \\
& \frac{i(1 - e^{-t_M(ik_z + \gamma - i\omega)})}{(\omega + \frac{3}{4}i\Gamma_s k^2)(\omega - k_z + i\gamma)} + \frac{-i(1 - e^{t_M(ik_z - \gamma + i\omega)})}{(\omega + \frac{3}{4}i\Gamma_s k^2)(\omega + k_z + i\gamma)}.
\end{aligned} \tag{G-12}$$

The ω integration here takes the form

$$\int \frac{d\omega}{(2\pi)} e^{-i\omega t} \frac{i(1 - e^{-t_M(ik_z + \gamma - i\omega)})}{(\omega + \frac{3}{4}i\Gamma_s k^2)(\omega - k_z + i\gamma)} + \frac{-i(1 - e^{t_M(ik_z - \gamma + i\omega)})}{(\omega + \frac{3}{4}i\Gamma_s k^2)(\omega + k_z + i\gamma)} \tag{G-13}$$

whose only contributing pole is at

$$\omega = -i\frac{3}{4}\Gamma_s k^2 \equiv -iQ\Gamma_s k^2 \tag{G-14}$$

which again is in the lower complex plane. The contour integration can be done to give

$$\begin{aligned}
& -ie^{-Q\Gamma_s k^2 t} \left[\frac{i(1 - e^{-t_M(ik_z + \gamma - Q\Gamma_s k^2)})}{(-iQ\Gamma_s k^2 - k_z + i\gamma)} + \frac{-i(1 - e^{t_M(ik_z - \gamma + Q\Gamma_s k^2)})}{(-iQ\Gamma_s k^2 + k_z + i\gamma)} \right] \\
& = e^{-Q\Gamma_s k^2 t} \left[\frac{(1 - e^{-t_M(ik_z + \gamma - Q\Gamma_s k^2)})}{(-iQ\Gamma_s k^2 - k_z + i\gamma)} - \frac{(1 - e^{t_M(ik_z - \gamma + Q\Gamma_s k^2)})}{(-iQ\Gamma_s k^2 + k_z + i\gamma)} \right]
\end{aligned} \tag{G-15}$$

and one is left to evaluate

$$\mathbf{g}_T(x, t) = i\hat{O} \int \frac{d^3k}{(2\pi)^3} e^{-Q\Gamma_s k^2 t + i\mathbf{k}\cdot\mathbf{x}} \frac{(-k_x k_z, -k_y k_z, k_T^2)}{k^2} \times \left[\frac{(1 - e^{-tM(ik_z + \gamma - Q\Gamma_s k^2)})}{(-iQ\Gamma_s k^2 - k_z + i\gamma)} - \frac{(1 - e^{tM(ik_z - \gamma + Q\Gamma_s k^2)})}{(-iQ\Gamma_s k^2 + k_z + i\gamma)} \right]. \quad (\text{G-16})$$

Performing the ϕ integration gives

$$\mathbf{g}_T(x, t) = i\hat{O} \int \frac{dkdu}{(2\pi)^2} e^{-Q\Gamma_s k^2 t + iku\sqrt{1-u^2}} \times \left(-iuJ_1(k\rho\sqrt{1-u^2}) \cos \alpha, -iuJ_1(k\rho\sqrt{1-u^2}) \sin \alpha, \sqrt{1-u^2} J_0(k\rho\sqrt{1-u^2}) \right) \times \left[\frac{(1 - e^{-tM(iku + \gamma - Q\Gamma_s k^2)})}{(-iQ\Gamma_s k^2 - ku + i\gamma)} - \frac{(1 - e^{tM(iku - \gamma + Q\Gamma_s k^2)})}{(-iQ\Gamma_s k^2 + ku + i\gamma)} \right]. \quad (\text{G-17})$$

which can be done numerically.

Appendix H: Numerical Integration

Several times in this thesis results were cast in the form of an integration which could be done numerically but not analytically. In all numerical integrations the software program *Mathematica* has been used. There are several ways to gauge the accuracy of the numerical results of integration which I will discuss here.

The most straightforward gauge of accuracy in the numerical integration routine of *Mathematica* is found by using the option of `AccuracyGoal`. Setting `AccuracyGoal` \rightarrow n effectively limits the error to be of order 10^{-n} . If the program takes an abnormally long amount of time to converge to the specified accuracy, it issues a warning, but continues the evaluation. In such a case, a result is obtained but the accuracy may be less than specified in `AccuracyGoal`. In more extreme cases, the error may be comparable in size to the integration value, in which case a warning is issued which gives the result of the integration and the estimated error size. Finally, the program

may be unable to obtain a finite result, in which case a warning is issued stating the integral does not converge. For any given evaluation, the error messages provide a natural check on accuracy. For most results, I have used an AccuracyGoal of 6.

A second, but less quantitative, check on accuracy is found in the amount of time an evaluation takes. Typically, for a given AccuracyGoal, more straightforward manipulations converge quickly, while more difficult evaluations may take much longer. Generally speaking, if an integration takes an inordinate amount of time, the program is struggling to evaluate it and the answer may be wrong. Most of the plots presented in this thesis required hundreds of evaluation points, providing a natural deterrent to using very slowly evaluating integrals. However, the amount of time an evaluation takes is only a rough guide for accuracy. Sometimes integrations where the error is comparable in size to the integration value evaluate very quickly.

Finally, the most basic check on the accuracy of numerical integration is found in plotting the final result. Clearly, results which vary smoothly and are consistent with known results are more likely numerically accurate than choppy results which are not consistent with physical intuition. Similarly, one can check how the plots change when a parameter of the calculation is varied, such as was done in Chapter 6 for the speed of sound and shear viscosity. In these cases, one has a reasonable idea ahead of time how the plots should change.

Bibliography

- [1] M. E. Peskin and D. V. Schroeder, “An Introduction To Quantum Field Theory,”
Reading, USA: Addison-Wesley (1995) 842 p
- [2] H. Satz, *Ann. Rev. Nucl. Part. Sci.* **35**, 245 (1985).
- [3] B. Muller and K. Rajagopal, *Eur. Phys. J. C* **43**, 15 (2005).
- [4] L. D. McLerran, *Rev. Mod. Phys.* **58**, 1021 (1986).
- [5] F. Karsch, *Nucl. Phys. A* **698**, 199 (2002).
- [6] L. D. McLerran and B. Svetitsky, *Phys. Rev. D* **24**, 450 (1981).
- [7] F. Karsch, *PoS LAT2007*, 015 (2007).
- [8] E. V. Shuryak, *Phys. Lett. B* **107**, 103 (1981).
- [9] A. Bazavov *et al.*, arXiv:0903.4379 [hep-lat].
- [10] J. Stachel, *Nucl. Phys. A* **654**, 119C (1999).
- [11] F. Karsch, *Nucl. Phys. A* **783**, 13 (2007).
- [12] J. D. Bjorken, *Phys. Rev. D* **27**, 140 (1983).
- [13] I. Arsene *et al.* [BRAHMS Collaboration], *Nucl. Phys. A* **757**, 1 (2005);
- [14] B. B. Back *et al.*, *Nucl. Phys. A* **757**, 28 (2005);
- [15] J. Adams *et al.* [STAR Collaboration], *Nucl. Phys. A* **757**, 102 (2005);
- [16] K. Adcox *et al.* [PHENIX Collaboration], *Nucl. Phys. A* **757**, 184 (2005).

- [17] K. Adcox *et al.* [PHENIX Collaboration], Phys. Rev. Lett. **89**, 212301 (2002).
- [18] J. Adams *et al.* [STAR Collaboration], Phys. Rev. C **72**, 014904 (2005).
- [19] H. B. Meyer, Phys. Rev. Lett. **100**, 162001 (2008).
- [20] M. Luzum and P. Romatschke, Phys. Rev. C **78**, 034915 (2008).
- [21] P. Kovtun, D. T. Son and A. O. Starinets, Phys. Rev. Lett. **94**, 111601 (2005).
- [22] S. S. Adler *et al.* [PHENIX Collaboration], Phys. Rev. Lett. **96**, 202301 (2006).
- [23] C. Adler *et al.* [STAR Collaboration], Phys. Rev. Lett. **90**, 082302 (2003).
- [24] A. Adare *et al.* [PHENIX Collaboration], Phys. Rev. C **78**, 014901 (2008).
- [25] C. B. Chiu and R. C. Hwa, Phys. Rev. C **74**, 064909 (2006).
- [26] N. Armesto, C. A. Salgado and U. A. Wiedemann, Phys. Rev. Lett. **93**, 242301 (2004).
- [27] J. G. Ulery, J. Phys. G **35**, 104032 (2008) [arXiv:0807.1613 [nucl-ex]].
- [28] J. G. Ulery, arXiv:0801.4904 [nucl-ex].
- [29] V. Koch, A. Majumder and X. N. Wang, Phys. Rev. Lett. **96**, 172302 (2006).
- [30] A. Majumder and X. N. Wang, Phys. Rev. C **73**, 051901 (2006).
- [31] <http://www.kettering.edu/~drussell/Demos/doppler/doppler.html>
- [32] J. Casalderrey-Solana, E. V. Shuryak and D. Teaney, J. Phys. Conf. Ser. **27**, 22 (2005).
- [33] H. Stöcker, Nucl. Phys. A **750** (2005) 121.
- [34] L. M. Satarov, H. Stöcker and I. N. Mishustin, Phys. Lett. B **627** (2005) 64.
- [35] J. Ruppert and B. Müller, Phys. Lett. B **618**, 123 (2005).
- [36] T. Renk and J. Ruppert, Phys. Rev. C **73** (2006) 011901; Phys. Lett. B **646** (2007) 19; Int. J. Mod. Phys. E **16** (2008) 3100.

- [37] T. Renk and J. Ruppert, Phys. Rev. C **76** (2007) 014908;
- [38] A. K. Chaudhuri and U. Heinz, Phys. Rev. Lett. **97**, 062301 (2006).
- [39] B. Betz, M. Gyulassy, D. H. Rischke, H. Stoecker and G. Torrieri, J. Phys. G **35**, 104106 (2008).
- [40] B. Betz, M. Gyulassy, J. Noronha and G. Torrieri, arXiv:0807.4526 [hep-ph].
- [41] J. Noronha, M. Gyulassy and G. Torrieri, Phys. Rev. Lett. **102**, 102301 (2009).
- [42] R. B. Neufeld, B. Muller and J. Ruppert, Phys. Rev. C **78**, 041901 (2008).
- [43] R. B. Neufeld, Phys. Rev. D **78**, 085015 (2008).
- [44] R. B. Neufeld, Phys. Rev. C **79**, 054909 (2009).
- [45] R. B. Neufeld, Eur. Phys. J. C **62**, 271, (2009).
- [46] J. J. Friess, S. S. Gubser, G. Michalogiorgakis and S. S. Pufu, Phys. Rev. D **75**, 106003 (2007).
- [47] P. M. Chesler and L. G. Yaffe, Phys. Rev. D **78**, 045013 (2008).
- [48] X. N. Wang and M. Gyulassy, Phys. Rev. Lett. **68**, 1480 (1992).
- [49] R. Baier, Y. L. Dokshitzer, A. H. Mueller, S. Peigne and D. Schiff, Nucl. Phys. B **484**, 265 (1997).
- [50] B. G. Zakharov, JETP Lett. **65**, 615 (1997).
- [51] M. Gyulassy, P. Levai and I. Vitev, Phys. Rev. Lett. **85**, 5535 (2000).
- [52] X. f. Guo and X. N. Wang, Phys. Rev. Lett. **85**, 3591 (2000).
- [53] R. Baier, D. Schiff and B. G. Zakharov, Ann. Rev. Nucl. Part. Sci. **50**, 37 (2000).
- [54] N. Armesto, C. A. Salgado and U. A. Wiedemann, Phys. Rev. Lett. **94**, 022002 (2005).
- [55] P. Jacobs and X. N. Wang, Prog. Part. Nucl. Phys. **54**, 443 (2005).
- [56] P. Arnold, G. D. Moore and L. G. Yaffe, JHEP **0301**, 030 (2003).

- [57] O. Kaczmarek and F. Zantow, Phys. Rev. D **71**, 114510 (2005).
- [58] D. Molnar and M. Gyulassy, Nucl. Phys. A **697**, 495 (2002) [Erratum-ibid. A **703**, 893 (2002)].
- [59] U. W. Heinz, Phys. Rev. Lett. **51**, 351 (1983).
- [60] M. Asakawa, S. A. Bass and B. Müller, Prog. Theor. Phys. **116**, 725 (2006).
- [61] S. K. Wong, Nuovo Cim. A **65S10**, 689 (1970).
- [62] E. Braaten and R. D. Pisarski, Nucl. Phys. B **337**, 569 (1990).
- [63] M. H. Thoma, Phys. Lett. B **273**, 128 (1991).
- [64] C. A. Salgado and U. A. Wiedemann, Phys. Rev. D **68**, 014008 (2003).
- [65] R. Baier and Y. Mehtar-Tani, Phys. Rev. C **78**, 064906 (2008).
- [66] P. M. Chesler, K. Jensen, A. Karch and L. G. Yaffe, arXiv:0810.1985 [hep-th].
- [67] S. A. Bass, C. Gale, A. Majumder, C. Nonaka, G. Y. Qin, T. Renk and J. Ruppert, Phys. Rev. C **79**, 024901 (2009).
- [68] A. K. Das, *Singapore, Singapore: World Scientific (1997) 404 p*
- [69] C. Itzykson and J. B. Zuber, *New York, Usa: Mcgraw-hill (1980) 705 P.(International Series In Pure and Applied Physics)*
- [70] A. Patkos and Z. Szep, Phys. Lett. B **446**, 272 (1999).
- [71] P. Arnold, G. D. Moore and L. G. Yaffe, JHEP **0011**, 001 (2000).
- [72] S. S. Adler *et al.* [PHENIX Collaboration], Phys. Rev. Lett. **97**, 052301 (2006).
- [73] P. Arnold, G. D. Moore and L. G. Yaffe, JHEP **0305**, 051 (2003).
- [74] Z. Xu and C. Greiner, Phys. Rev. Lett. **100**, 172301 (2008).
- [75] P. Romatschke and U. Romatschke, Phys. Rev. Lett. **99**, 172301 (2007).
- [76] M. Asakawa, S. A. Bass and B. Müller, Phys. Rev. Lett. **96**, 252301 (2006).

- [77] O. Aharony, S. S. Gubser, J. M. Maldacena, H. Ooguri and Y. Oz, Phys. Rept. **323**, 183 (2000).
- [78] A. Erdelyi, W. Magnus, F. Oberhettinger and F.G. Tricomi, Tables of Integral Transforms, Vol. 1, New York, McGraw-Hill (1954).

Biography

Richard Bryon Neufeld, Junior

- **Personal**

- Born March 22nd, 1982 near Chattanooga, TN

- **Education**

- B.S. in Math and Physics, King College, Bristol, Tennessee, 2004
- A.M. in Physics, Duke University, Durham, North Carolina, 2007

- **Academic Honors**

- Co-authored publication (Phys. Rev. C **78**, 041901 (2008)) which was highlighted in the APS Journal Physics

- **Publications**

- R. B. Neufeld, *Mach Cones in the quark-gluon plasma: viscosity, speed of sound, and effects of finite source structure*, Phys. Rev. C **79**, 054909 (2009)
- R. B. Neufeld and B. Müller, *The sound produced by a fast parton in the quark-gluon plasma is a crescendo*, Phys. Rev. Letters (in production 2009)
- R. B. Neufeld, *Comparing different freeze-out scenarios in azimuthal hadron correlations*, Eur. Phys. J. C **62**, 271, (2009).

- R.B. Neufeld, B. Müller, and J. Ruppert, *Sonic Mach cones induced by fast partons in a perturbative quark gluon plasma*, Phys. Rev. C **78**, 041901 (2008)
- R. B. Neufeld, *Fast Partons as a Source of Energy and Momentum in a Perturbative Quark-Gluon Plasma*, Phys. Rev. D **78**, 085015 (2008)
- B. Müller and R. B. Neufeld, *The sound of a fast parton in QCD*, J. Phys. G **35**, 104108 (2008)